# Appendix G-6

# MM5 Model Performance Evaluation

# Meteorological Modeling using Penn State/NCAR 5th Generation Mesoscale Model (MM5)

**Bureau of Air Quality Analysis and Research**

**Division of Air Resources**

**New York State Department of Environmental Conservation**

**Albany, NY 12233**

**March 19, 2006**

# Meteorological Modeling using Penn State/NCAR 5th Generation Mesoscale Model (MM5)

Version 3.6 of MM5 was used to generate annual 2002 meteorology for the OTC modeling work. Prof. Dalin Zhang of the University of Maryland performed the MM5 simulations in consultation with NYSDEC staff. The model was applied in Lambert conformal map projection and utilized MPP Version developed for clusters. The two-way nested domain consisted of coarse (36km) and fine (12km) mesh corresponding to 149x129 and 175x175 grids, respectively, in this application (see Figure 1).

The Lambert projection used in this work followed the Regional Planning Organization (RPO) national domain setup with the center at (40ºN, 97ºW) and parallels at 33ºN and 45ºN. Map projection parameters in reference to the projection center point are as follows: Southwest corner for the 36 km grid is at (-2664km, -2304km) and the northeast corner at (2664km, 2304km). In the case of the 12km grid, the southwest corner is at (252km, -900km) and the northeast corner at (2340km, 1188km). In the vertical direction, the terrain following $\sigma$-coordinate system was used with the pressure at each $\sigma$-level determined from a reference state that is estimated using the hydrostatic equation from a given sea-level pressure and temperature with a standard lapse rate. There are 30 unevenly spaced $\sigma$ levels, giving 29 vertical layers, with higher resolution within the planetary boundary layer (PBL).  The $\sigma$ levels are:

1.0000, 0.9974, 0.9940, 0.8980, 0.9820, 0.9720, 0.9590, 0.9430, 0.9230, 0.8990,

0.8710, 0.8390, 0.8030, 0.7630, 0.7180, 0.6680, 0.6180, 0.5680, 0.5180, 0.4680,

0.3680, 0.3180, 0.2680, 0.2180, 0.1680, 0.1230, 0.0800, 0.0400, 0.0000

The surface layer was set at about 10m, the level at which surface winds were typically observed, and the model top was set at 50hPa with a radiative top boundary condition. The time steps for the 36km and 12km domains were 75 and 25 seconds, respectively.

The important model physics options used for this MM5 simulation include:

- Kain-Fritsch (1993) convective scheme for both 36- and 12-km domains
- Explicit moisture scheme (without the mixed phase) containing prognostic equations for cloud water (ice) and rainwater (snow) (Dudhia 1989; Zhang 1989)
- Modified version of the Blackadar planetary boundary layer (PBL) scheme (Zhang and Anthes 1982; Zhang and Zheng 2004)
- Simple radiative cooling scheme (Grell et al. 1994)
- Multi-layer soil model to predict land surface temperatures using the surface energy budget equation (Dudhia 1996)

Note that the Blackadar PBL scheme has been modified in order to correct the phase shift of surface wind speed and temperature diurnal cycle, following a study that compared five different PBL schemes: the Gayno-Seaman TKE scheme (Shafran et al. 2000), Burk-

Thompson (1989), Blackadar (Zhang and Anthes 1982), MRF (Hong and Pan 1996), and Mellor-Yamada-Jajic (Mellor and Yamada 1974; Jajic 1990, 1994). The details of the study can be found at Zhang and Zheng (2004).

**Nudging Processes**

The MM5 provides options for nudging observations for each domain during the model integration process (Stauffer and Seaman, 1990; Stauffer et al. 1991). The Eta analyses of upper-air winds, temperature and water-vapor mixing ratio as well as their associated surface fields were used for nudging every 6 hours, and the Eta surface wind fields blended with surface wind observations were used to nudge every 3 hours. While only the surface winds were nudged, their influences could extend into the PBL as well (see Stauffer et al. 1991). Based on UMD's prior experience in numerical experiments, the following nudging coefficients have been used:

- Upper-air wind fields: $5.0E\text{-}4s^{-1}$ for Domain 1 (36km), and $2.5E\text{-}4s^{-1}$ for Domain 2 (12km);
- Upper-air temperature fields: $1.0E\text{-}5s^{-1}$ for both Domains;
- Surface winds: $5.0s^{-1}E\text{-}4s^{-1}$ for Domain 1, and $2.5E\text{-}4s^{-1}$ for Domain 2; and
- Surface temperature and moisture: not nudged due to instability consideration.

**ASSESSMENT**

This assessment covers the period of May through September 2002.

**National Weather Service (NWS) and CASTNet data – Surface temperature, Wind Speed, and Humidity**

NWS (TDL) and CASTNet (www.epa.gov/castnet/) surface measurements of temperature, wind speed, and humidity (note there were no humidity measurements for CASTNet) were used to compare with the MM5 outputs. The evaluation was performed with METSTAT program developed by Environ Corporation (www.camx.com/files/metstat.15feb05.tar.gz)   When comparing to NWS data, the METSTAT interpolates the first layer MM5 (at 10m height) temperature and humidity data to a height of 2m, the level that corresponds to the NWS measurement of these parameters. However, no such interpolation was made for wind speed and direction. In the case of CASTNet surface measurements, no such changes were needed as CASTNet data were reported at a height of 10m. In this analysis, no exclusion was made for calm conditions. The reported calm winds (zero wind speed measured) were treated as is in this evaluation effort. The   METSTAT calculated standard statistical measures – average, bias, error and index of agreement between the measured and predicted parameters.

 Figure 2 displays the temperature and wind speed comparison of MM5 and measured data from NWS and CASTNet networks for August 2002. MM5 performance for both in magnitude and diurnal timing, temperature can be considered to be quite good for both NWS and CASTNet data, while MM5 underpredicted NWS and overpredicted CASTNet

daytime wind speed, respectively. It should be pointed out that there are differences in how the meteorological information is collected and reported by the two networks as well as in MM5. The CASTNet measurements are based on hourly averaged wind speed while NWS reports 2min average at 10min before the hour, whereas MM5 predictions are reflective of the last time-step of the hour of computation. Interestingly, MM5 appears to track quite well the nighttime minimum wind speed for both networks. In the case of humidity (not shown), MM5 tracks the NWS observed humidity trend well, but MM5 missed the observed semi-diurnal cycles.  Comparisons for the five months including bias and root mean square error from both NWS and CASTNet are available on request from NYSDEC.

The above assessment is based on domain-wide averages to provide an overall response of the model over the five months. Another way of assessing the model is to examine the degree of correlation between the measured and predicted parameters. Figures 3a and 3b displays such a comparison for wind speed and temperature, respectively, for the NWS hourly data covering the period of May through September 2002. For the NWS data, the correlations are in the range from 0.7 to 0.8 for wind speed, above 0.96 for temperature, and in the range of 0.8 to 0.9 for humidity. CASTNet data (not shown) also exhibit similar correlation. These correlations indicate that MM5 simulation has captured both the diurnal and synoptic scale variations. Detailed plots of this comparison are available on request from NYSDEC.

**Vertical Profiler – Winds**

The Wind-Profiler network measurements along the U. S. East Coast ([www.madis-fsl.org/cap)](www.madis-fsl.org/cap)) were used to evaluate the vertical profiles from MM5. There are twelve wind-profiler measurement stations from which data were available for comparison. For convenience of comparison, the wind-profiler measurements were interpolated to the MM5 vertical levels. The approach used was simple interpolation between two adjacent wind-profiler layers to the MM5 vertical level, and was limited to that reported by the profiler measurement. The focus of the comparison was to assess if MM5 was able to capture the measured vertical structure, and for this we used the observed Low Level Jet (LLJ) as an indicator. The comparison was performed for June, July and August 2002. In general it is found that MM5 captures the profiler measured vertical wind field structure reasonably well.  Figure 4 displays an example of the MM5 and wind profiler comparison for the August 2002 episode at Richmond, VA and Concord, NH. MM5 predicted weaker LLJ winds compared to those based on the wind-profiler measurements. The detailed plots of this comparison are available on request from NYSDEC.

**Cloud Cover – Satellite cloud image**

Cloud information derived from satellite image data ([www.atmos.umd.edu/~srb/gcip/webgcip.htm](www.atmos.umd.edu/~srb/gcip/webgcip.htm) )were used to assess the MM5 prediction of cloud cover. The $0.5^o$ by $0.5^o$ resolution of the satellite data were interpolated into the 12km MM5 grid for comparison. The MM5 total cloud fraction was estimated by MCIP based on the MM5's low cloud, middle cloud and high cloud predictions. In general,

MM5 captured the satellite cloud pattern well but underestimates the satellite cloud fraction (see Figure 5 as an example). Part of problem may due to the coarse resolution of the satellite cloud data.

**Precipitation comparison**

The monthly total observed precipitation data were constructed from 1/8-degree daily precipitation analysis data (http://data.eol.ucar.edu/codiac/dss/id=21.093 produced by Climate Prediction Center, based on 7,000-8,000 hourly/6-hourly gauge reports and radar). The MM5 monthly total precipitation was estimated from the MM5 predicted convective and non-convective rainfall and summed up for each month. In general, MM5 captured the observed spatial patterns in May and September, but no so well for June, July and August (See Figure 6), perhaps reflective of the summertime convective rain activities not captured by MM5. Detailed plots of this comparison are available on request from NYSDEC.

**Calm Conditions**

Calm conditions are defined as observed wind speed of zero knots and wind direction as $0^o$. It would be useful to assess how MM5 performs under observed calm conditions, because of potential pollutant buildup that could occur under such conditions. Table 1 lists the summary of the percentage of calm condition at each hour for the August 2002 from the NWS data within the 12km domain. It is apparent from the Table that the calm conditions occur primarily during the night and early morning hours, from 23Z (7 p.m. EDT) to 15Z (11 a.m. EDT) with a peak at 10Z (6 a.m. EDT). To assess MM5 performance, the observed and MM5 predicted wind speeds were divided into calm and non-calm according to observed wind speed. Figure 7 displays such a comparison of the MM5 predicted wind speed to the observed wind speed under the calm and non-calm conditions for the month of August 2002. For the "calm" group, the average wind speed for MM5 varies from 1 m/s during the night and early morning hours and over 1.5 m/s during the day. MM5 is over-predicting during observed calm wind conditions. There are local minima every 3 hours, due to the surface observed wind speed nudging in MM5. In contrast under the non-calm conditions, MM5 underpredicts by about 0.5 m/s for all hours with noticeable local maximum happening at the nudging hours. The MM5 nudging process would pull predictions toward the measured data, while the underprediction of MM5 for the non-calm conditions may due to the adopted PBL scheme in this simulation.

**Summary**

In this study, we performed an assessment of the MM5 simulation to real-world data, both at the surface level as well as in the vertical. While there are no specific recommended procedures identified for this assessment, similar approaches have been used elsewhere (Dolwick 2005, Baker 2004, and Johnson 2004). Traditionally, the NWS surface measurements are used for such a comparison. Since NWS data had been used through nudging processes in developing the MM5 simulation, the comparisons should

not be far removed from each other. In this study, we extended the evaluation by using CASTNet measurements that were not used in the MM5 simulations. Thus comparison with CASTNet data provides for an independent assessment and should complement the comparison with NWS data. We also compared the MM5 results with the wind profiler data and cloud data derived from satellite images to diagnose if the MM5 simulation is yielding the right type of dynamics in the vertical. The analyses shows that in general, the performance of the MM5 is reasonable both at the surface and in the vertical, thereby providing confidence in the use of these data in the CMAQ simulations.

## References

Baker, K. 2004: www.ladco.org/tech/photo/photochemical.html

Burk, S. D. and W. T. Thompson, 1989:  A vertically nested regional numerical weather prediction model with second-order closure physics. Mon. Wea. Rev., 117, 2305–2324.

Dudhia, J., 1989: Numerical study of convection observed during the winter monsoon experiments using a mesoscale two-dimensional model. J. Atmos. Sci., 46, 3077–3107.

Dudhia, J., 1996: A multi-layer soil temperature model for MM5. Preprints, 6th Annual MM5 Users Workshop, Boulder, CO.

Dolwick, P. 2005:
http://cleanairinfo.com/modelingworkshop/presentations/MPE_Dolwick.pdf

Grell, G. A., J. Dudhia , and D. R. Stauffer 1994:  A description of the fifth-generation Penn State/NCAR Mesoscale Model (MM5). NCAR Tech.Note NCAR/TN-398 1 STR, 122 pp.

Hong, S.-H., and H.-L. Pan, 1996: Nonlocal boundary layer vertical diffusion in a medium-range forecast model. Mon. Wea. Rev., 124, 2322–2339.

Jajic, Z.  I., 1990: The step-mountain coordinate: Physical package.  Mon. Wea. Rev., 118, 1429-1443.

Jajic, Z. I., 1994: The step-mountain Eta coordinate model: Further development of the convection, viscous sublayer and turbulent closure schemes. *Mon. Wea. Rev*., 122, 927-945.

Johnson, M. 2004: www.ladco.org/tech/photo/photochemical.html

Kain, J.S., and J.M. Fritsch, 1993:  Convective parameterization for mesoscale models: The Kain-Fritsch scheme. Cumulus Parameterization. Meteor. Monogr., 46,  Amer. Meteor. Soc., 165-170.

Mellor, G.  L., and T. Yamada, 1974:  A hierarchy of turbulence closure models for planetary boundary layers. J. Atmos. Sci., 31, 1791–1806.

Shafran, P.C., N.L. Seaman, and G. A. Gayno, 2000: Evaluation of numerical predictions of boundary layer structure during the Lake Michigan ozone study. J. Appl. Meteor., 39, 412-426.

Stauffer, D. R., N. L. Seaman and F. S. Binkowski 1991: Use of four-dimensional data assimilation in a limited-area mesoscale model. Part II: Effects of data assimilation within the planetary boundary layer. Mon. Wea. Rev., 119, 734-754.

Stauffer, D. R. and N. L. Seaman, 1990: Use of four-dimensional data assimilation in a limited-area mesoscale model. Part I: Experiments with synoptic-scale data. Mon. Wea. Rev., 118, 1250-1277.

Zhang, D.-L., 1989: The effect of parameterized ice microphysics on the simulation of vortex circulation with a mesoscale hydrostatic model. Tellus, 41A, 132-147.

Zhang, D.-L, and R. A. Anthes, 1982: A high-resolution model of the planetary boundary layer-sensitivity tests and comparisons with SESAME-79 data. J. Appl. Meteor., 21, 1594–1609.

Zhang, D.-L, and W.-Z. Zheng, 2004: Diurnal cycles of surface winds and temperatures as simulated by five boundary-layer parameterizations. J. Appl. Meteor., 43, 157-169.

Table 1        Measured calm and non-calm occurrences over the modeling domain during August 2002 based on NWS data

| Hour | #Non-Calm | #Calm | #Total | % Calm |
|------|-----------|-------|--------|--------|
| 00Z | 18209 | 3924 | 22133 | 17.7 |
| 01Z | 16531 | 6026 | 22557 | 26.7 |
| 02Z | 15604 | 6929 | 22533 | 30.8 |
| 03Z | 14983 | 7245 | 22228 | 32.6 |
| 04Z | 14309 | 7540 | 21849 | 34.5 |
| 05z | 14073 | 7735 | 21808 | 35.5 |
| 06Z | 13934 | 7949 | 21883 | 36.3 |
| 07Z | 13792 | 8040 | 21832 | 36.8 |
| 08Z | 13542 | 8273 | 21815 | 37.9 |
| 09Z | 13542 | 8385 | 21927 | 38.2 |
| 10Z | 13708 | 8591 | 22299 | **38.5** |
| 11Z | 14139 | 8693 | 22832 | 38.1 |
| 12Z | 15297 | 7690 | 22987 | 33.5 |
| 13Z | 17336 | 5192 | 22528 | 23 |
| 14Z | 18522 | 3439 | 21961 | 15.7 |
| 15Z | 18755 | 2617 | 21372 | 12.2 |
| 16Z | 19169 | 2015 | 21184 | 9.5 |
| 17Z | 19555 | 1617 | 21172 | 7.6 |
| 18Z | 19982 | 1430 | 21412 | 6.7 |
| 19Z | 20149 | 1389 | 21538 | 6.4 |
| 20Z | 20565 | 1288 | 21853 | 5.9 |
| 21Z | 20518 | 1383 | 21901 | 6.3 |
| 22Z | 20672 | 1556 | 22228 | 7 |
| 23Z | 20231 | 2292 | 22523 | 10.2 |
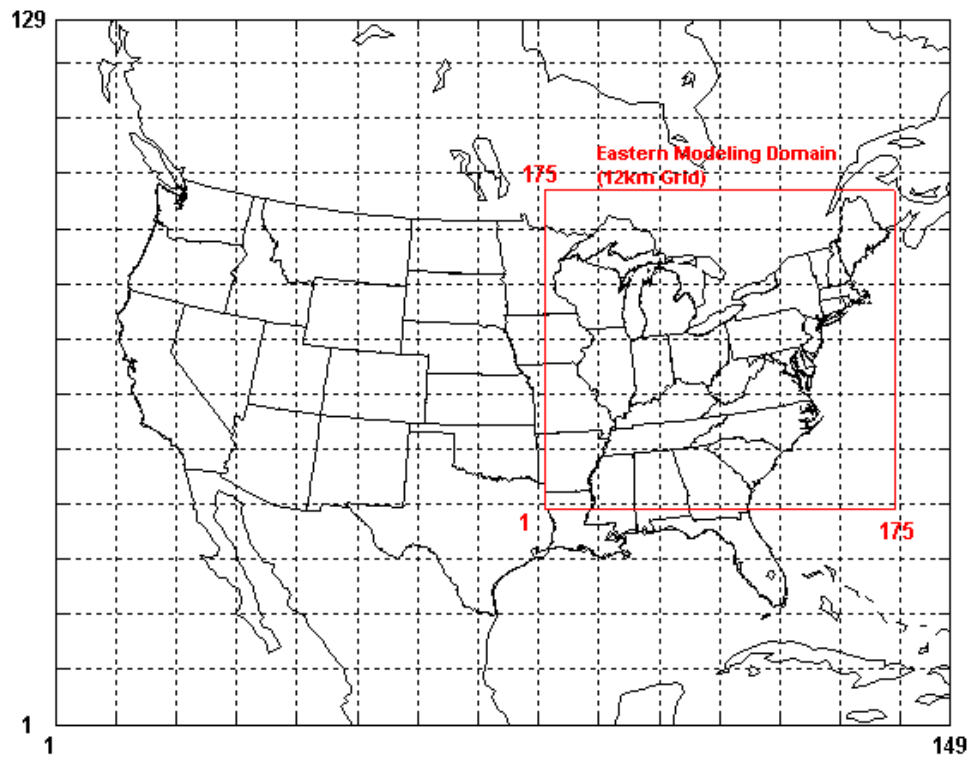
Figure 1: OTC MM5 modeling domain with areal extent of 12km and 36km grids
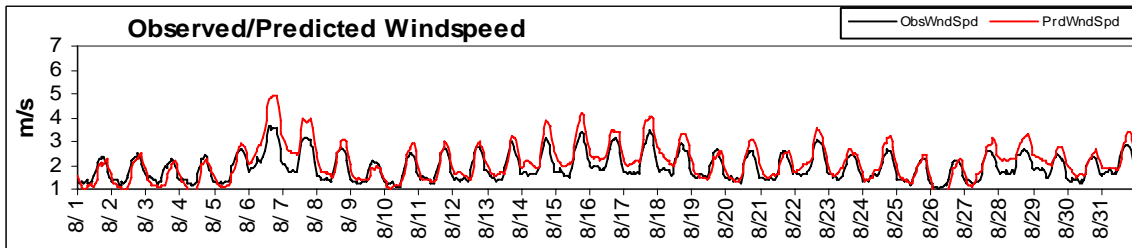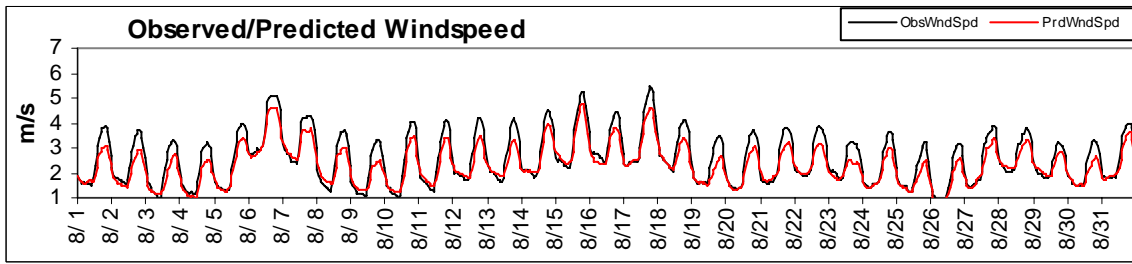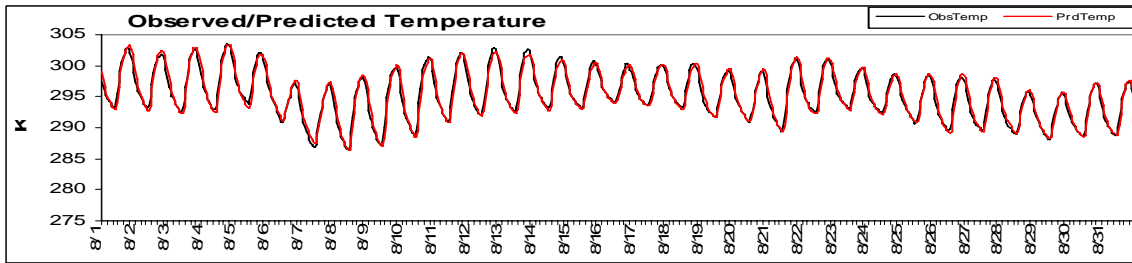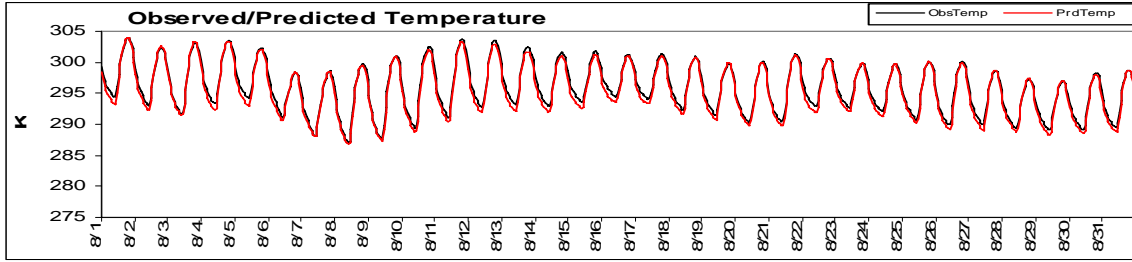
Figure 2: Temperature and Wind speed comparisons for August 2002. In each case the upper panel corresponds to comparison between MM5 and NWS data and the lower panel between MM5 and CASTNet data.

MM5 Sfc Wind Speed Correlation with TDL  May to Sept 2002

| | | | | | |
|---|---|---|---|---|---|
| 0.5 | 0.6 | 0.7 | 0.8 | 0.9 | |
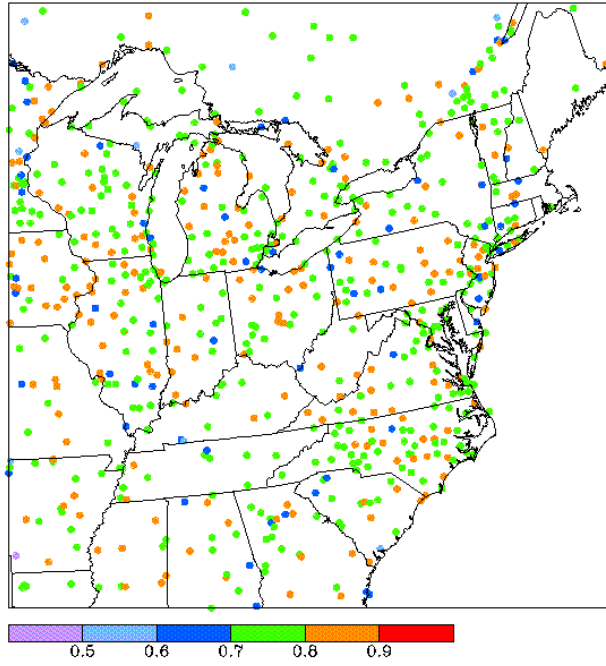
Figure 3a:    Spatial correlation estimates between MM5 and NWS data for wind speed
              from May to September 2002

MM5 Sfc Temperature Correlation with TDL   May to Sept 2002

0.90   0.92   0.94   0.96   0.98
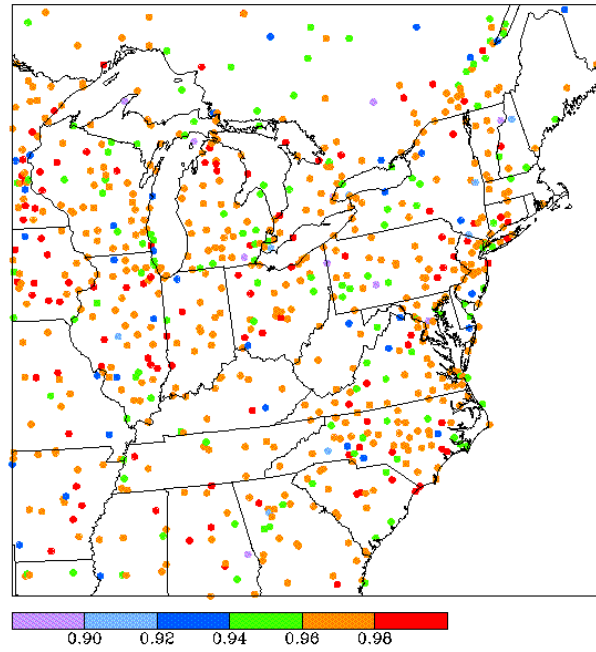
Figure 3b:    Spatial distribution of correlation coefficients for Temperature between
MM5 and NWS data from May to September 2002.

Richmond, VA
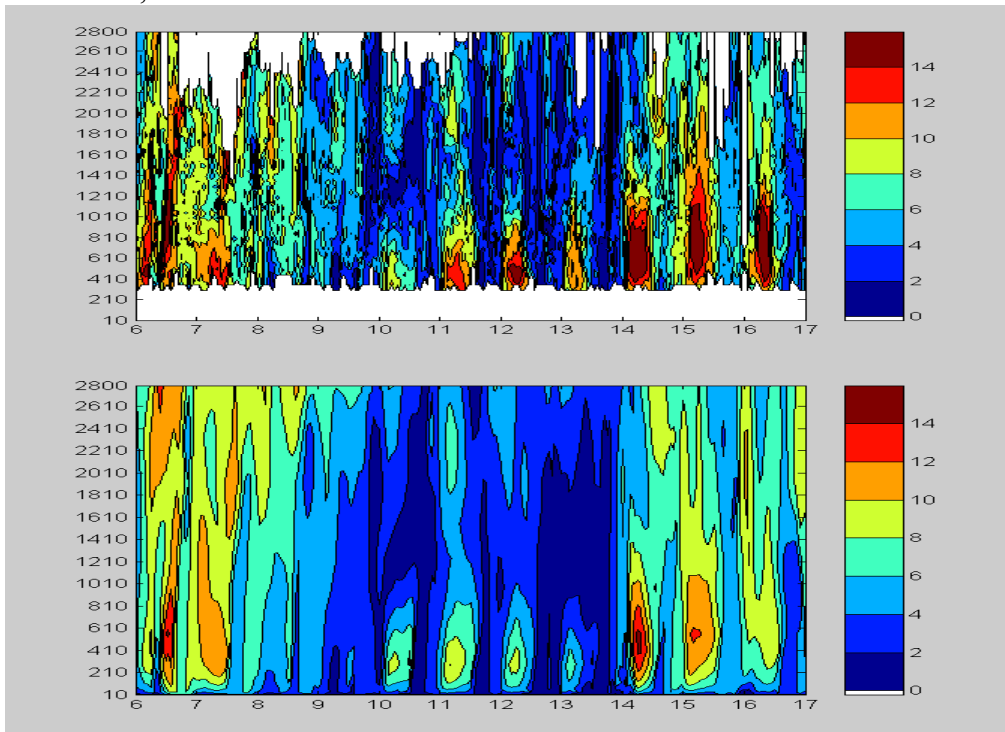


Concord, NH
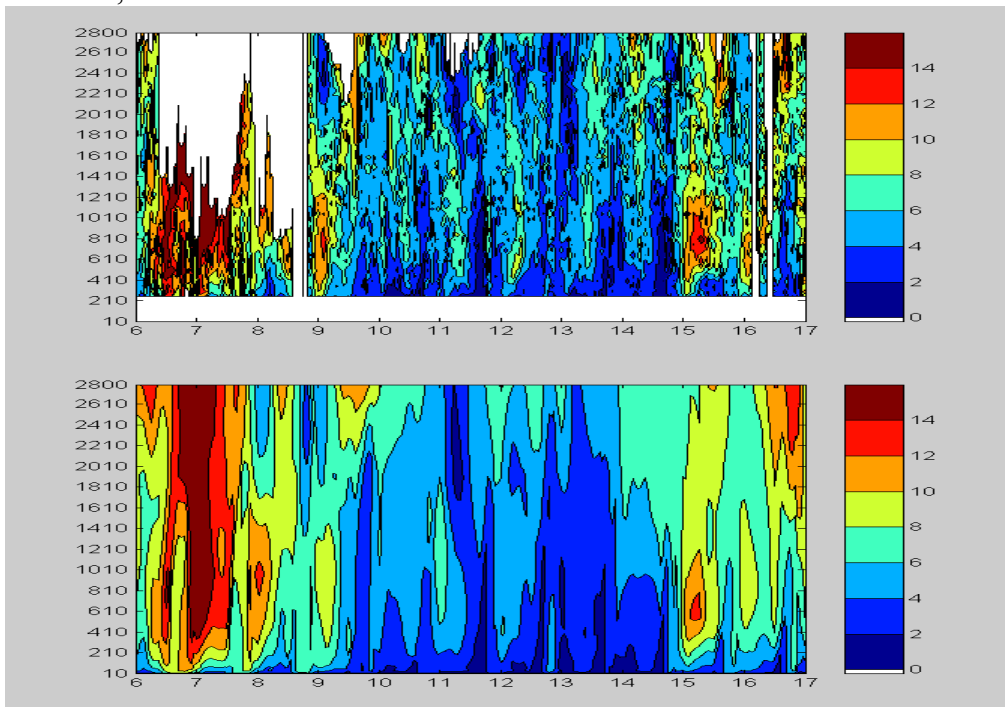


Figure 4: MM5 and Wind profiler comparison for August 6 to 17, 2002 at Richmond, VA and Concord, NH. The upper and lower panes at each station are for MM5 and profiler, respectively. The abcissa represents day and the ordinate the height (m).

13

## Observed Cloud
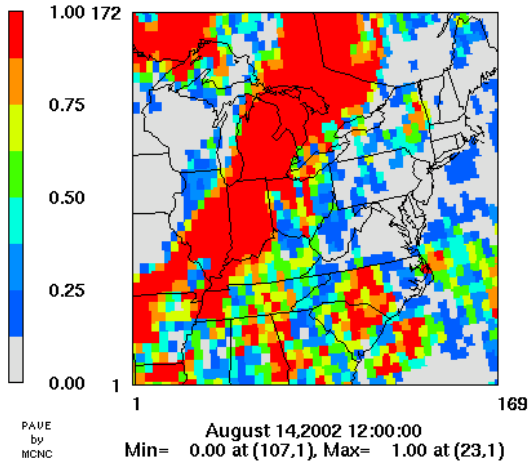


## MM5 Cloud
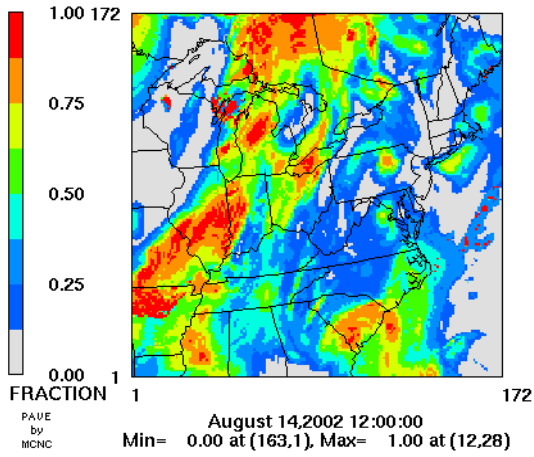


Figure 5: MM5 and Satellite cloud images for August 14, 2002 at 0700 EST
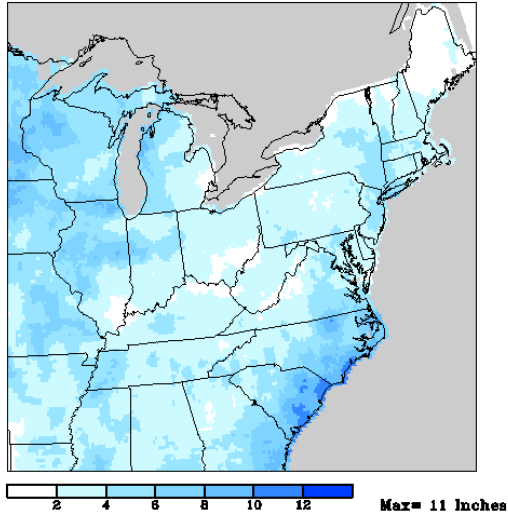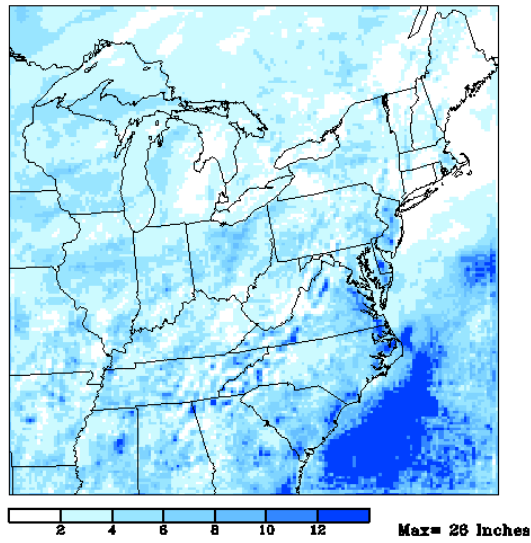
Figure 6: MM5 predicted and measured precipitation over the domain for the month of August 2002
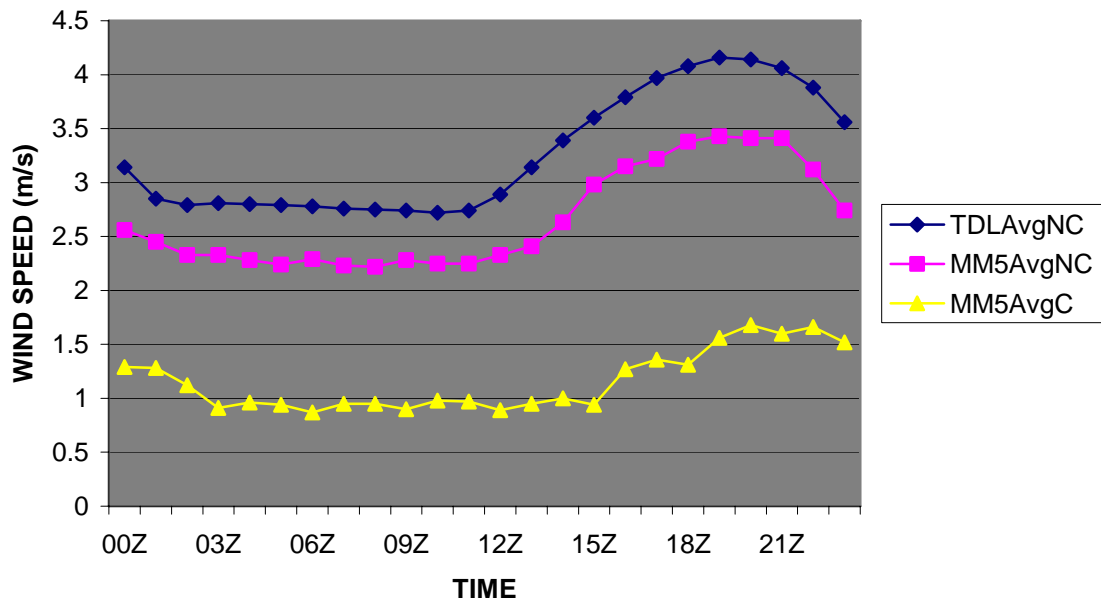
Figure 7: Comparison of averaged wind speed between MM5 and observed under calm (C) and non-calm (NC) conditions.

**Analysis of MM5 Simulations based on three PBL schemes over the eastern US for August 6 to 16, 2002**

**Winston Hao, Mike Ku, and Gopal Sistla**
**NYSDEC-DAR**
**Albany, NY 12233**

***Introduction:*** In a prior report[1] dated December 8, 2003, a comparison was performed between meteorological measurements and the simulated MM5 fields for August 6 to 16, 2002 based upon 3 approaches to the PBL. In this report, we provide the comparison with TDL and CASTNet measurements.

***Purpose:*** The intent of this exercise was to investigate the response of three PBL schemes and develop a recommendation for the use of a PBL method for developing meteorological fields for the May through September of 2002, in support of air quality modeling work.

***Approach:*** In this study, Prof. Dalin Zhang of University of Maryland, applied 3 PBL schemes for the August 6 to 16, 2002, a period in which the OTR experienced high ozone as well as particulate levels. The three schemes were (a) modified Blackadar [BL], (b) the Pleim-Xiu scheme with the soil module [PX], and (c) modified Blackadar with soil module [SSIB]. The simulated meteorological fields were compared to the measurements from TDL (NWS) and CASTNet.

***Model setup:*** The MM5 model setup is similar to the earlier exercise of developing meteorological fields for July 1997, with the first level at 10 m. The projection for this exercise was that recommended by the RPOs, and has a spatial resolution of 12 km (see Figure 1)

***Analysis:*** The basic approach used is to compare domain-wide averaged measurements and predictions for surface temperature, wind speed and direction, and where available with humidity. While the CASTNet sites are more representative of rural areas, the TDL are reflective of urban/suburban settings. There are 47 CASTNet and about 600 NWS sites in the TDL data set over the modeling domain.

***TDL data and MM5 simulations:***

**Average wind speed and direction** (see Figures 2a through 2c)

---

[1] Hao, W., Ku, M., and Sistla, G. (2002) 'Preliminary analysis of MM5 simulations for the August 6 to 17, 2002 – A status report', NYSDEC, Albany, NY 12233

Overall, the 3 PBL schemes provide good agreement with the observed average wind direction . In terms of wind speed:

BL:    Under prediction of daytime maximum wind speed, but agreement with nighttime low windspeed

P-X:    Systematic under prediction during daytime and over prediction in the nighttime

SSIB:  Under prediction during daytime with phase lag, the predicted maximum occurring latter than the measured maximum

**Temperature** (see Figures 3a through 3c)

BL:    Good agreement throughout the episode days

P-X:    Initial over prediction of temperature minimum, and under prediction of daytime maximum

SSIB:  Over prediction of daytime maximum

**Humidity** (see Figures 4a through 4c)

BL:    While the general trend is captured during the episode, there is poor agreement between the observed and predicted diurnal patterns, with the observation showing a double peak versus one peak based on predictions.

P-X:    The model yields the observed daily double peak, but with underprediction and a phase lag.

*CASTNet data and MM5 simulations:*

**Average wind speed and direction** (see Figures 5a through 5c)

All 3 PBL approaches provide good agreement with the observed average wind direction. In terms of wind speed:

BL:    Wind speed over prediction during the daytime, a feature that differs from the TDL results, but good agreement with nighttime minimum

P-X:    Wind speed over prediction, for both day- and nighttime hours.

SSIB:   Wind speed over prediction at the start and end of the episode, and exhibiting a phase-lag of 1 to 2 hours

**Average Temperature** (see Figures 6a through 6c)

BL:    Overall good agreement

P-X:    Systematic under prediction during daytime and over prediction in the nighttime with phase lag

SSIB:  Over prediction during the daytime, but good agreement during nighttime

**Average Humidity**

There were no data to perform this comparison, as mixing ratio cannot be estimated due to lack of station pressure.

*Spatial distribution of correlation between TDL data and MM5 simulations*

**Wind Speed** (see Figures 7a through 7c)
BL:     The correlation levels are generally in the 0.7 or higher range over most portions of the domain, with lower values mainly confined to the southeastern and western parts of the domain.
P-X: The correlation levels are slightly lower compared to BL, with more stations exhibiting a correlation level of less than 0.6 in the Southeastern portion of the domain.
SSIB: The correlation levels are similar to P-X, but with increased number of stations exhibiting correlation levels less than 0.6 over the domain

**Temperature** (see Figures 8a through 8c)
BL:     The correlation levels are generally higher (>0.97) over the northeastern portions of the domain, with the remainder of the domain exhibiting correlation levels in the range of 0.94 to 0.96
P-X:    Overall the correlation levels are slightly lower than BL
SSIB:  Similar to P-X, with correlation levels in the 0.95 throughout the domain

**Humidity** (see Figures 9a through 9c)
BL:     The correlation levels over the northeast are generally higher than the rest of the domain, although most portions of the domain report correlation of 0.70 or higher
P-X:    The correlation levels are comparable or slightly better than BLK
SSIB:   The correlation levels are comparatively lower than the other two over the northeastern portions of the domain

*Discussion and conclusions*

On an overall basis, it appears that the BL scheme exhibits a better correspondence to the measured data than the other two schemes. The exception being the poor capture of the observed diurnal pattern of humidity in the case of the BL scheme. While the P-X scheme shows a better correspondence with the observed diurnal pattern for humidity, it fails to perform well for wind speed and temperature. Further work is needed to improve the performance of these methods. An examination of other studies in which the P-X scheme was applied suggests the predictive performance is similar to this study.

Other comparisons of model to observed or measured parameters such as cloud cover, precipitation, and upper air soundings/profiler network are under examination to provide a comprehensive evaluation of the meteorological model. Also, the use of the model simulated fields in air quality model and comparison to pollutant fields is also in progress.

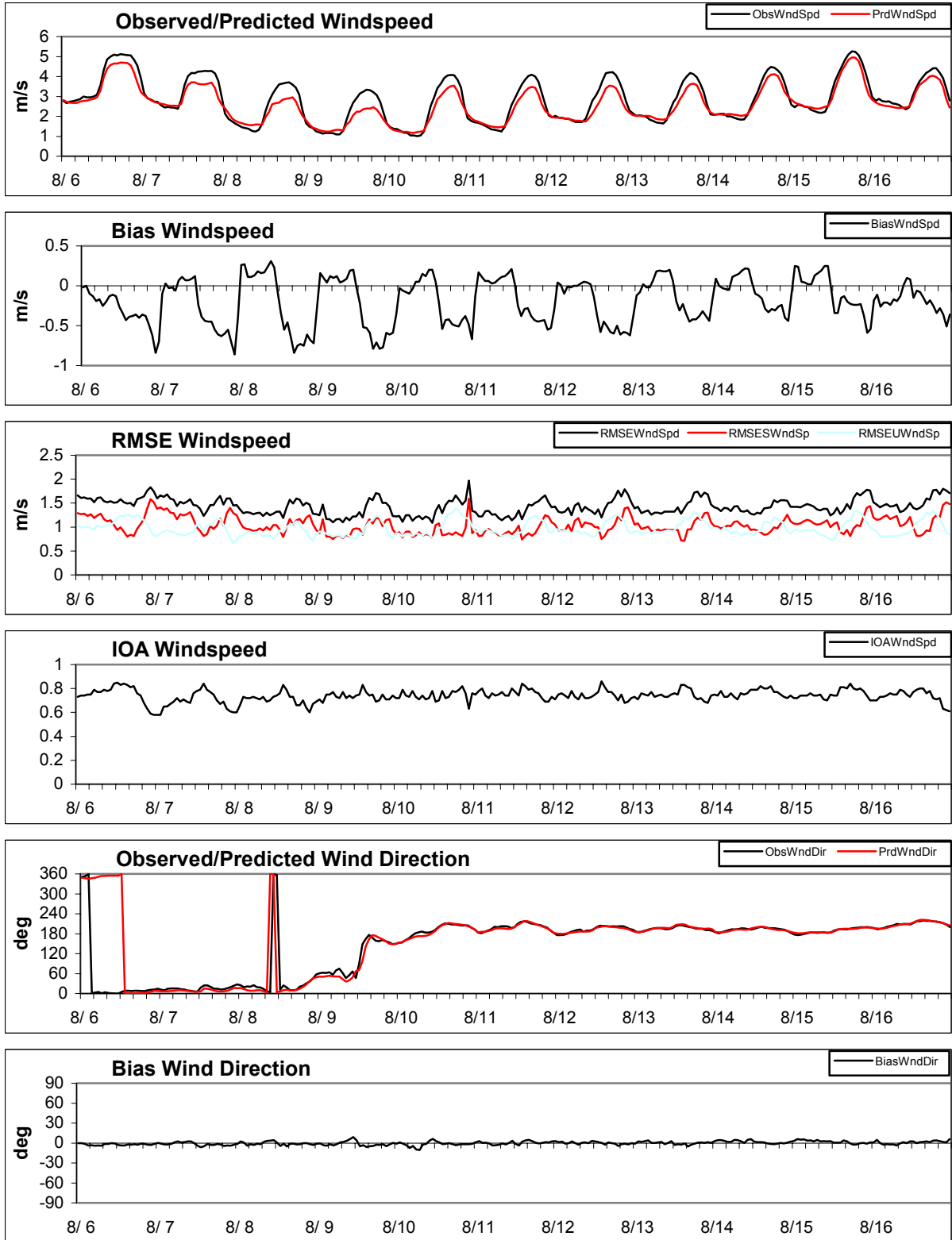# Figure 2a  MM5 Simulation - UMD BLK & TDL - Aug 6 01Z to Aug 17 00Z 2002



4

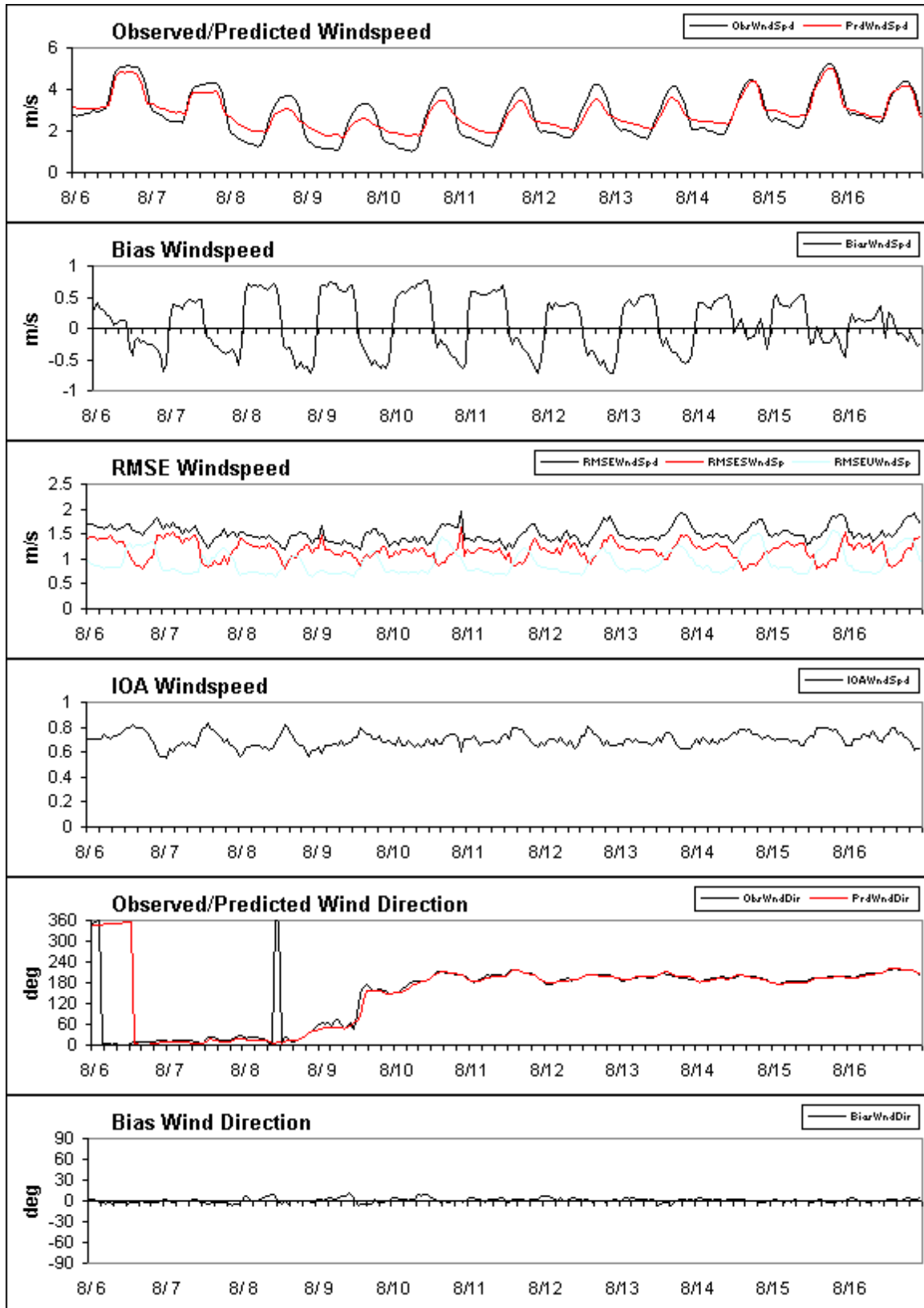**Figure 2b MM5 Simulation - UMD PX & TDL Aug 06 01Z to Aug 17 00Z 2002**

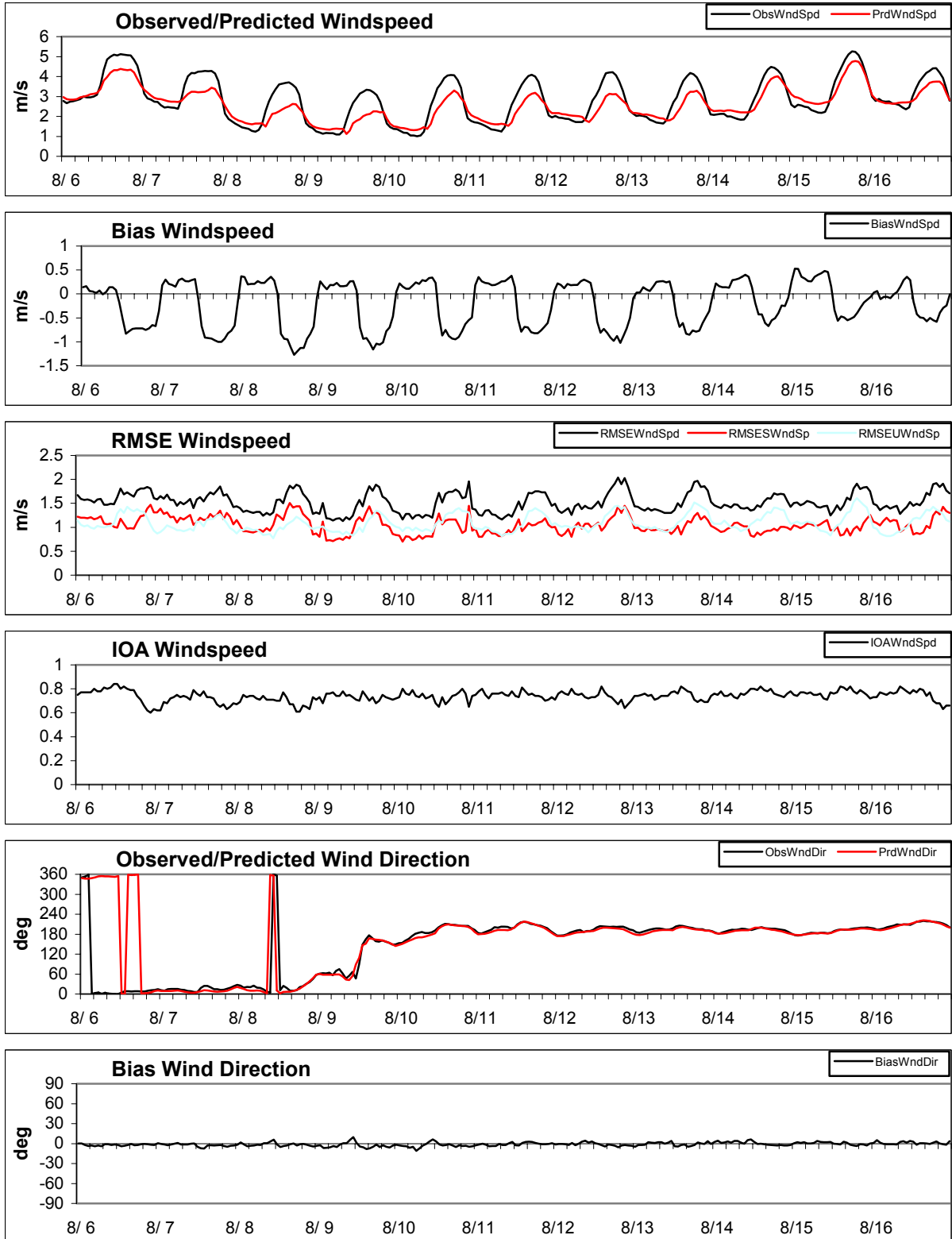# Figure 2c MM5 Simulation - UMD SSIB & TDL Aug 06 01Z to Aug 17 00Z 2002

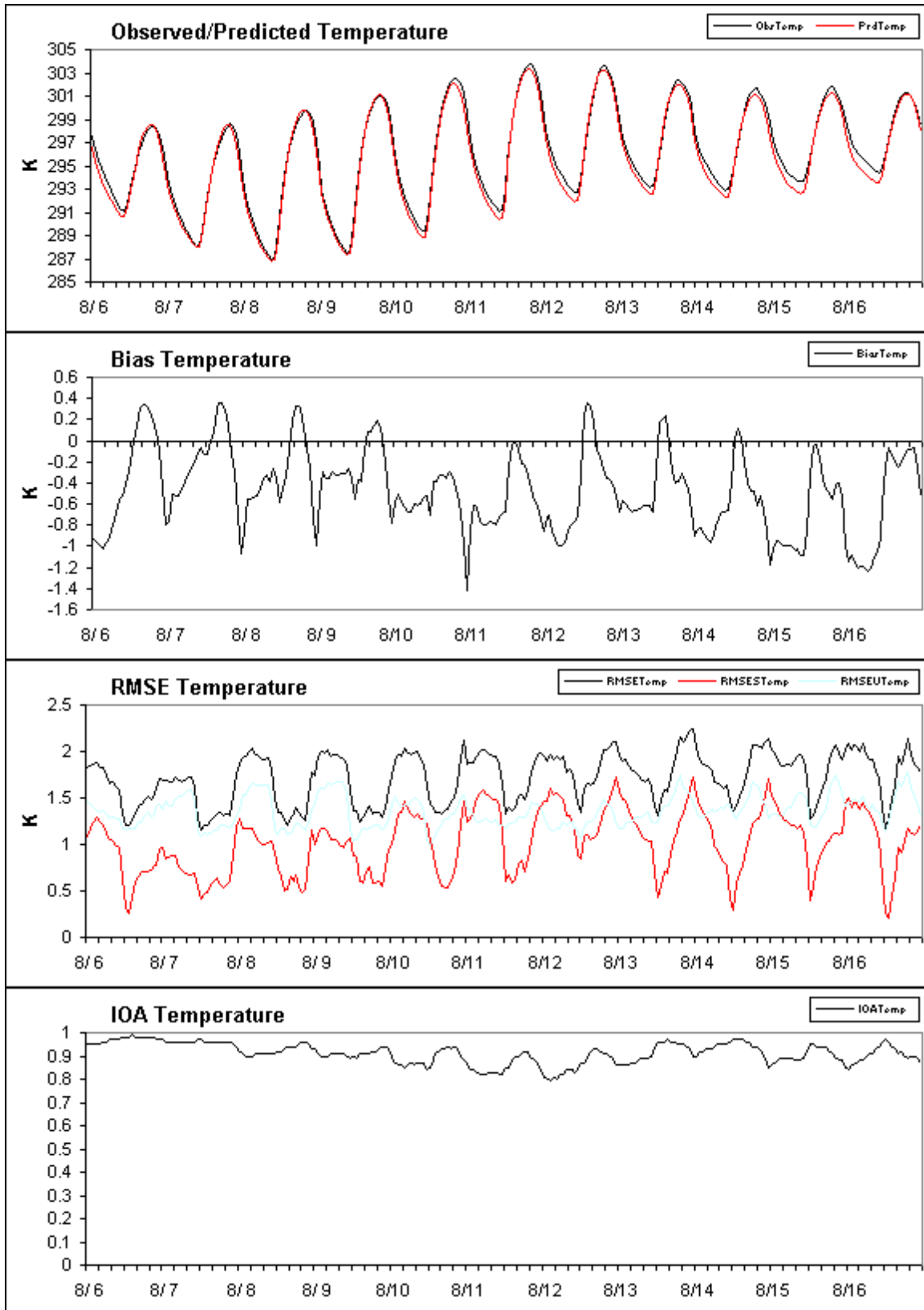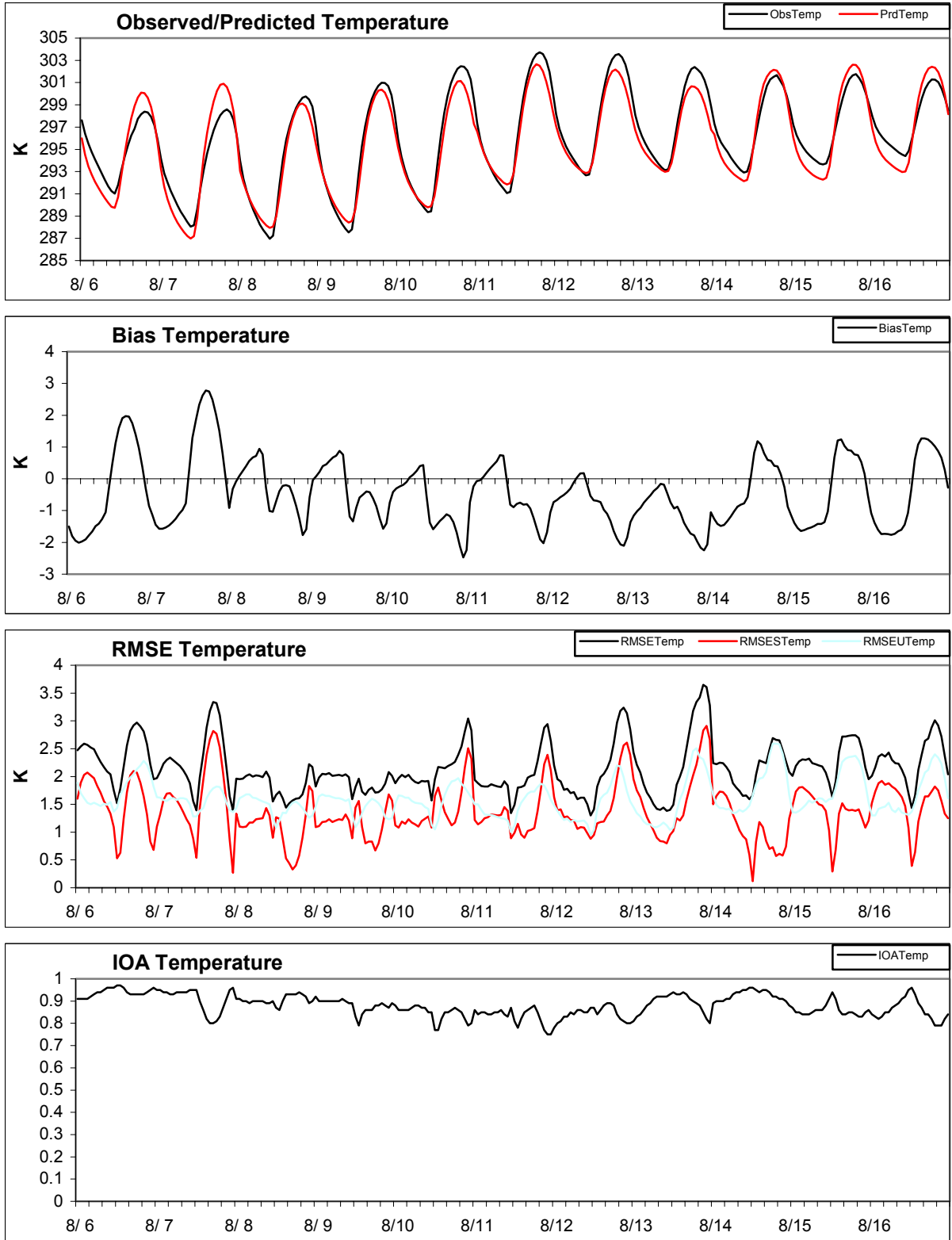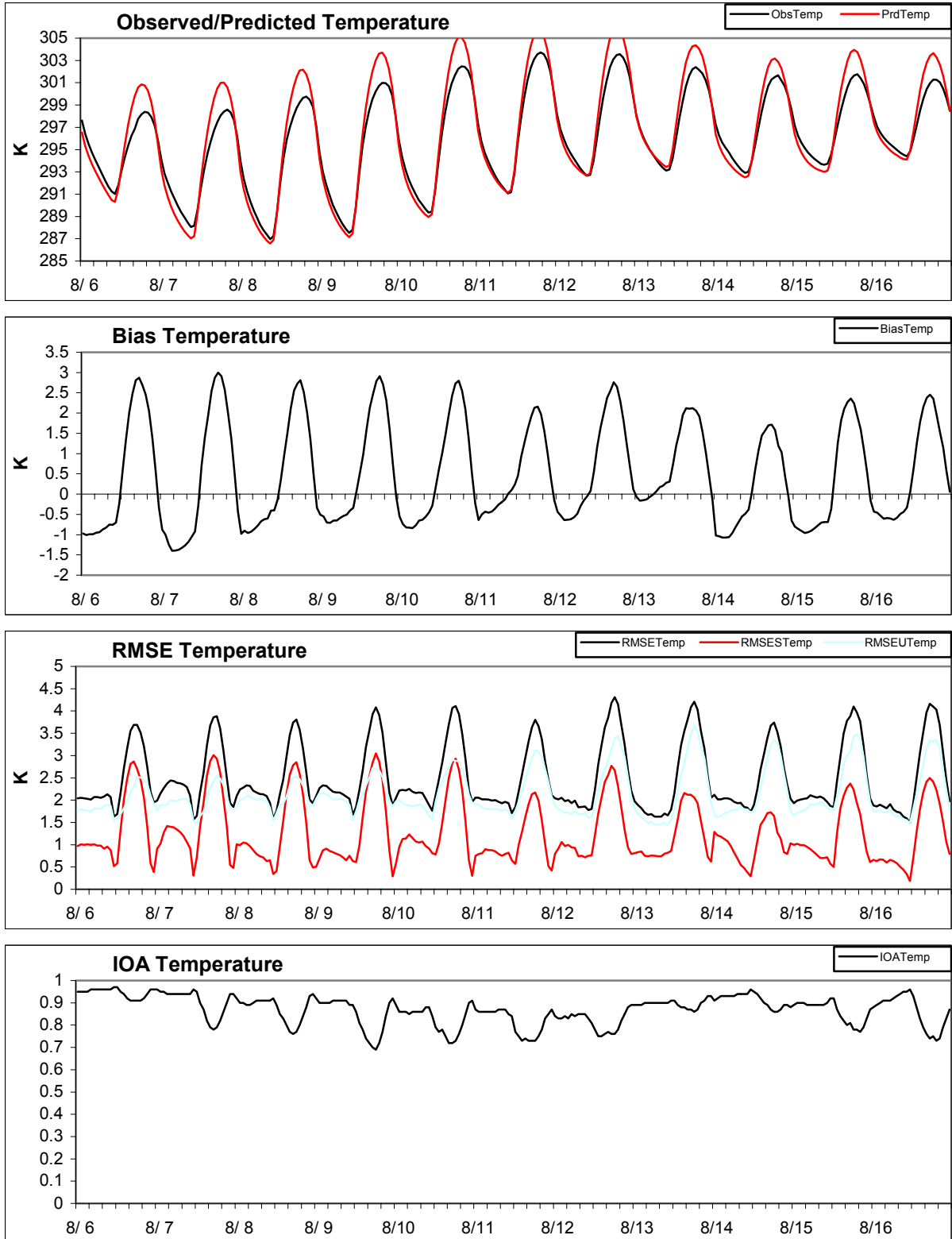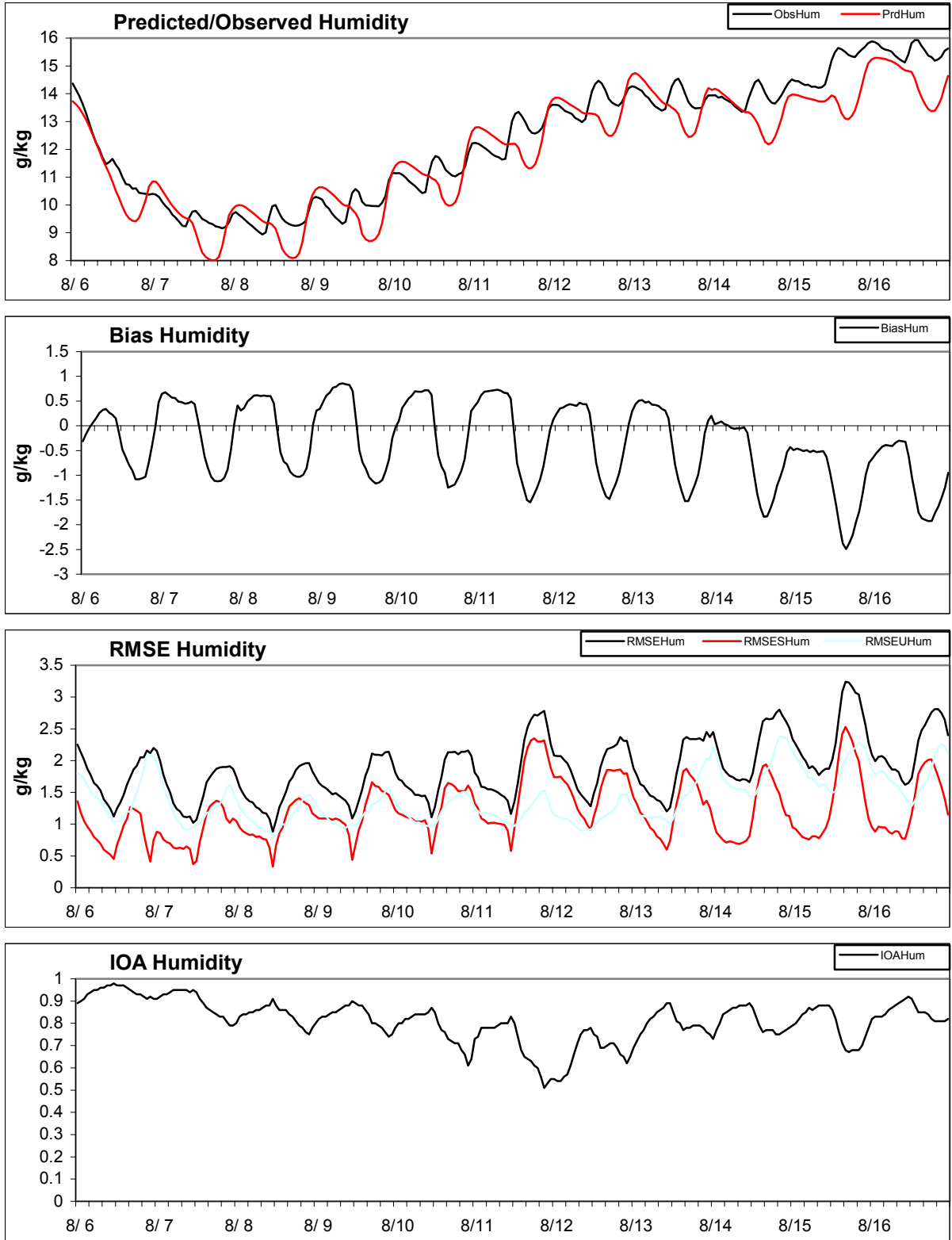**Figure 3a MM5 Simulation - UMD BL & TDL Aug 6 01Z to Aug 17 00Z 2002**

# Figure 3b MM5 Simulation - UMD PX & TDL Aug 06 01Z to Aug 17 00Z 2002

**Figure 3c MM5 Simulation - UMD SSIB & TDL Aug 06 01Z to Aug 17 00Z 2002**

**Figure 4a MM5 Simulation - UMD BL & TDL Aug 6 01Z to Aug 17 00Z 2002**
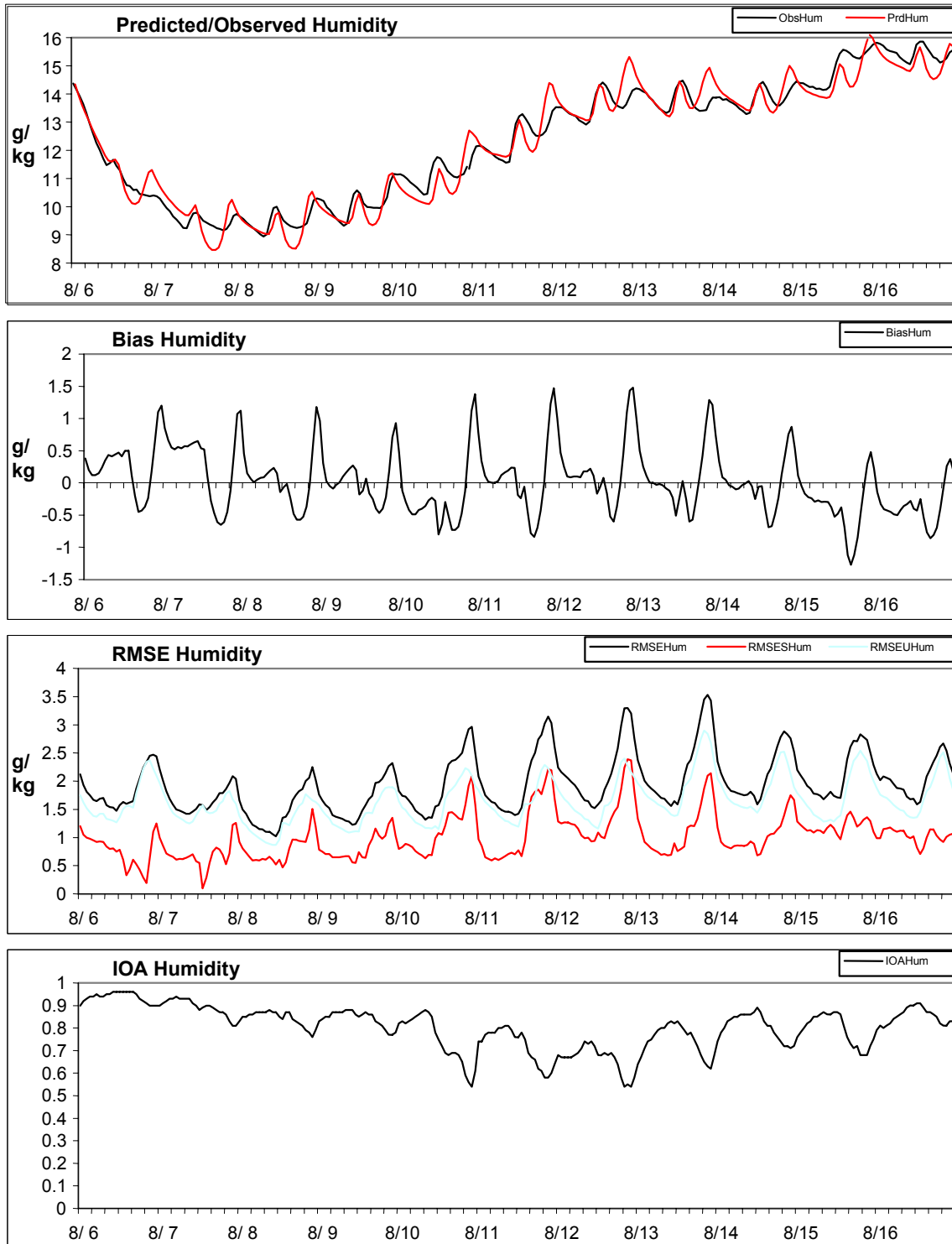
**Figure 4b MM5 Simulation - UMD PX Aug 06 01Z to Aug 17 00Z**

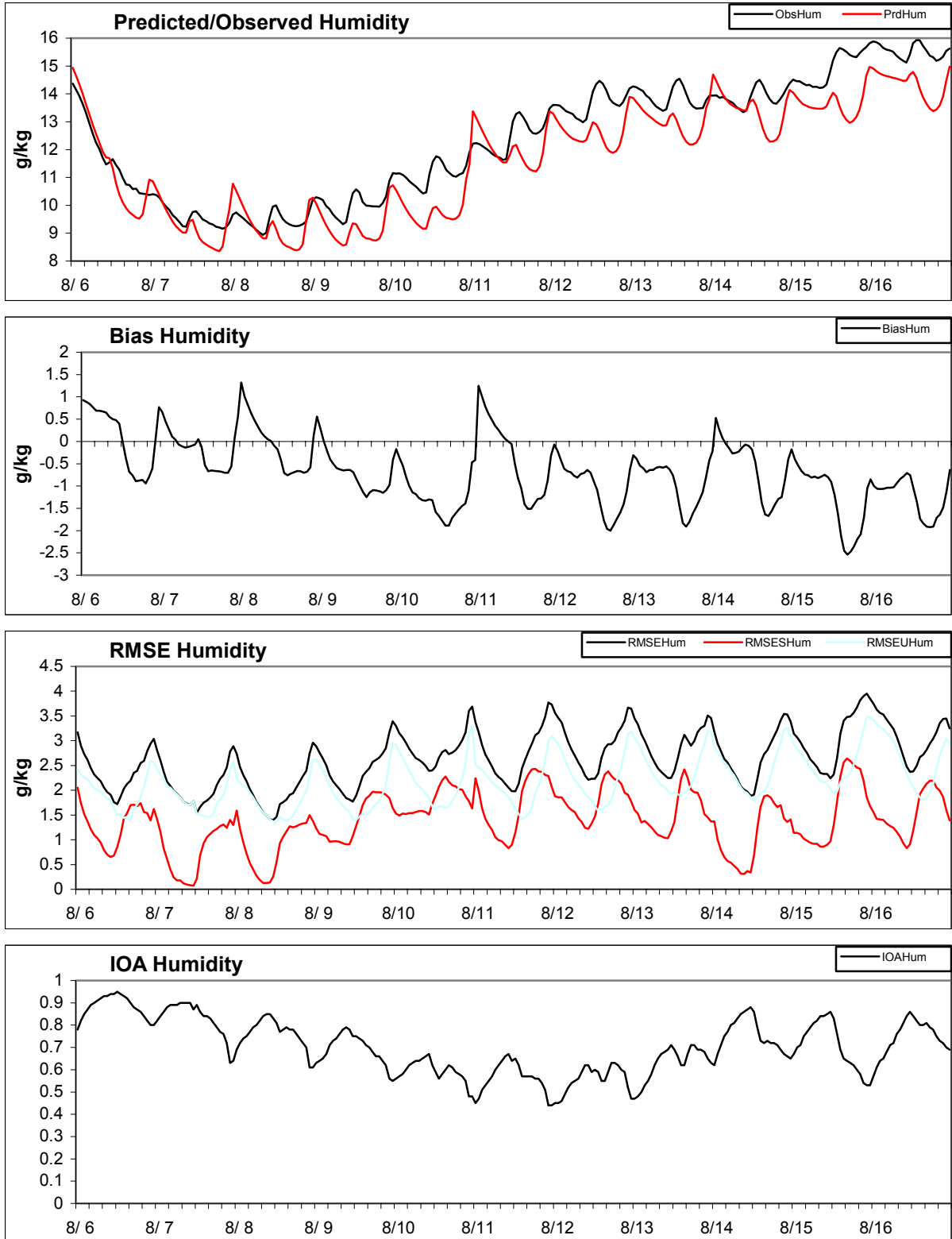**Figure 4c MM5 Simulation - UMD SSIB & TDL Aug 06 01Z to Aug 17 00Z 2002**

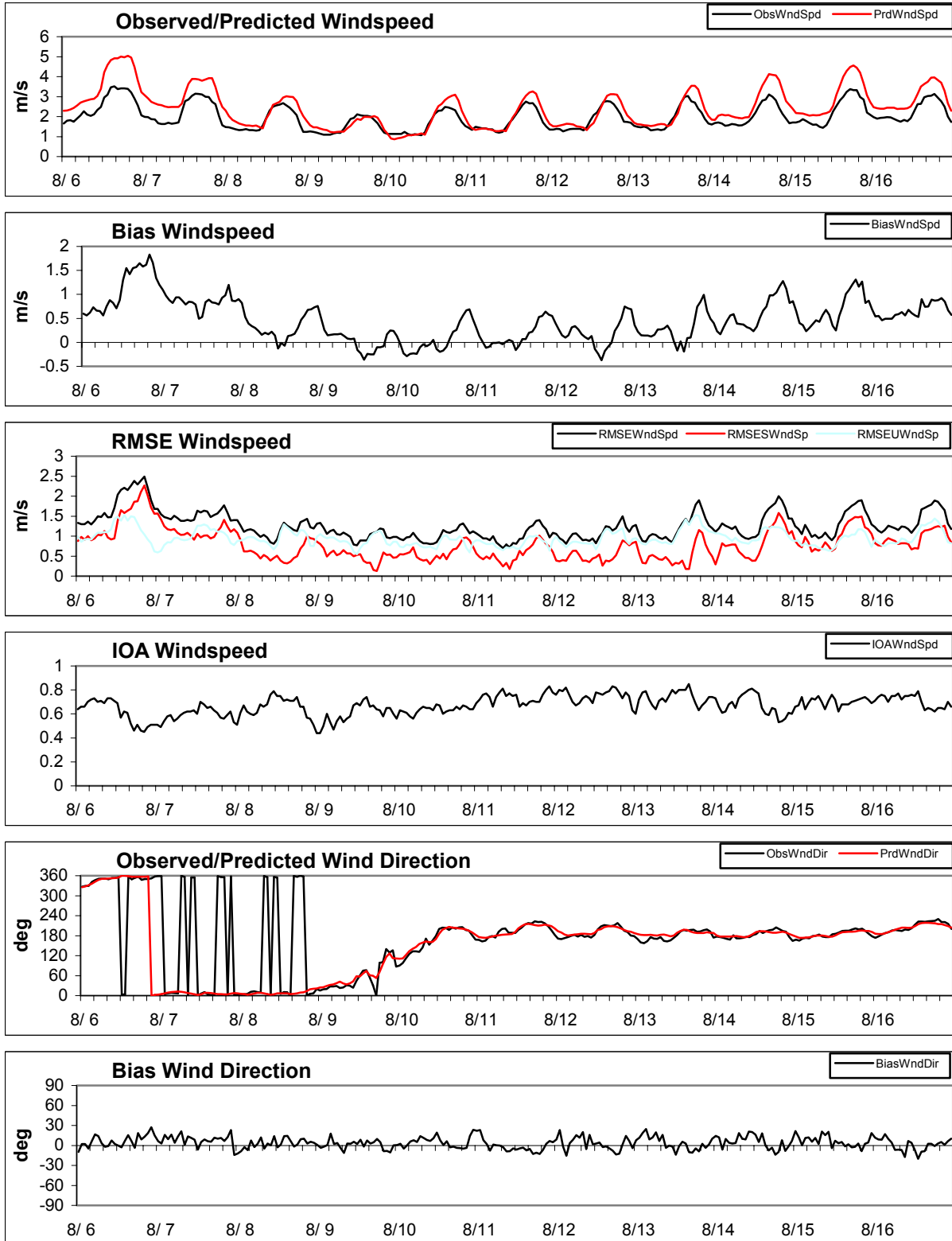# Figure 5a   MM5 UMD - BL & CASTNet Aug 6 01Z to Aug 17 00Z 2002



13

# Figure 5b  MM5 - UMD PX & CASTNet Aug 06 01Z to Aug 17 00Z 2002
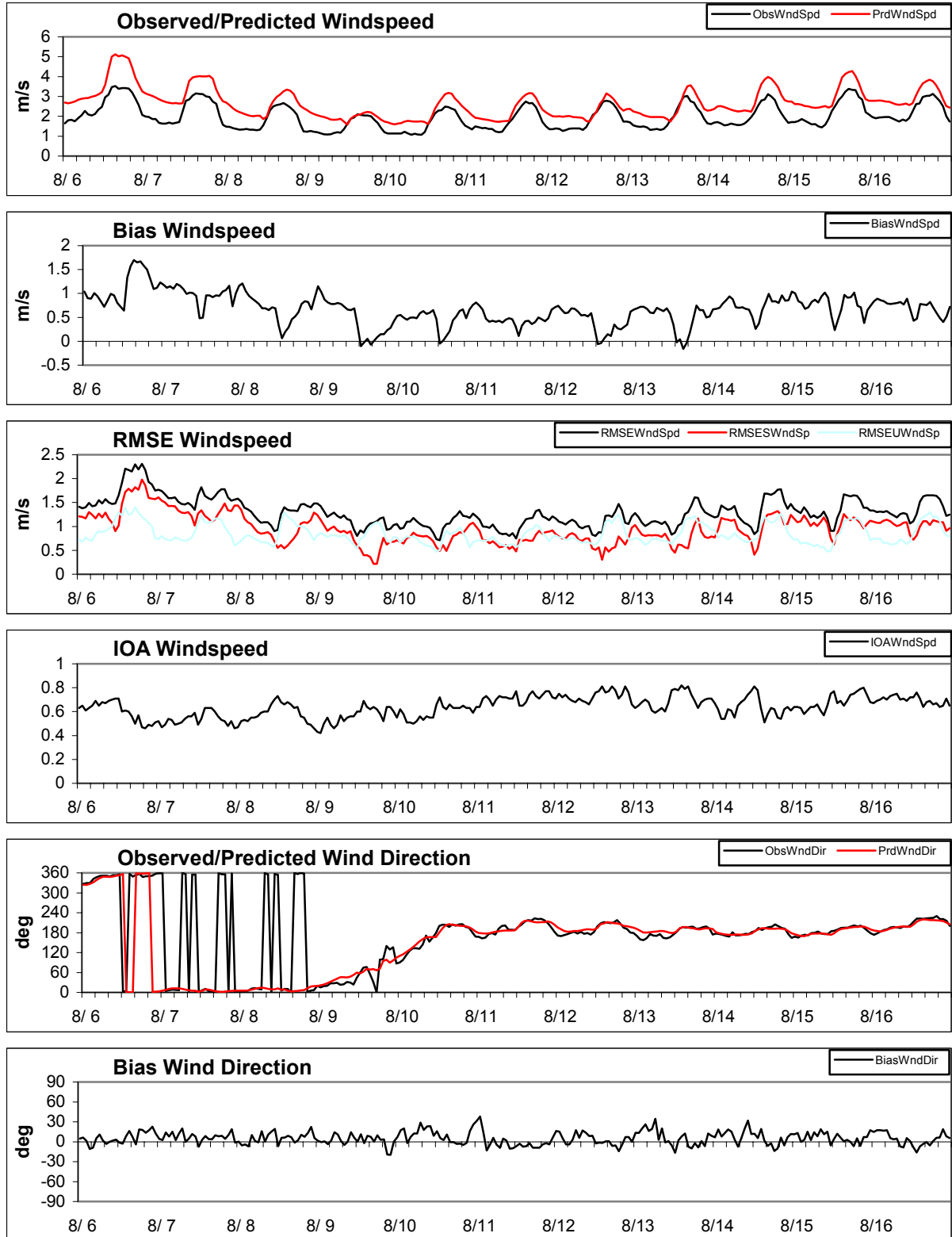


14

# Figure 5c MM5 - UMD SSIB & CASTNet Aug 06 01Z to Aug 17 00Z 2002
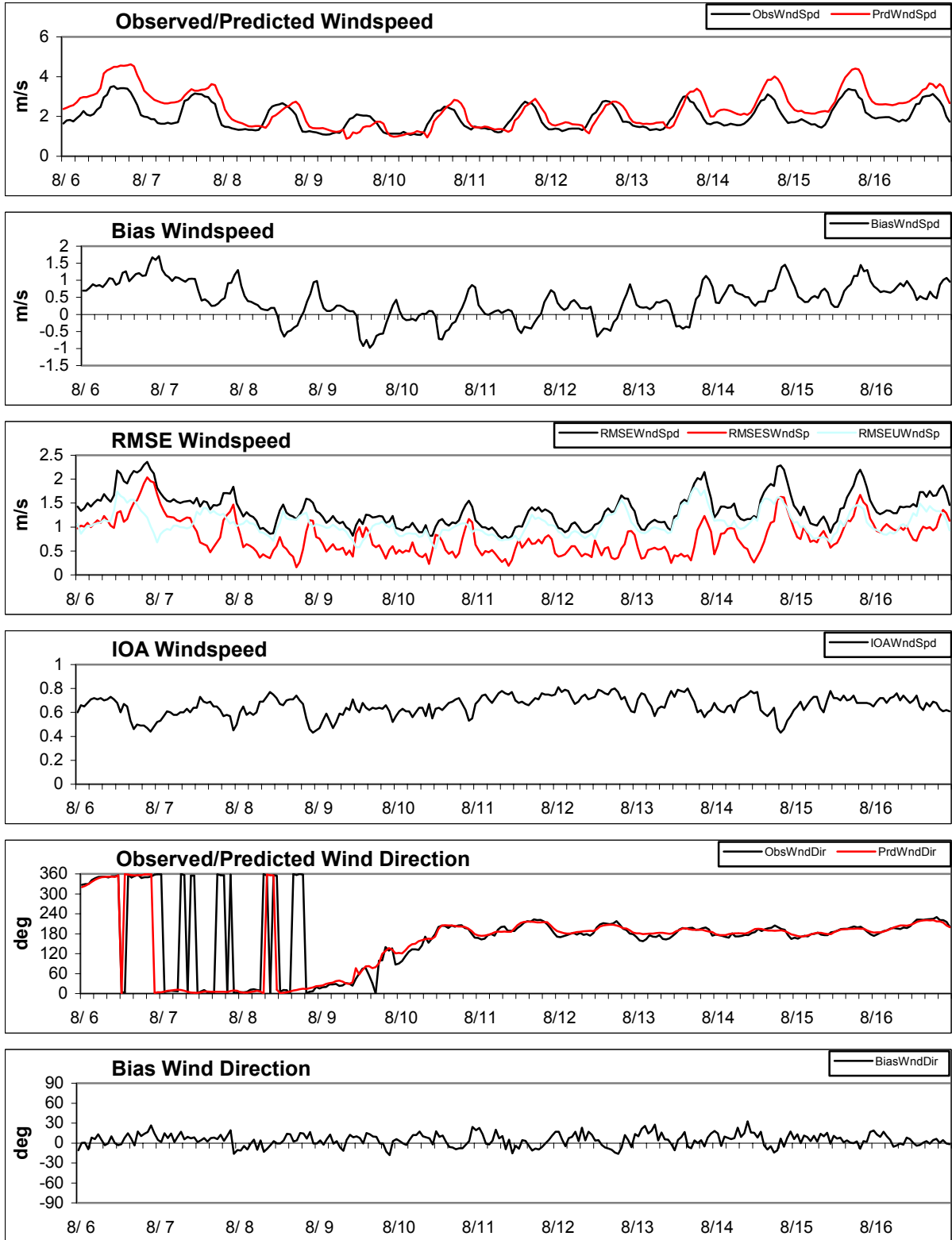


15

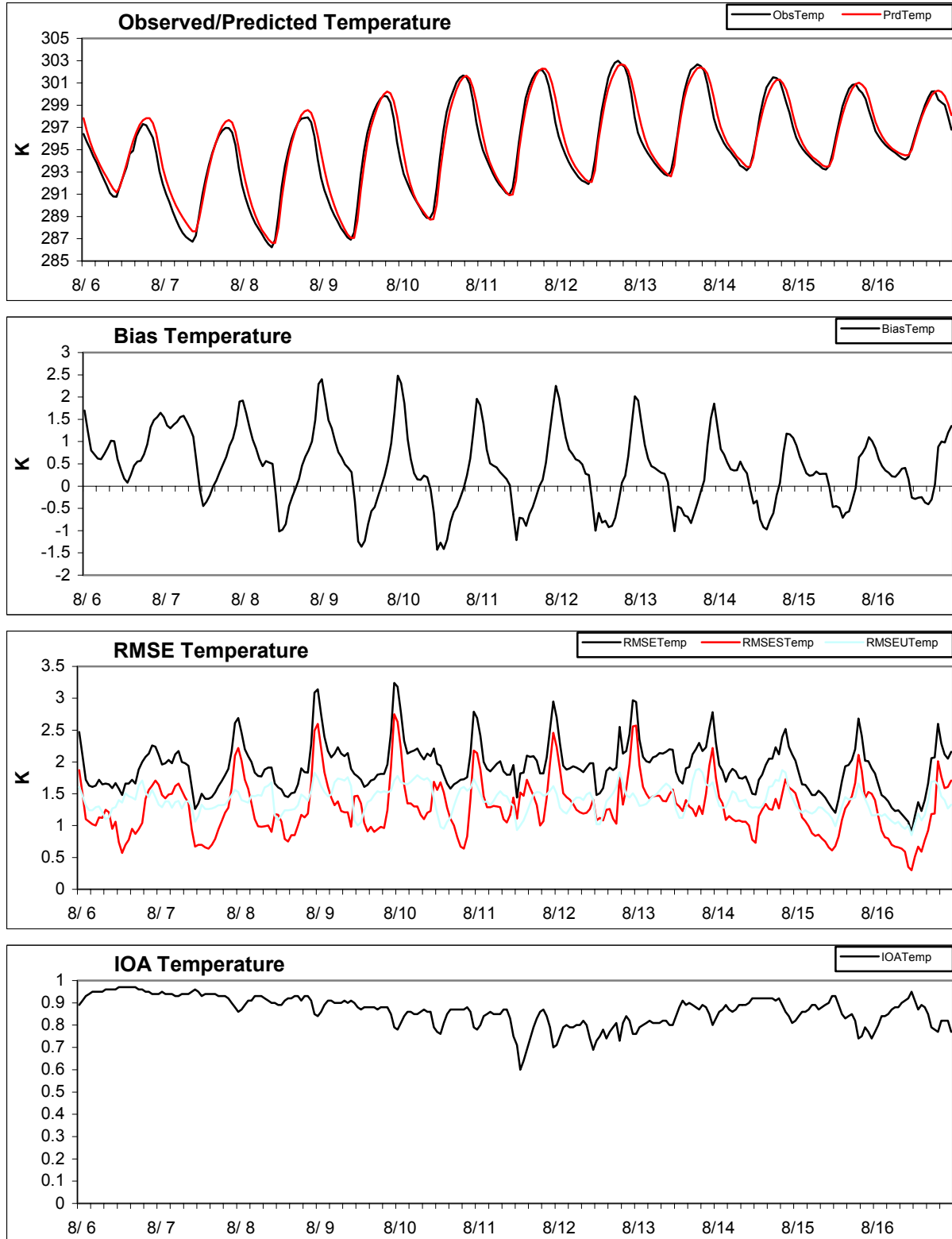# Figure 6a   MM5 - UMD BL  & CASTNet Aug 6 01Z to Aug 17 00Z 2002

# Figure 6b  MM5 - UMD PX  & CASTNet Aug 06 01Z to Aug 17 00Z 2002



17

# Figure 6c  MM5 - UMD SSIB & CASTNet  Aug 06 01Z to Aug 17 00Z 2002
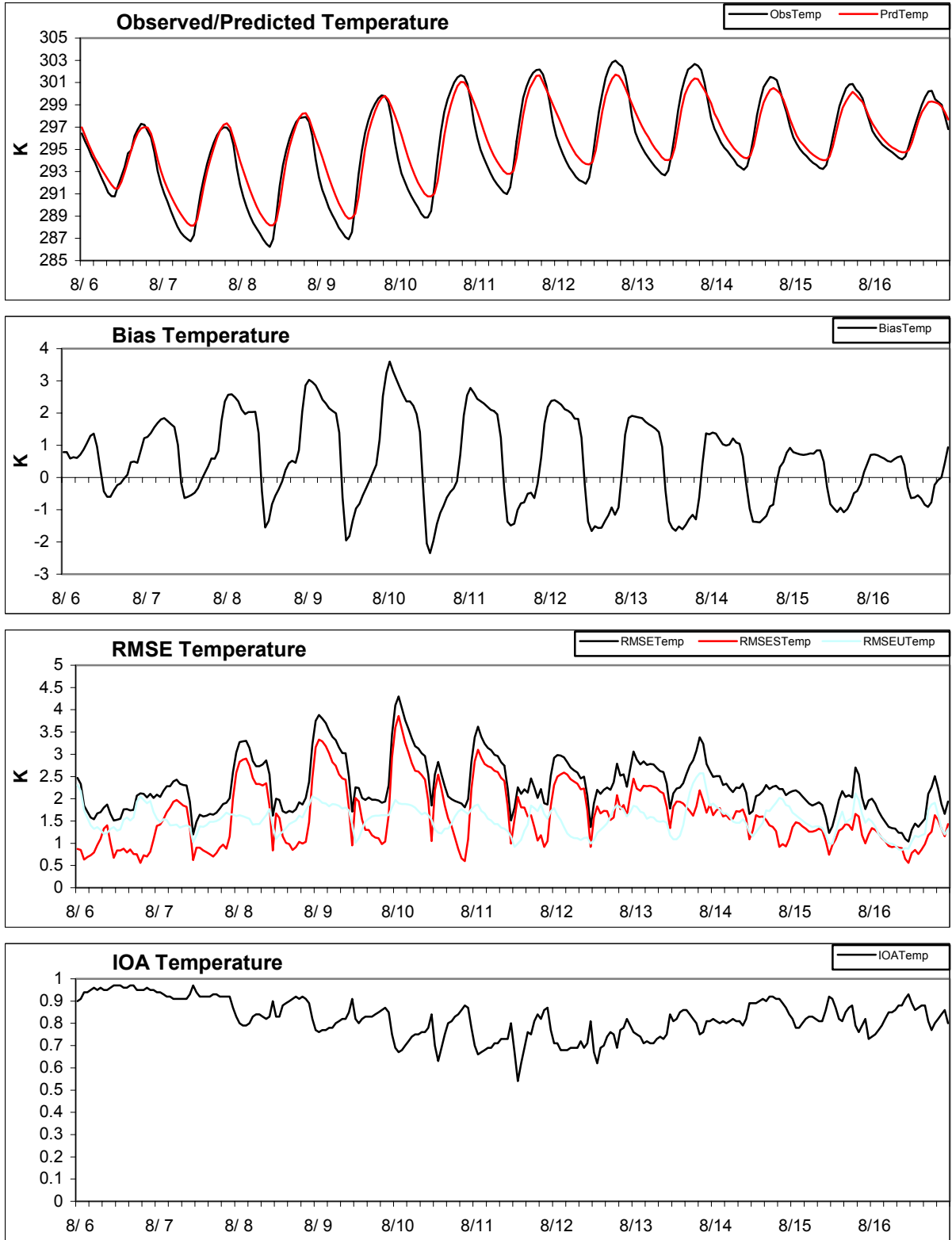
Figure 7a Spatial Correlation – Wind speed – BL  & TDL

UMD 2002 MM5 BL Wind Speed Correlation with TDL



| 0.3 | 0.4 | 0.5 | 0.6 | 0.7 | 0.8 | 0.9 |
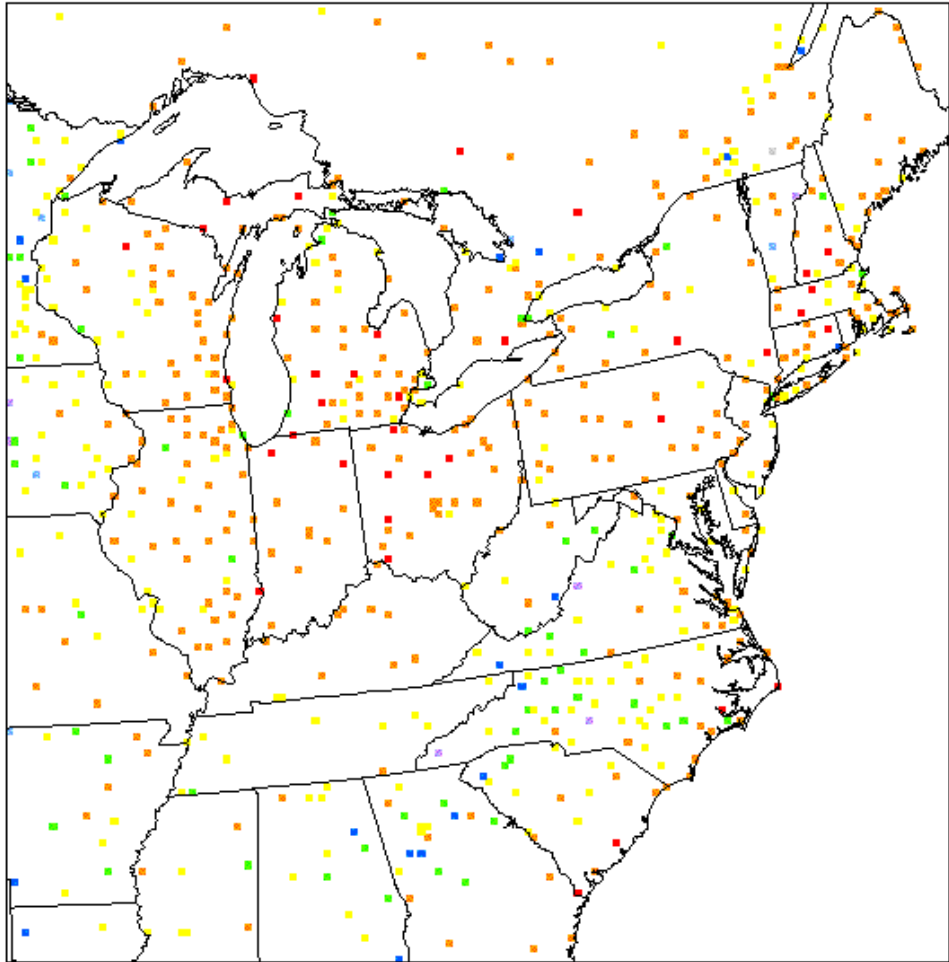
Figure 7b  Spatial Correlation – Wind Speed – P-X & TDL



UMD 2002 MM5 PX Wind Speed Correlation with TDL
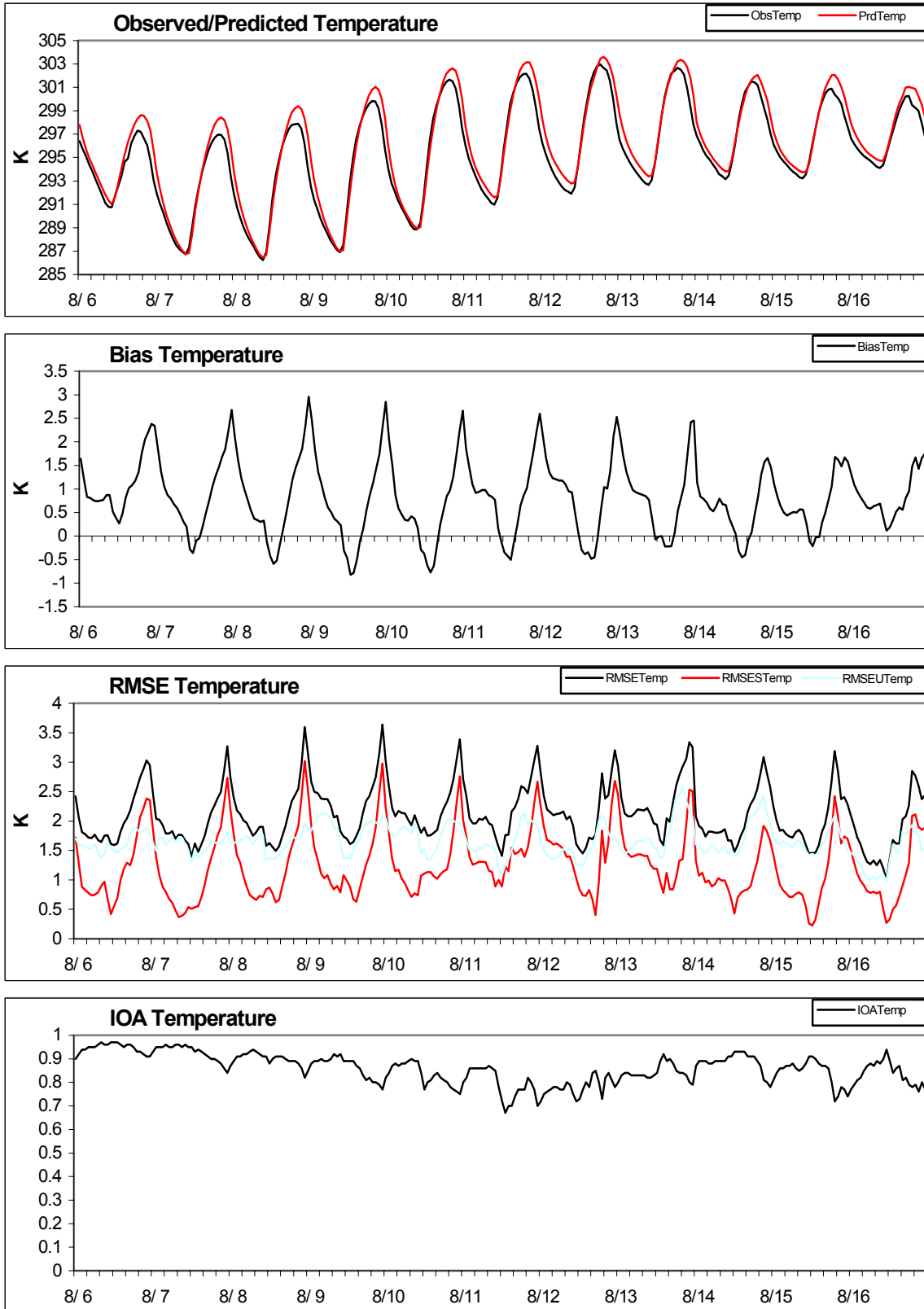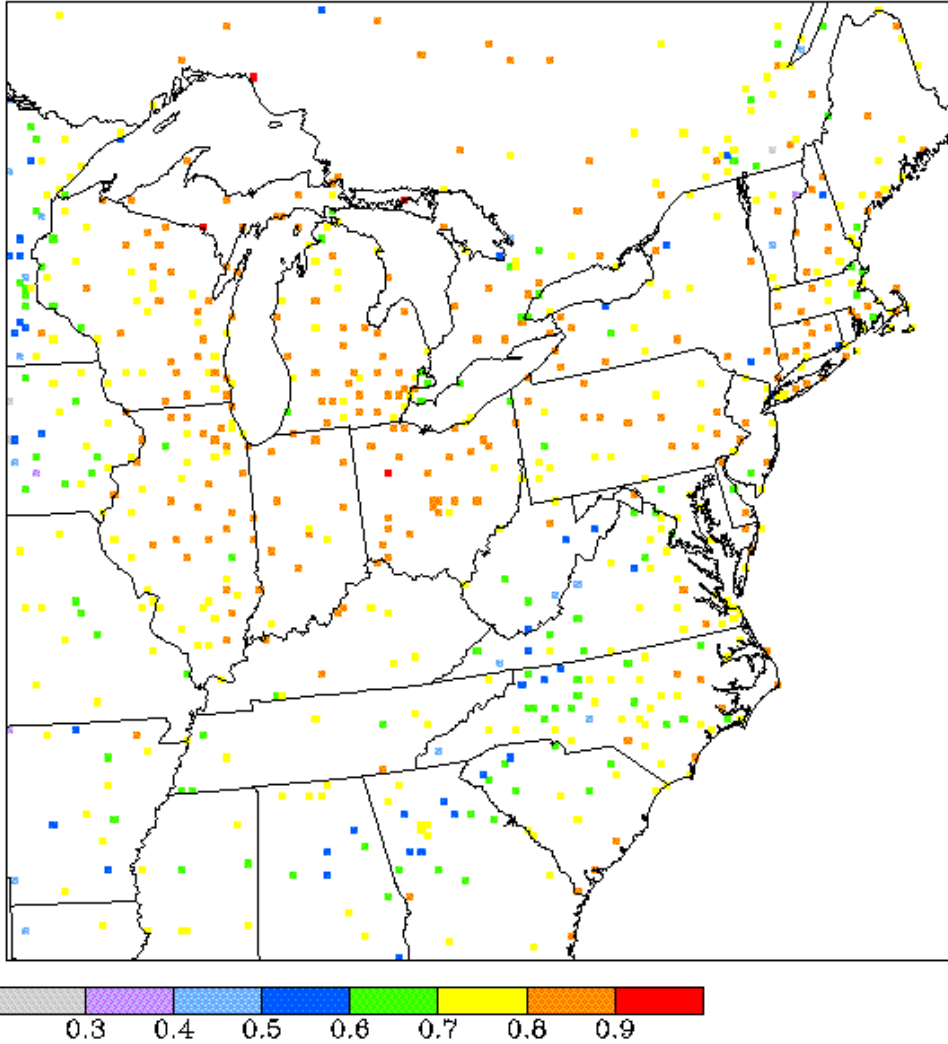
Figure 7c  Spatial Correlation – Wind Speed  SSIB  & TDL

UMD 2002 MM5 SSiB Wind Speed Correlation with TDL
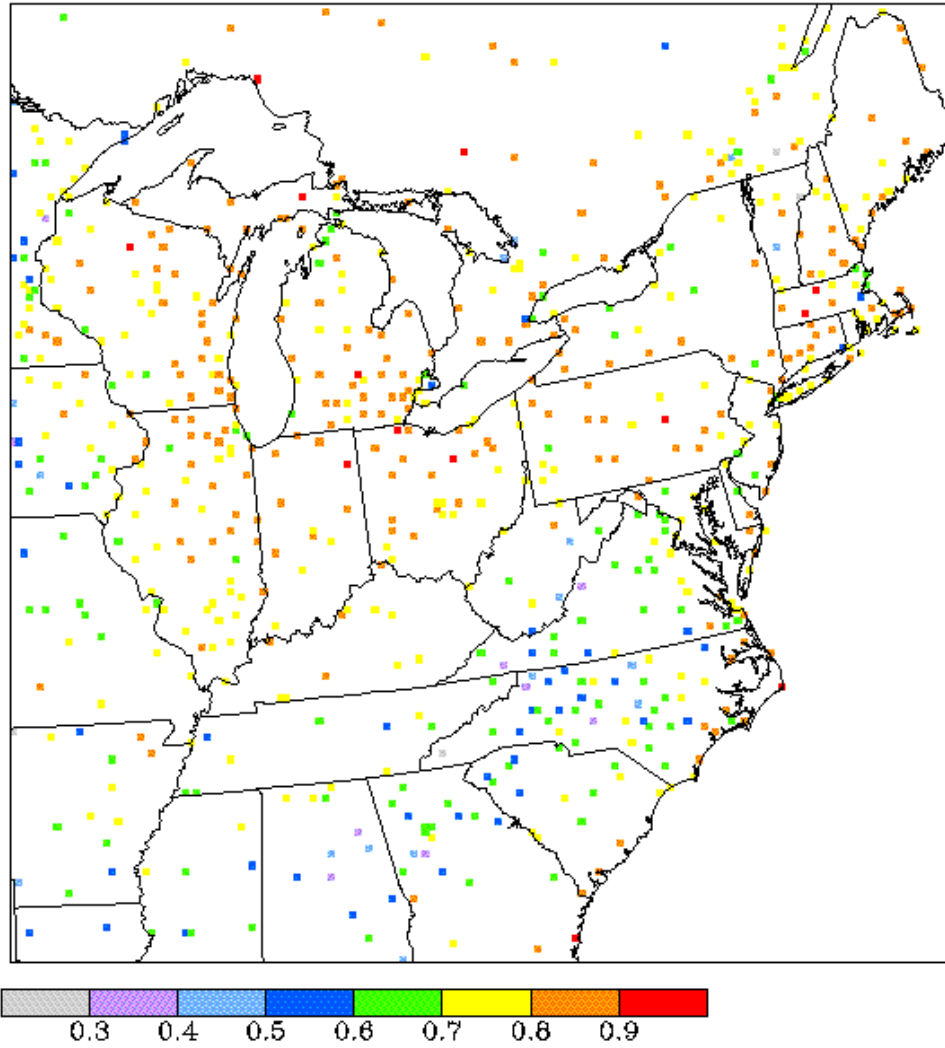
Figure 8a  Spatial Correlation – Temperature – BL  & TDL



UMD 2002 MM5 BL Temperature Correlation with TDL

0.93   0.94   0.95   0.96   0.97   0.98   0.99
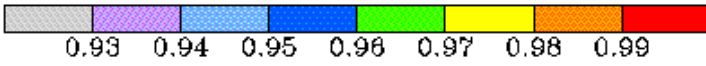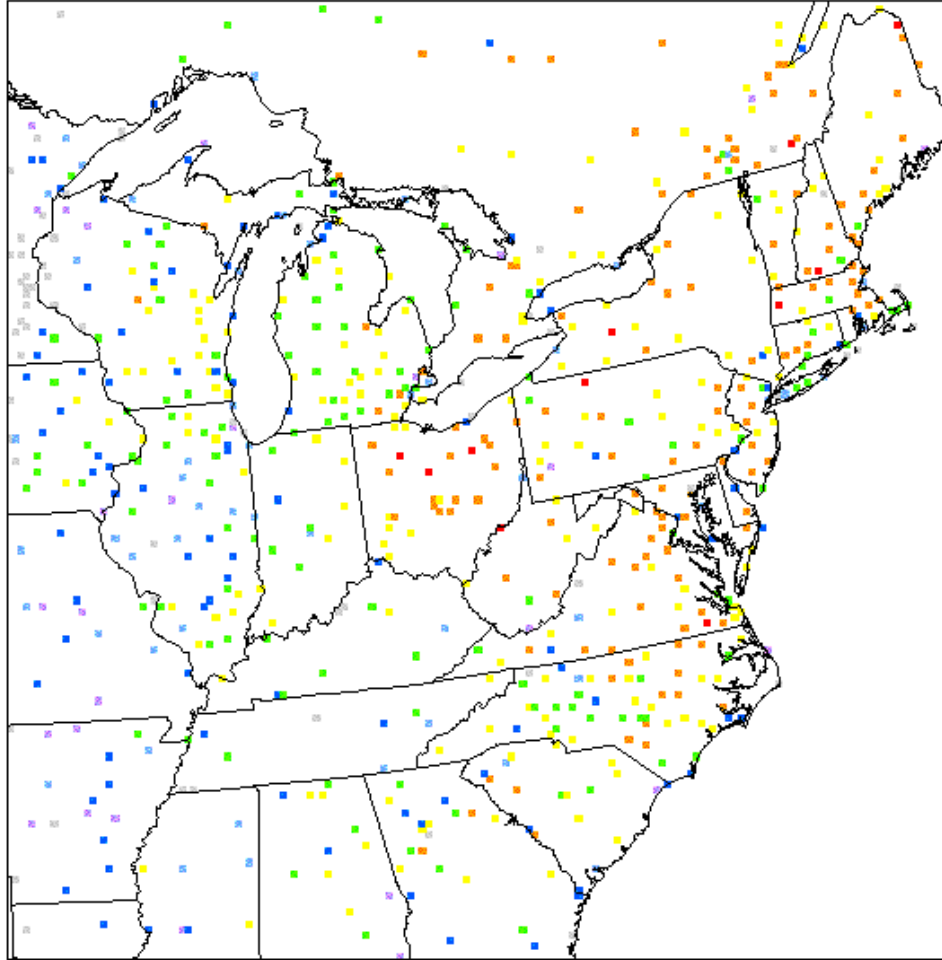
Figure 8b  Spatial Correlation – Temperature – PX & TDL



UMD 2002 MM5 PX Temperature Correlation with TDL
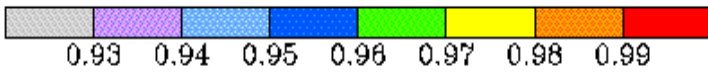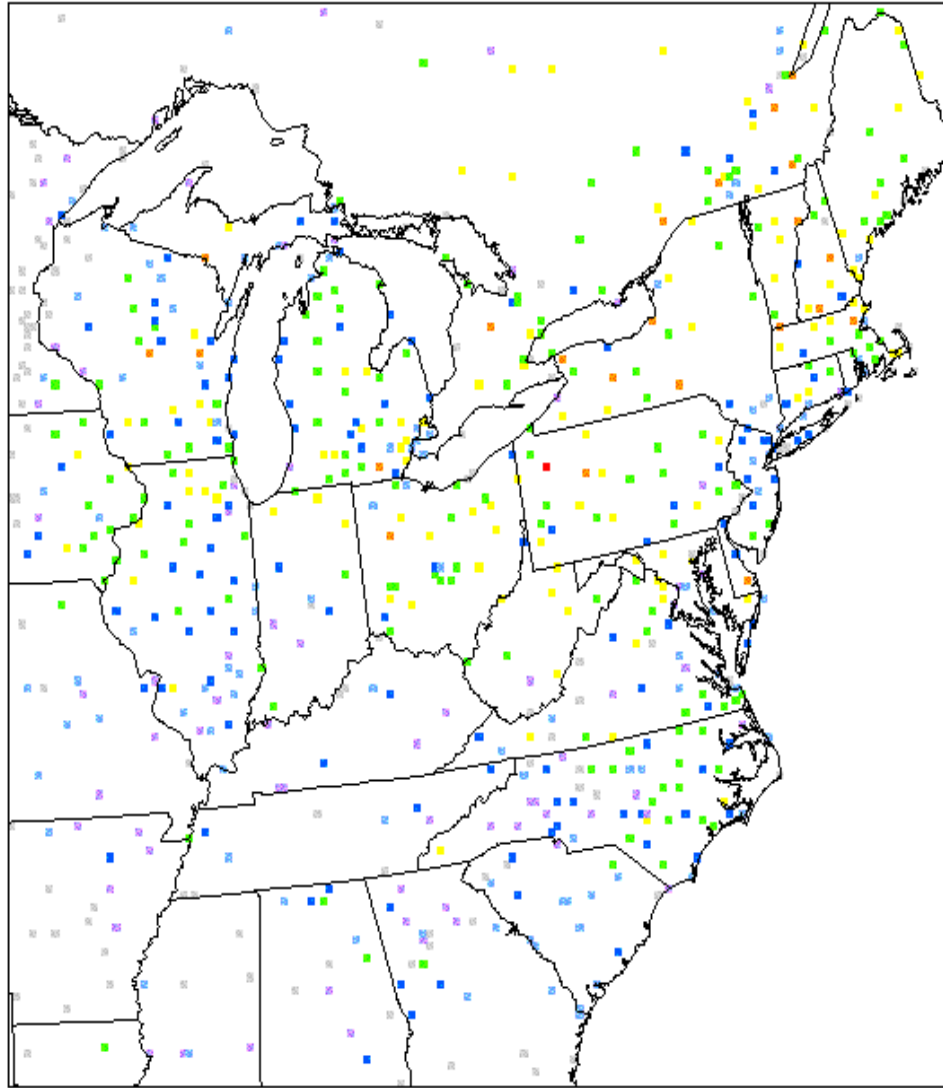
Figure 8c  Spatial Correlation – Temperature  SSIB & TDL

UMD 2002 MM5 SSiB Temperature Correlation with TDL

0.93  0.94  0.95  0.96  0.97  0.98  0.99

Figure 9a  Spatial Correlation  - Humidity  BL & TDL

UMD 2002 MM5 BL Humidity Correlation with TDL



0.65   0.70   0.75   0.80   0.85   0.90   0.95

Figure 9b Spatial Correlation – Humidity   PX & TDL



UMD 2002 MM5 PX Humidity Correlation with TDL

Figure 9c   Spatial Correlation – Humidity  SSIB  & TDL
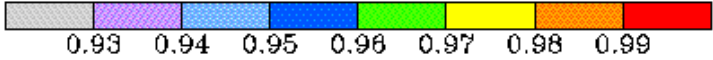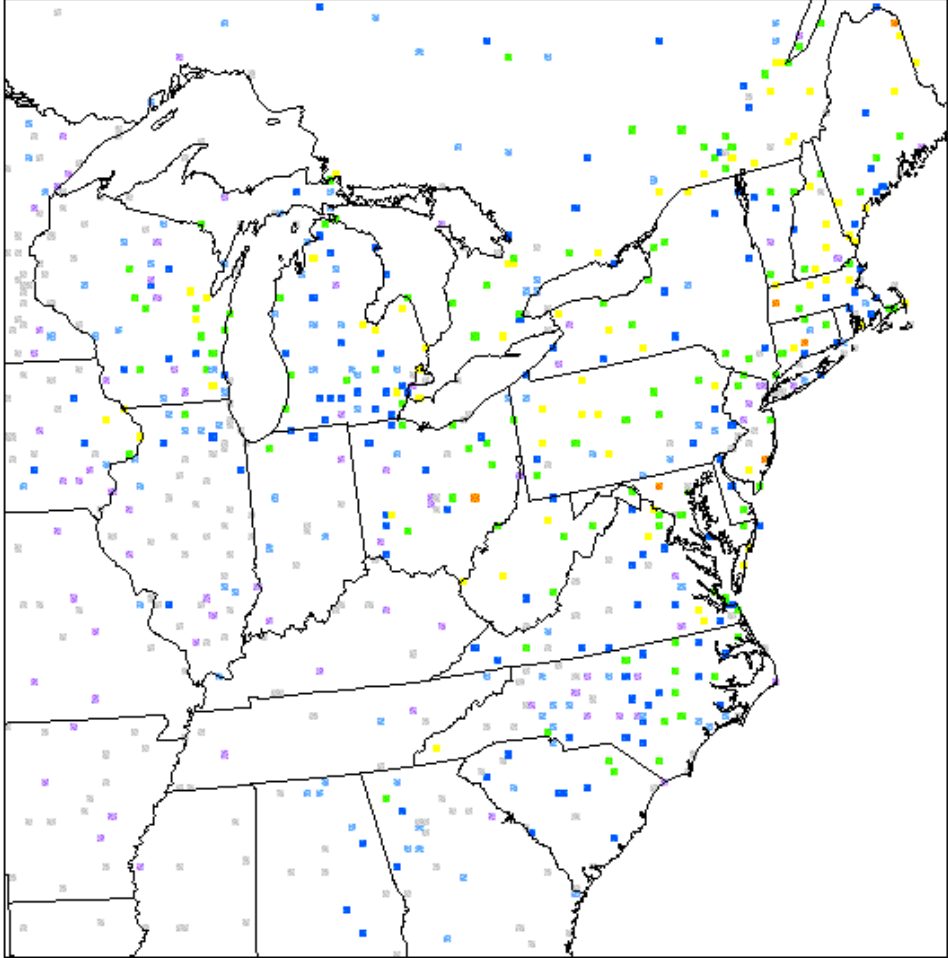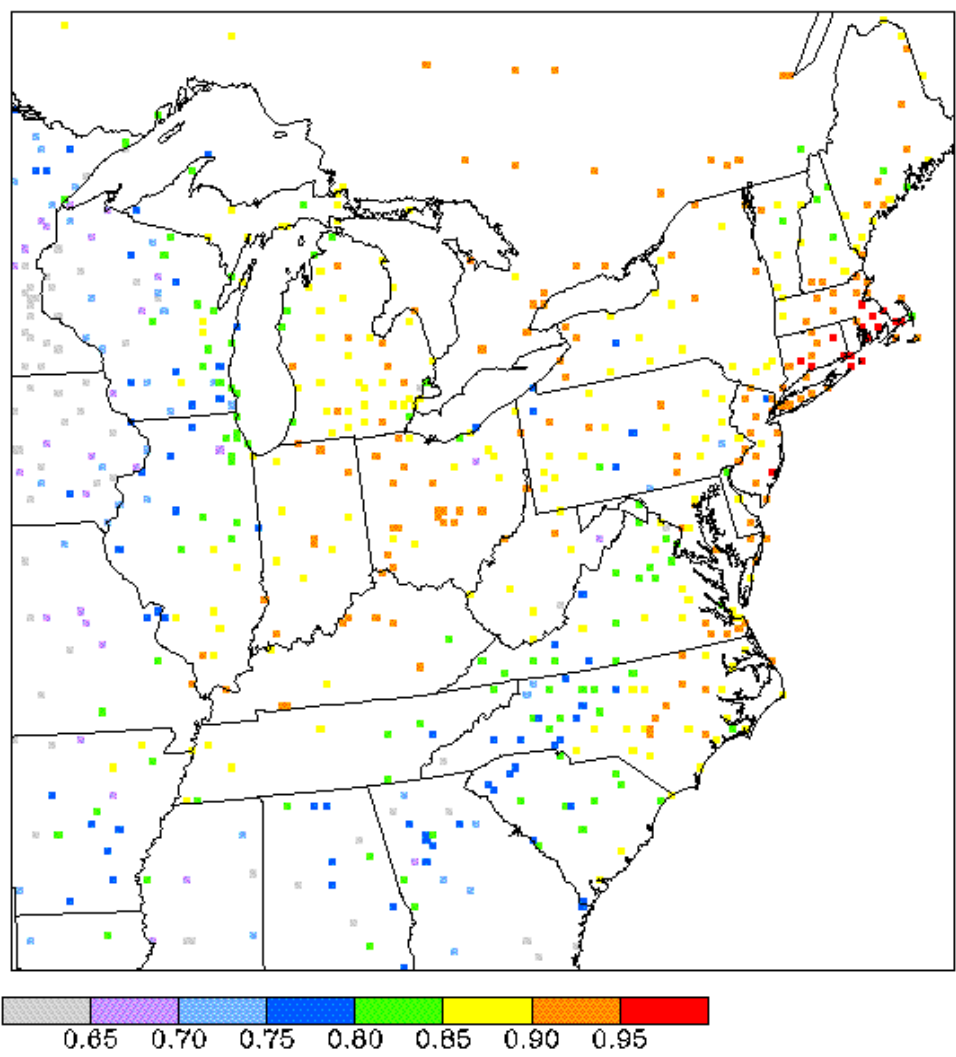
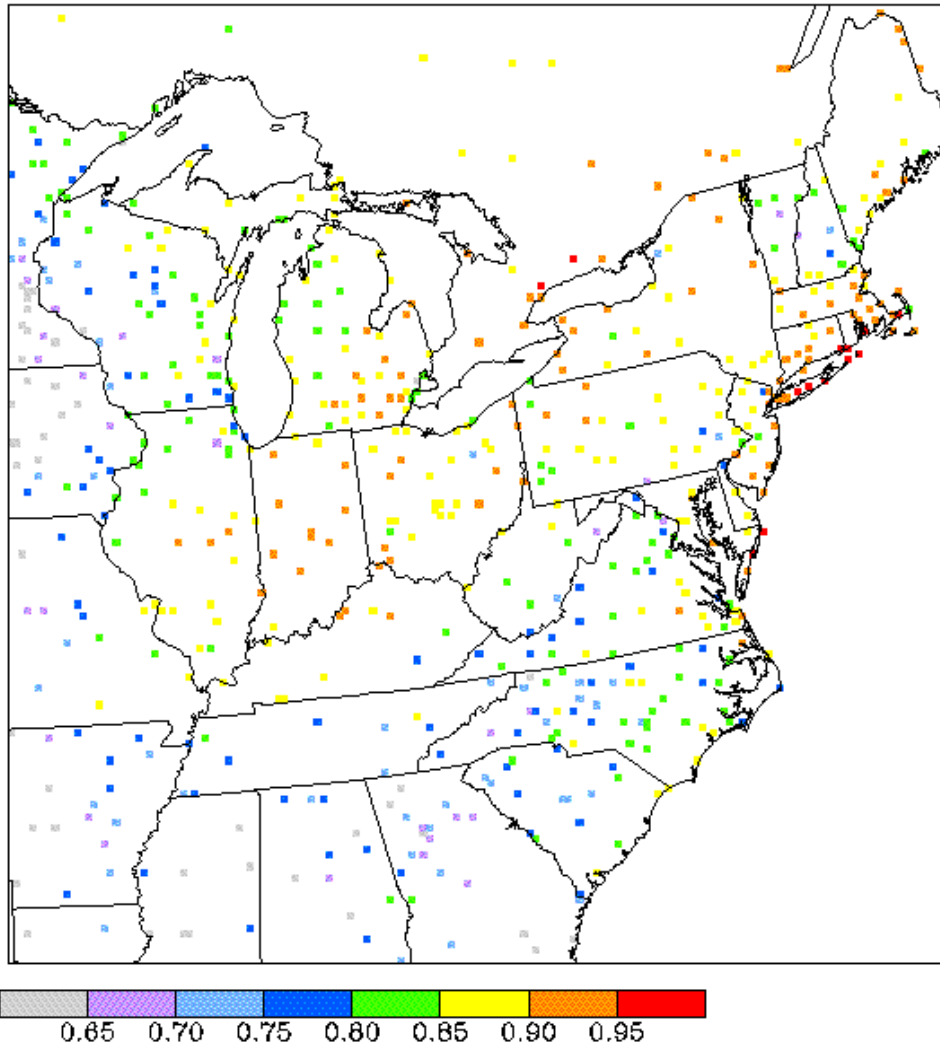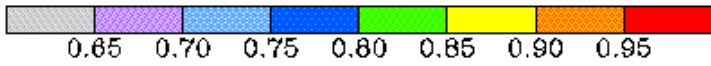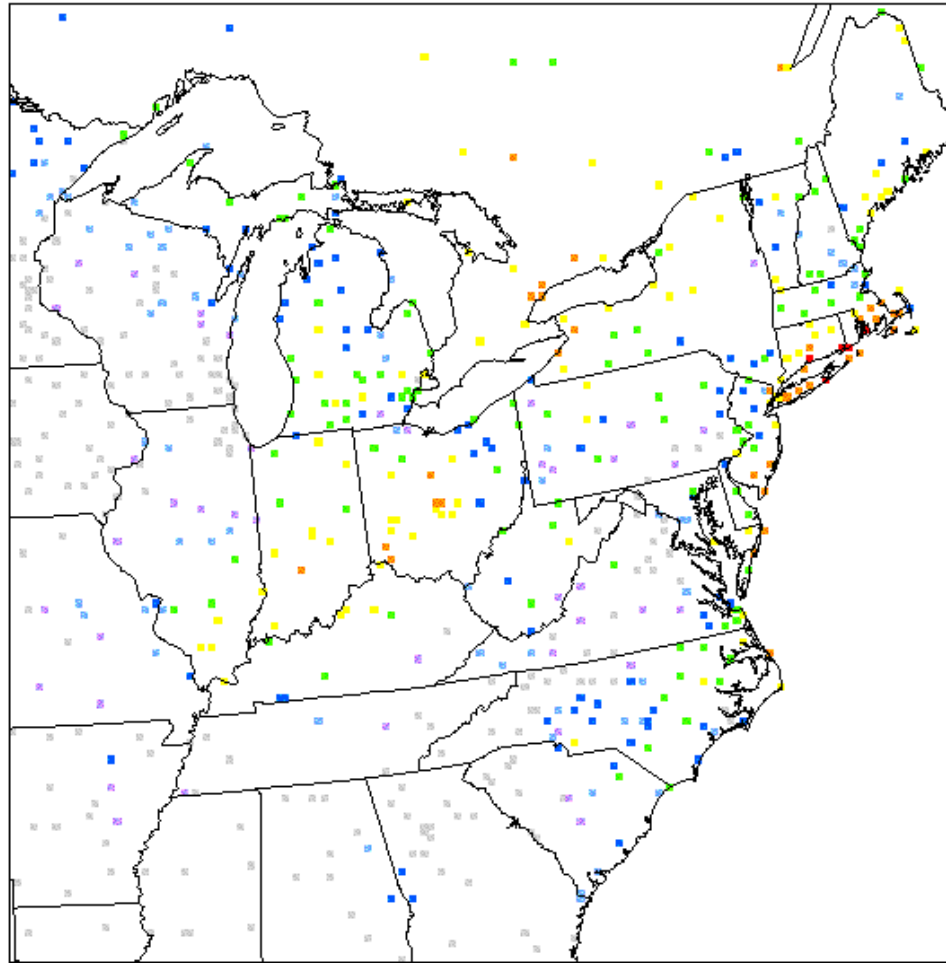UMD 2002 MM5 SSiB Humidity Correlation with TDL



0.65   0.70   0.75   0.80   0.85   0.90   0.95

# Numerical Experimental Analysis Data for the Year of 2002

Da-Lin Zhang and Shunli Zhang
Department of Atmospheric and Oceanic Science, University of Maryland
College Park, MD 20742
Tel. (301) 405-2018; Email: dalin@atmos.umd.edu

## 1. Introduction

A total of 128 numerical experiments, in 3-day segments, for the year of 2002 (i.e., from 0000 UTC 14 December 2001 to 0000 UTC 1 January 2003) have been conducted on our newly purchased Cluster using the nested-grid (36/12 km) Version 3.6 of the PSU/NCAR mesoscale model (i.e., MM5). The NCEP's Eta analysis with 40-km resolution was used to initialize the model integrations and specify the outmost lateral boundary conditions. To minimize the influence of model errors but retain as many mesoscale circulations as possible, the dynamical nudging or four-dimensional data assimilation (FDDA) technique was adopted to include observations of the surface winds and upper-level meteorological information. More attention was paid to the accuracy of surface winds due to their important roles in ozone transport. The model integrations were re-initialized every 3.5 days, allowing a 12-h period for the model spin-up (i.e., the first 12-h data could be truncated in the application of the datasets). Hourly model outputs were archived for the period of 12.5 months. This four-dimensional high resolution (in time and space) analysis dataset so assimilated was generated for air quality modeling and for regional haze studies. These integrations yielded a total of 830 Gbytes analysis data.

## 2. Model description

The Version 3.6 of MM5 with a Lambert conformal map projection, an MPP Version developed for clusters, was used for this project. The (x, y) dimensions of the coarse (36 km) and fine (12 km) mesh domains are 149 x 129 and 175 x 175, respectively. The vertical discretion uses terrain-following σ-coordinates, but the pressure at the σ-levels are determined from a reference state that is estimated using the hydrostatic equation from a given sea-level pressure and temperature with a standard lapse rate. There are 30 uneven σ levels, giving 29 layers, with higher resolution in the planetary boundary layer (PBL). The σ levels are placed at the following values:

1.000, 0.9974, 0.994, 0.989, 0.9820, 0.972, 0.959, 0.943, 0.923, 0.8990, 0.871, 0.839, 0.803, 0.763, 0.718, 0.668, 0.618, 0.568, 0.518, 0.468, 0.418, 0.368, 0.318, 0.268, 0.218, 0.168, 0.123, 0.080, 0.040, 0.00

The surface layer is defined at an altitude of about 10 m, the level at which surface winds are typically observed. The model top is set at 50 hPa with a radiative upper boundary condition. The time steps for the 36 km and 12 km resolution domains are 75 and 25 seconds, respectively.

Figs. 1 and 2 show the nested-grid (36/12 km) domain and the fine-mesh domain, respectively, that were used for this project.

Domain 1 is centered at $40^0$N latitude and $97^0$W longitude with a grid size of 36 km, and it covers the U.S. continents, Mexico, Canada, the Gulf of Mexico, and part of the East Pacific and West Atlantic oceans.

| Fig. 1 The coarse-mesh (36 km) domain. | Fig. 2  The fine-mesh (12-km) domain. |

Domain 2 uses a grid size of 12 km, and it covers the northeastern, central and southeastern US as well as Southeastern Canada.

The important model physics of the MM5 used for this project include:

(i) The latest version of the Kain-Fritsch (1993) convective scheme was used for both 36- and 12-km resolution domains;

(ii) An explicit moisture scheme (without the mixed phase) containing prognostic equations for cloud water (ice) and rainwater (snow) (Dudhia 1989; Zhang 1989);

(iii) A modified version of the Blackadar planetary boundary layer (PBL) scheme (Zhang and Anthes 1982; Zhang and Zheng 2004);

(iv) A simple radiative cooling scheme (Grell et al. 1997);

(v) A multi-layer soil model to predict land surface temperatures using the surface energy budget equation (Dudhia 1996).

Note that the Blackadar PBL scheme has been modified in order to reproduce the diurnal cycles of surface winds and temperatures, after performing a comparative study of the following five different PBL schemes: the Gayno-Seaman TKE scheme (Shafran et al. 2000), Burk-Thompson (1989), Blackadar (Zhang and Anthes 1982), MRF (Hong and Pan 1996), and Miller-Yamada-Jajić (Miller and Yamada 1974; Jajić 1990, 1994). These changes are given as follows (see Zhang and Zheng 2004 for more detail):

• K-coefficient is determined by the Richardson number according to Zhang and Anthes (1982), where the critical Richardson number is set to be 0.25. In addition, the mixing length is set to be the thickness of the model layer.

• Use of potential temperature rather than virtual potential temperature to calculate the bulk Richardson number Rb.

## 3. Nudging Processes

The MM5 provides options for nudging observations for each domain during the course of model integration (Stauffer and Seaman 1990; Stauffer et al. 1991). The Eta

analyses of upper-air winds, temperature and water-vapor mixing ratio as well as their associated surface fields, were nudged every 6 hours, and the higher-resolution surface wind field was nudged every 3 hours. While only the surface winds were nudged, their influences could be extended into the PBL (see Stauffer et al. 1991).

Based on our previous experience with many numerical experiments, the following nudging coefficients have been used:

- Upper-air wind fields: 5.0E-4 for Domain 1, and 2.5E-4 for Domain 2;
- Upper-air temperature fields: 1.0E-5 for both Domains;
- Surface winds: 5.0E-4 for Domain 1, and 2.5E-4 for Domain 2; and
- Surface temperature and moisture: not nudged due to instability consideration.

## 4. Model initialization

The model is initialized with NCEP's Eta model analysis (ds609.2) as a first guess that is then enhanced by observations at upper levels and the surface.

(i) NCEP's ADP global upper-air observations (NCAR archive ds353.4) are used to further enhance the upper-level Eta analysis.

(ii) The following two sets of surface observations have been introduced into the model initial state to improve the Eta analysis of surface wind fields:

- The NCEP's ADP global surface wind observations (NCAR archive ds464.0): This dataset provides 6-hourly surface observations over land (i.e., at 0000, 0600, 1200, 1800 UTC) in one stream, and 3-hourly (i.e., at 0300, 0900, 1500, 2100 UTC) over both land and ocean surfaces in another stream.
- The TDL's U.S. and Canadian surface observations (NCAR archive ds472.0): This dataset provides hourly surface observations over the U.S. and Canadian regions.

The Eta model analysis has a domain covering the entire U.S. continents with a 40-km horizontal resolution. It includes the following types of observations:

- Rawinsonde mass and wind;
- Piball winds;
- Dropwindsondes;
- Wind profiles;
- Surface land temperature and moisture;
- Oceanic surface data (ship and buoys);
- Aircraft winds;
- Satellite cloud-drift winds;
- Oceanic TOVS thickness retrievals;
- GOES and SSM/I precipitable water retrievals.

The Cressman objective analysis option was used to enhance the Eta analysis. However, we analyzed the results and found that it still could not reproduce the right diurnal cycle of surface winds and temperatures. Thus, we repeated the Cressman procedures three more times to enhance the surface analyses. Results indicate that this procedure significantly improved the results.

Note that (i) because of the initial model spin-up, we recommend that the first 12-h model integration of each run be discarded; and (ii) because the synoptic-scale upper-air winds and temperatures were nudged, the flow fields above the PBL might contain less smaller-scale features (e.g., in low-level jets, mountain-forced perturbations and etc.).

## 5. Data Archive

As mentioned above, we have conducted a total of 128 experiments, in 3-day segments, from 0000 UTC 14 December 2001 to 0000 UTC 1 January 2003. The following table lists the experiments and their corresponding integration periods:

| Exp. # | Period | Exp. # | Period |
|---|---|---|---|
| 1 | 00/15/12-00/18/12*01 | 2 | 00/18/12-12/21/12*01 |
| 3 | 00/21/12-00/24/12*01 | 4 | 00/24/12-00/27/12*01 |
| 5 | 00/27/12-00/30/12*01 | 6 | 00/30/12-00/02/01*02 |
| 7 | 00/02/01-00/05/01*02 | 8 | 00/05/01-00/08/01*02 |
| 9 | 00/08/01-00/11/01*02 | 10 | 00/11/01-00/14/01*02 |
| 11 | 00/14/01-00/17/01*02 | 12 | 00/17/01-00/20/01*02 |
| 13 | 00/20/01-00/23/01*02 | 14 | 00/23/01-00/26/01*02 |
| 15 | 00/26/01-00/29/01*02 | 16 | 00/29/01-00/01/02*02 |
| 17 | 00/01/02-00/04/02*02 | 18 | 00/04/02-00/07/02*02 |
| Exp. # | Period | Exp. # | Period |
| 19 | 00/07/02-00/10/02*02 | 20 | 00/10/02-00/13/02*02 |
| 21 | 00/13/02-00/16/02*02 | 22 | 00/16/02-00/19/02*02 |
| 23 | 00/19/02-00/22/02*02 | 24 | 00/22/02-00/25/02*02 |
| 25 | 00/25/02-00/28/02*02 | 26 | 00/28/02-00/03/03*02 |
| 27 | 00/03/03-00/06/03*02 | 28 | 00/06/03-00/09/03*02 |
| 29 | 00/09/03-00/12/03*02 | 30 | 00/12/03-00/15/03*02 |
| 31 | 00/15/03-00/18/03*02 | 32 | 00/18/03-00/21/03*02 |
| 33 | 00/21/03-00/24/03*02 | 34 | 00/24/03-00/27/03*02 |
| 35 | 00/27/03-00/30/03*02 | 36 | 00/30/03-00/02/04*02 |
| 37 | 00/02/04-00/05/04*02 | 38 | 00/05/04-00/08/04*02 |
| 39 | 00/08/04-00/11/04*02 | 40 | 00/11/04-00/14/04*02 |
| 41 | 00/14/04-00/17/04*02 | 42 | 00/17/04-00/20/04*02 |
| 43 | 00/20/04-00/23/04*02 | 44 | 00/23/04-00/26/04*02 |
| 45 | 00/26/04-00/29/04*02 | 46 | 00/29/04-00/02/05*02 |
| 47 | 00/01/05-00/04/05*02 | 48 | 00/04/05-00/07/05*02 |
| 49 | 00/07/05-00/10/05*02 | 50 | 00/10/05-00/13/05*02 |
| 51 | 00/13/05-00/16/05*02 | 52 | 00/16/05-00/19/05*02 |
| 53 | 00/19/05-00/22/05*02 | 54 | 00/22/05-00/25/05*02 |
| 55 | 00/25/05-00/28/05*02 | 56 | 00/28/05-00/31/05*02 |
| 57 | 00/31/05-00/03/06*02 | 58 | 00/03/06-00/06/06*02 |
| 59 | 00/06/06-00/09/06*02 | 60 | 00/09/06-00/12/06*02 |
| 61 | 00/12/06-00/15/06*02 | 62 | 00/15/06-00/18/06*02 |
| 63 | 00/18/06-00/21/06*02 | 64 | 00/21/06-00/24/06*02 |
| 65 | 00/24/06-00/27/06*02 | 66 | 00/27/06-00/30/06*02 |

| 67 | 00/30/06-00/03/07*02 | 68 | 00/03/07-00/06/07*02 |
|---|---|---|---|
| 69 | 00/06/07-00/09/07*02 | 70 | 00/09/07-00/12/07*02 |
| 71 | 00/12/07-00/15/07*02 | 72 | 00/15/07-00/18/07*02 |
| 73 | 00/18/07-00/21/07*02 | 74 | 00/21/07-00/24/07*02 |
| 75 | 00/24/07-00/27/07*02 | 76 | 00/27/07-00/30/07*02 |
| 77 | 00/30/07-00/02/08*02 | 78 | 00/02/08-00/05/08*02 |
| 79 | 00/05/08-00/08/08*02 | 80 | 00/08/08-00/11/08*02 |
| 81 | 00/11/08-00/14/08*02 | 82 | 00/14/08-00/17/08*02 |
| 83 | 00/17/08-00/20/08*02 | 84 | 00/20/08-00/23/08*02 |
| 85 | 00/23/08-00/26/08*02 | 86 | 00/26/08-00/29/08*02 |
| 87 | 00/29/08-00/01/09*02 | 88 | 00/01/08-00/04/09*02 |
| 89 | 00/04/09-00/07/09*02 | 90 | 00/07/09-00/10/09*02 |
| 91 | 00/10/09-00/13/09*02 | 92 | 00/13/09-00/16/09*02 |
| 93 | 00/16/09-00/19/09*02 | 94 | 00/19/09-00/22/09*02 |
| 95 | 00/22/09-00/25/09*02 | 96 | 00/25/09-00/28/09*02 |
| 97 | 00/28/09-00/01/10*02 | 98 | 00/01/10-00/04/10*02 |
| 99 | 00/04/10-00/07/10*02 | 100 | 00/07/10-00/10/10*02 |
| 101 | 00/10/10-00/13/10*02 | 102 | 00/13/10-00/16/10*02 |
| 103 | 00/16/10-00/19/10*02 | 104 | 00/19/10-00/22/10*02 |

| Exp. # | Period | Exp. # | Period |
|---|---|---|---|
| 105 | 00/22/10-00/25/10*02 | 106 | 00/25/10-00/28/10*02 |
| 107 | 00/28/10-00/31/10*02 | 108 | 00/31/10-00/03/11*02 |
| 109 | 00/03/11-00/06/11*02 | 110 | 00/06/11-00/09/11*02 |
| 111 | 00/09/11-00/12/11*02 | 112 | 00/12/11-00/15/11*02 |
| 113 | 00/15/11-00/18/11*02 | 114 | 00/18/11-00/21/11*02 |
| 115 | 00/21/11-00/24/11*02 | 116 | 00/24/11-00/27/11*02 |
| 117 | 00/27/11-00/30/11*02 | 118 | 00/30/11-00/03/12*02 |
| 119 | 00/03/12-00/06/12*02 | 120 | 00/06/12-00/09/12*02 |
| 121 | 00/09/12-00/12/12*02 | 122 | 00/12/12-00/15/12*02 |
| 123 | 00/15/12-00/18/12*02 | 124 | 00/18/12-00/21/12*02 |
| 125 | 00/21/12-00/24/12*02 | 126 | 00/24/12-00/27/12*02 |
| 127 | 00/27/12-00/30/12*02 | 128 | 00/30/12-00/02/01*03 |

The datasets listed above include the MM5 outputs from Domain 1 (36 km) and Domain 2 (12 km), the analysis data used for FDDA, and initial and lateral boundary conditions. If necessary, any of the experiments listed above could be re-run. The MM5 outputs include the three-dimensional fields of temperature, horizontal winds, vertical motion, pressure perturbations, moisture, cloud water/rain water/ice water/snow water mixing ratio, and radiation tendency; and the two-dimensional fields of the map-scale factor, longitude and latitude, Coriolis parameter, land use category, terrain height, PBL depth, accumulated convective/non-convective precipitation, surface sensible/latent heat flux. A FORTRAN program to read the datasets has also been included.

**6. Acknowledgments**

**References**

Burk, S. D., and W. T. Thompson, 1989: A vertically nested regional numerical weather prediction model with second-order closure physics. *Mon. Wea. Rev.,* **117,** 2305–2324.

Dudhia, J., 1989: Numerical study of convection observed during the winter monsoon experiments using a mesoscale two-dimensional model. *J. Atmos. Sci.,* **46,** 3077–3107.

Grell, G. A., J. Dudhia, and D. R. Stauffer, 1995: A description of the fifth-generation Penn State/NCAR Mesoscale Model (MM5). NCAR Tech. Note NCAR/TN-398 1 STR, 122 pp.

Hong, S.-H., and H.-L. Pan, 1996: Nonlocal boundary layer vertical diffusion in a medium-range forecast model. *Mon. Wea. Rev.,* **124,** 2322–2339.

Jajić, Z. I., 1990: The step-mountain coordinate: Physical package. *Mon. Wea. Rev.,* **118,** 1429-1443.

——, 1994: The step-mountain Eta coordinate model: Further development of the convection, viscous sublayer and turbulent closure schemes. *Mon. Wea. Rev.,* **122,** 927-945.

Kain, J.S., and J.M. Fritsch, 1993: Convective parameterization for mesoscale models: The Kain-Fritsch scheme. Cumulus Parameterization. *Meteor. Monogr.*, **46**, Amer. Meteor. Soc., 165-170.

Mellor, G. L., and T. Yamada, 1974: A hierarchy of turbulence closure models for planetary boundary layers. *J. Atmos. Sci.,* **31,** 1791–1806.

Shafran, P.C., N.L. Seaman, and G.A. Gayno, 2000: Evaluation of numerical predictions of boundary layer structure during the Lake Michigan ozone study. *J. Appl. Meteor.,* **39,** 412-426.

Stauffer, D. R., N. L. Seaman and F. S. Binkowski, 1991: Use of four-dimensional data assimilation in a limited-area mesoscale model. Part II: Effects of data assimilation within the planetary boundary layer. *Mon. Wea. Rev.*, **119**, 734-754.

Stauffer, D. R. and N. L. Seaman, 1990: Use of four-dimensional data assimilation in a limited-area mesoscale model. Part I: Experiments with synoptic-scale data. *Mon. Wea. Rev.*, **118**, 1250-1277.

Zhang, D.-L., 1989: The effect of parameterized ice microphysics on the simulation of vortex circulation with a mesoscale hydrostatic model. *Tellus*, **41A**, 132-147.

——, and R. A. Anthes, 1982: A high-resolution model of the planetary boundary layer—Sensitivity tests and comparisons with SESAME-79 data. *J. Appl. Meteor.,* **21,** 1594–1609.

——, and W.-Z. Zheng, 2004: Diurnal cycles of surface winds and temperatures as simulated by five boundary-layer parameterizations. *J. Appl. Meteor.,* **43**, 157-169.

# Meteorological Data Analysis

Urban, Regional Modeling and Analysis Section
Division of Air Resources
New York State Department of Environmental Conservation
November 16, 2005

# OTC Air Quality Modeling Domains



36km Domain (145x102x22)

12km Domain (172x172x22)

MM5 input and output files were received from UMD for entire 2002 in 128 3.5-day chunks with 12-hour overlapping period between adjacent pieces

Evaluation was limited to 12km air quality modeling domain for 12km MM5 output files over the 5-month period of may to September 2002

Surface observation datasets include NCAR ds472.0 (around 800 stations) and CASTNet data (around 50 stations)

METSTAT program from Environ was used to examine surface wind speed and direction, temperature and humidity

Correlation coefficients were calculated for surface wind speed, temperature and humidity

Wind speed correlation with TDL are ranging from 0.7 to 0.8

Temperature correlation with TDL are .96 and better

Humidity correlation with TDL are ranging from 0.8 to 0.9

MM5 Sfc Wind Speed Correlation with TDL   May to Sept 2002

0.5   0.6   0.7   0.8   0.9

MM5 Sfc Temperature Correlation with TDL   May to Sept 2002

0.90   0.92   0.94   0.96   0.98
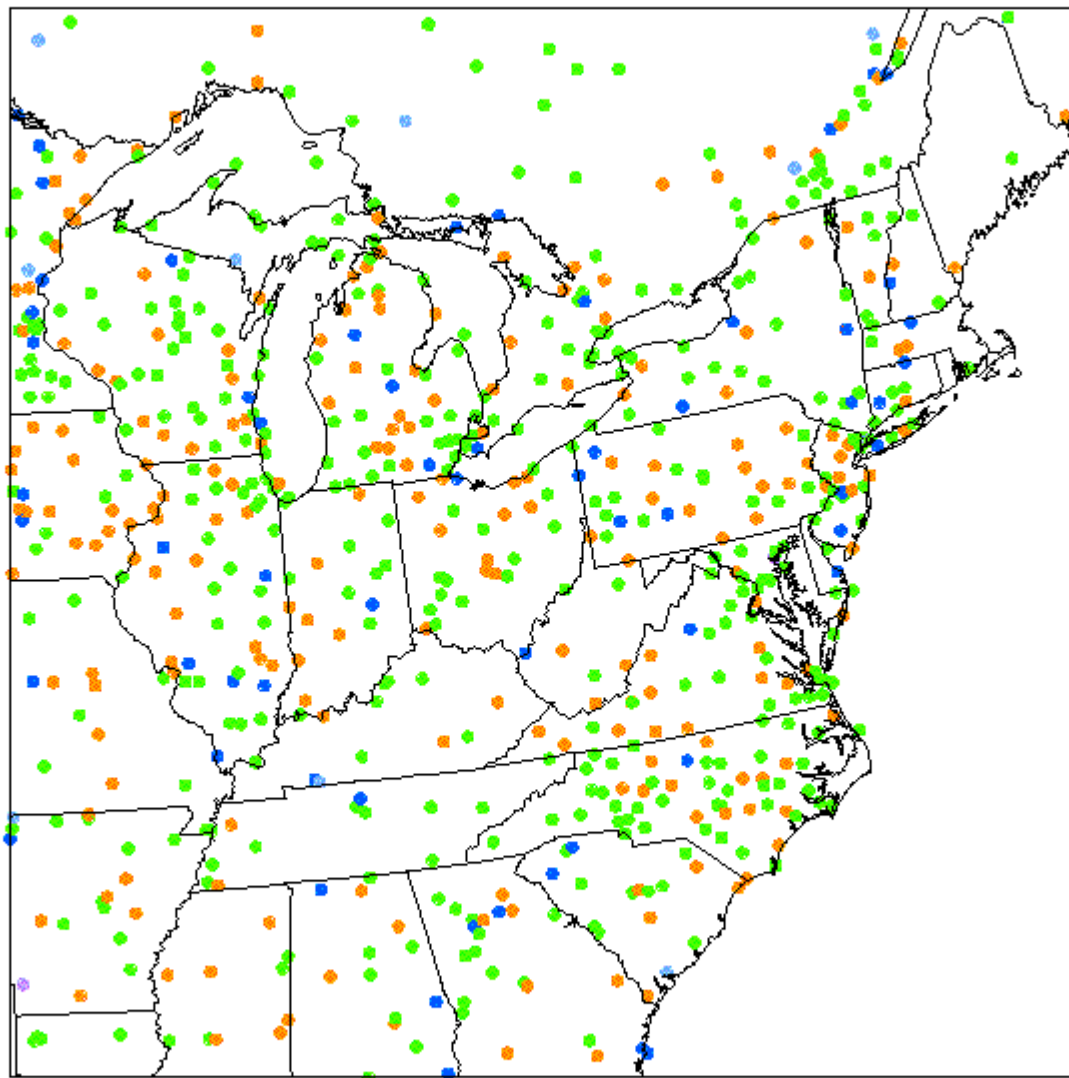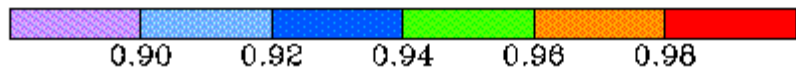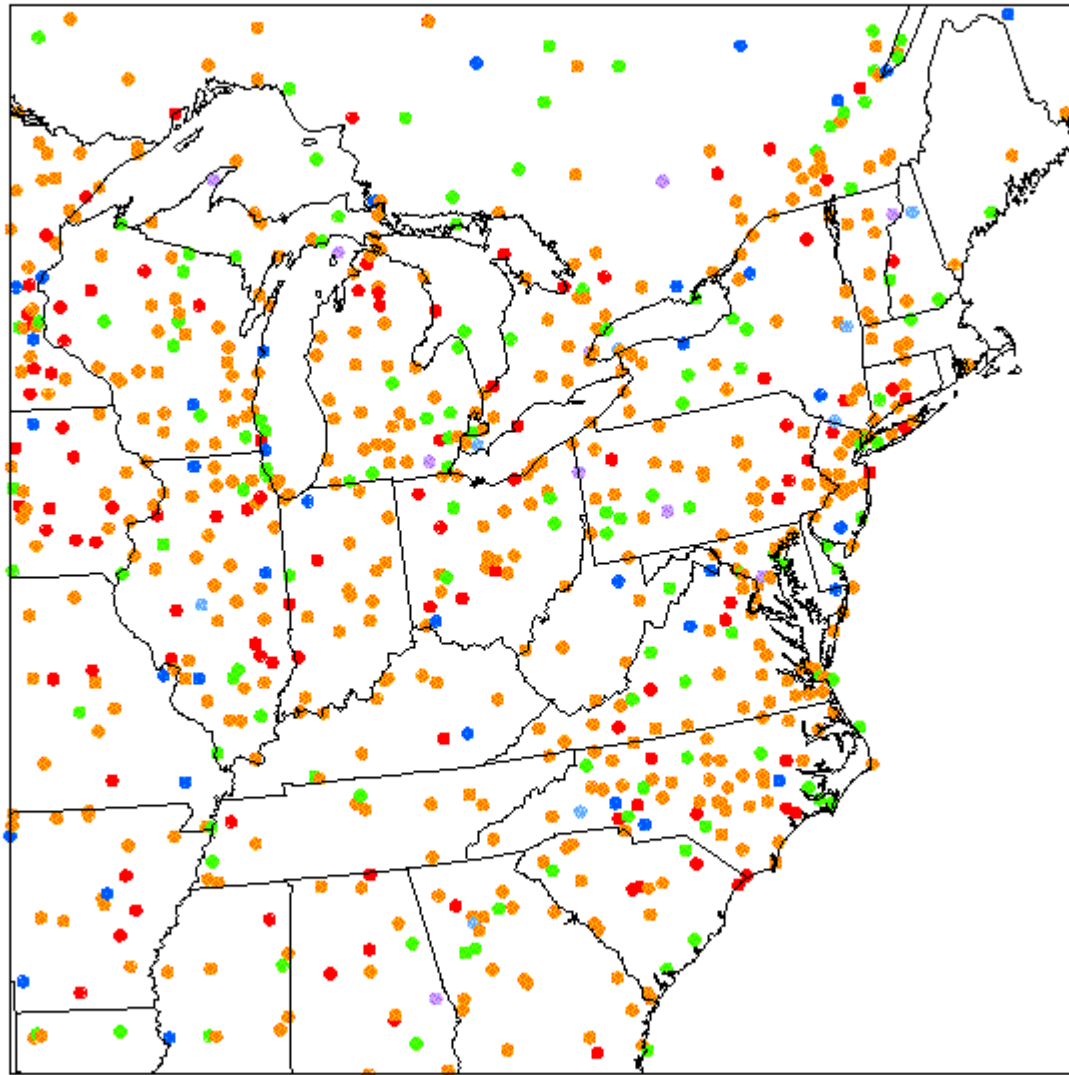
MM5 Sfc Humidity Correlation with TDL   May to Sept 2002
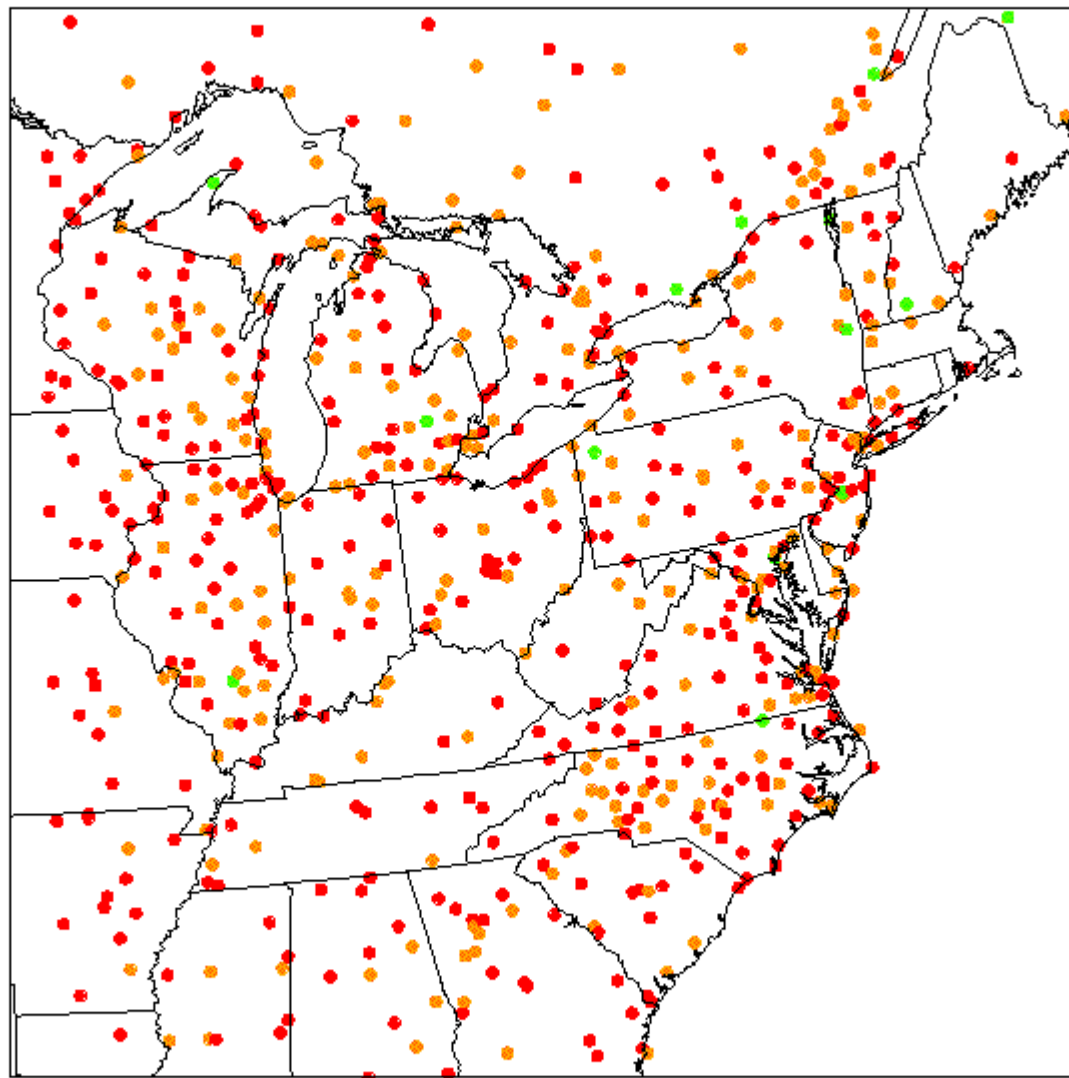
# Monthly total of MM5 predicted precipitation was compared with 1/8-degree CPC rain gauge analysis

For months of May and September 2002, MM5 is doing a fair job capturing the rainfall patterns

For months of June, July and August, the model is not doing well in terms of pattern and amount, probably is related to summertime convective activities

# Obs       May 2002       MM5



Monthly Precip Accummulation May 2002 CPC RFC 1/8 Deg

UMD MM5 Monthly Precip Accummulation May 2002

Max= 16 Inches

Max= 16 Inches

Obs                     June 2002                     MM5

Monthly Precip Accummulation June 2002 CPC RFC 1/8 Deg

UMD MM5 Monthly Precip Accummulation June 2002

Max= 15 Inches

Max= 23 Inches

# Obs        July 2002        MM5



Monthly Precip Accummulation July 2002 CPC RFC 1/8 Deg
Max= 9 Inches
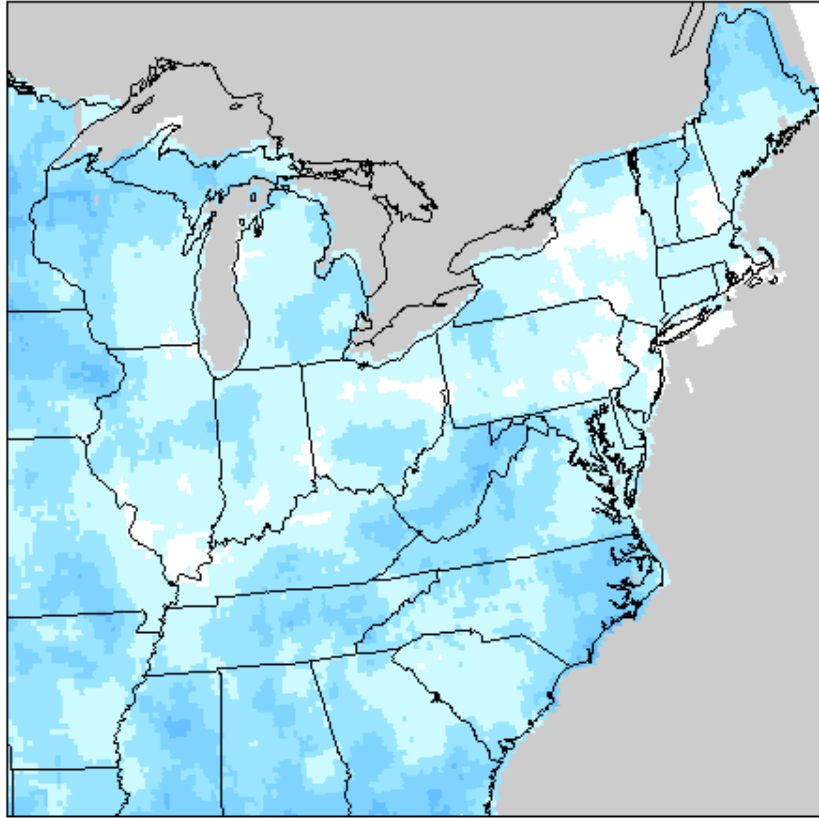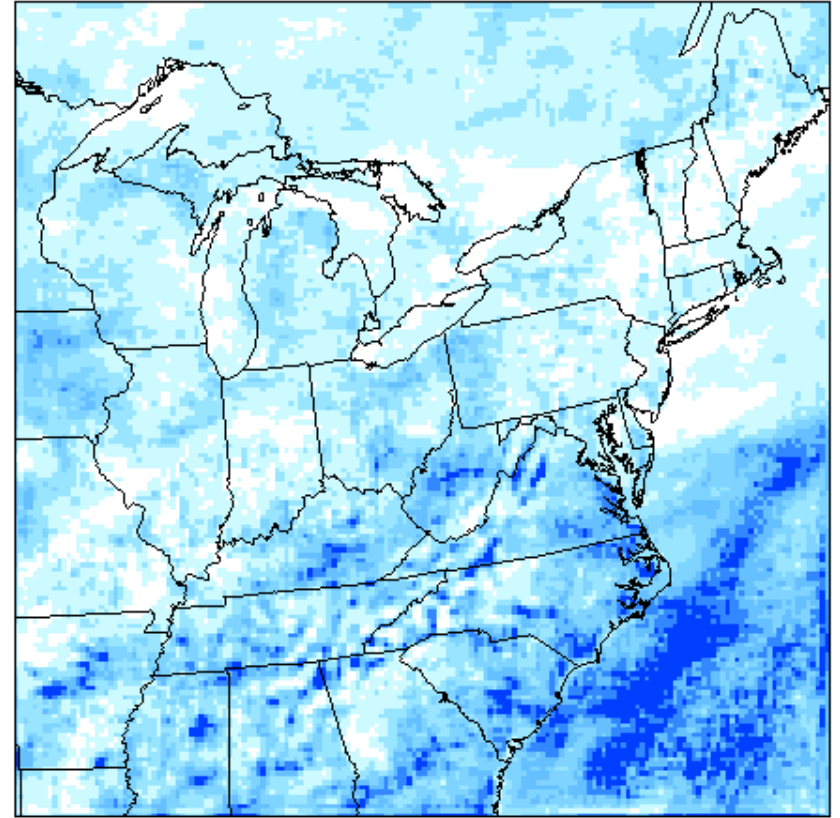
UMD MM5 Monthly Precip Accummulation  July 2002
Max= 21 Inches

Obs          August 2002          MM5

Monthly Precip Accummulation August 2002 CPC RFC 1/8 Deg

UMD MM5 Monthly Precip Accummulation  August 2002

Max= 11 Inches
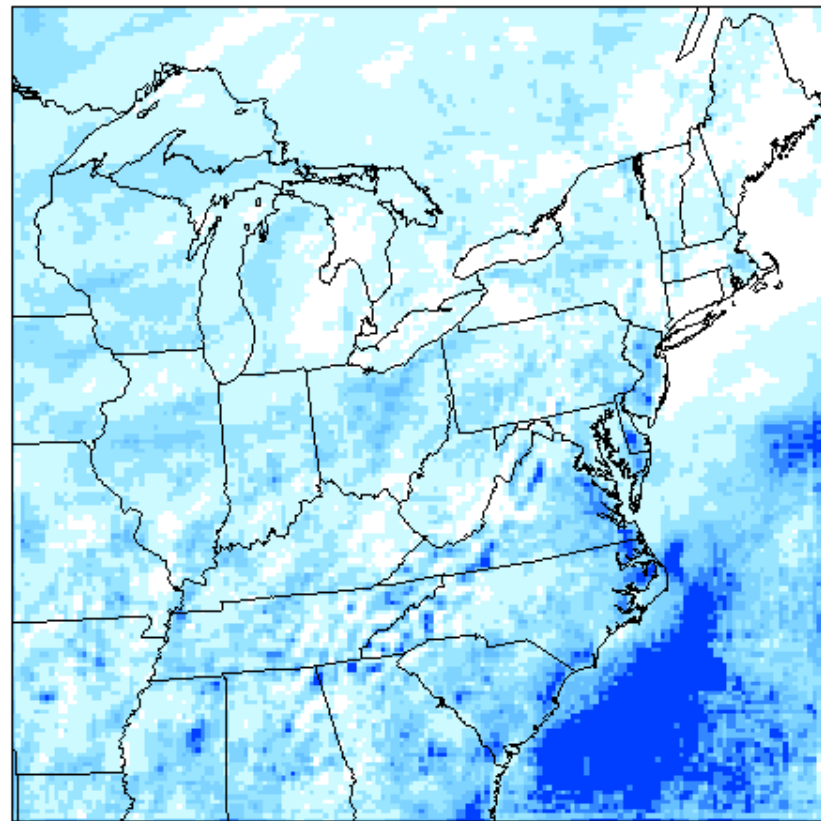
Max= 26 Inches

# Obs            September 2002            MM5



Monthly Precip Accummulation September 2002 CPC RFC 1/8 Deg



UMD MM5 Monthly Precip Accummulation  September 2002

Max= 13 Inches
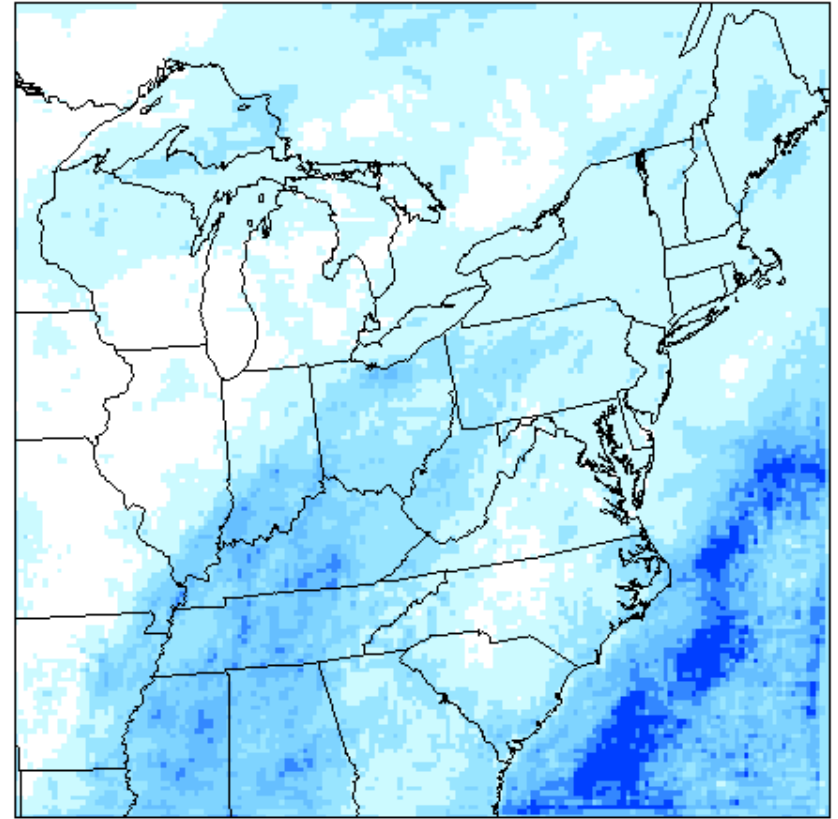
Max= 17 Inches

# MM5 cloud cover was compared qualitatively with UMD Surface Radiation Budget Groups' products

The observed cloud interpolated from satellite base data of $0.5^o$ by $0.5^o$ resolution

Total cloud fraction estimated by MCIP from MM5 low, middle and high cloud fraction

MM5 is doing a fair job to simulate cloud patterns for the time periods we examined

# Observed and Simulated Cloud field on August 13, 2002

## Observed Cloud



August 13,2002 12:00:00
Min=   0.00 at (152,1), Max=   1.00 at (1,1)

## MM5 Cloud



FRACTION

August 13,2002 12:00:00
Min=   0.00 at (160,1), Max=   1.00 at (148,17)
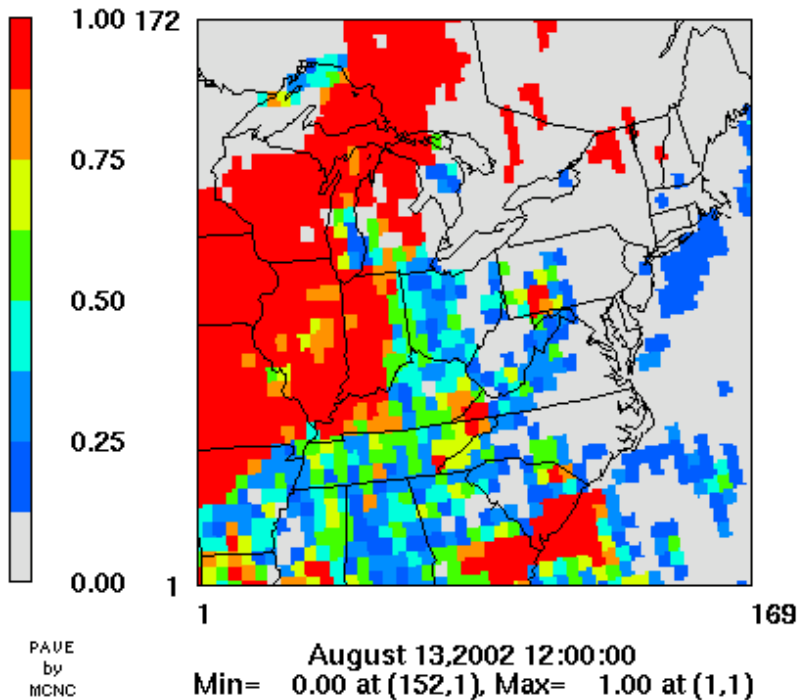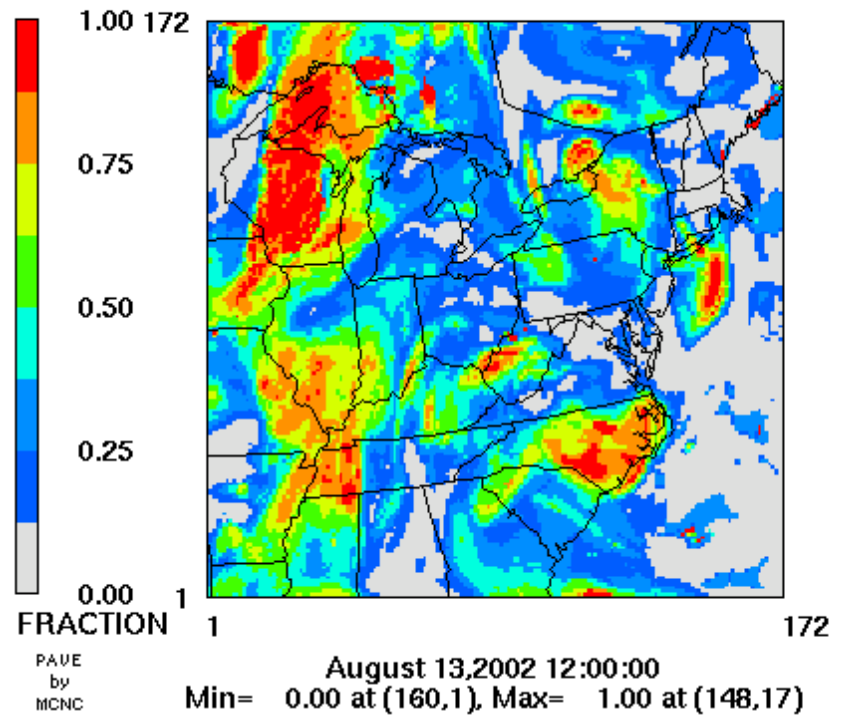
# Observed and Simulated Cloud Field on August 14, 2002

# Observed and Simulated Cloud Field on August 15, 2002
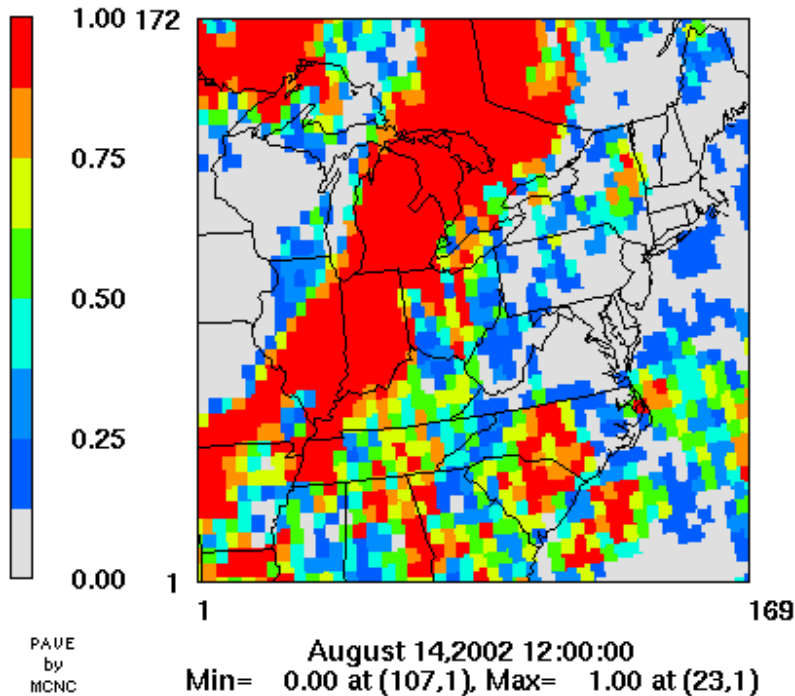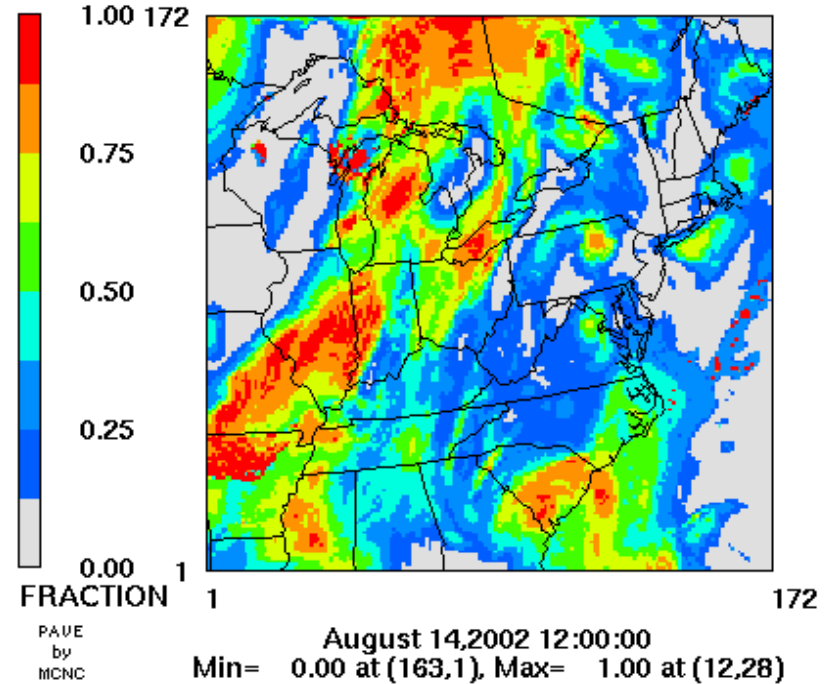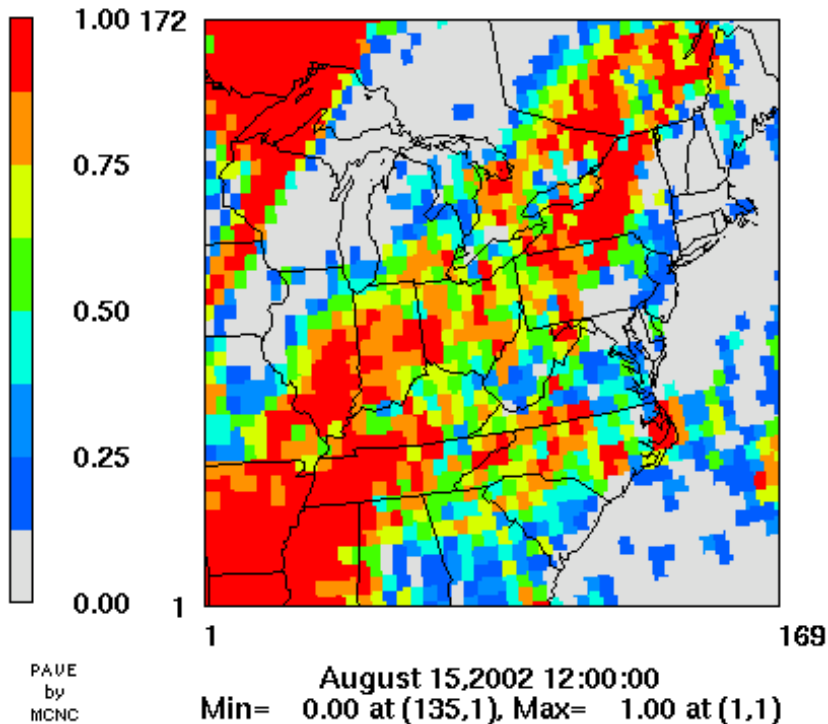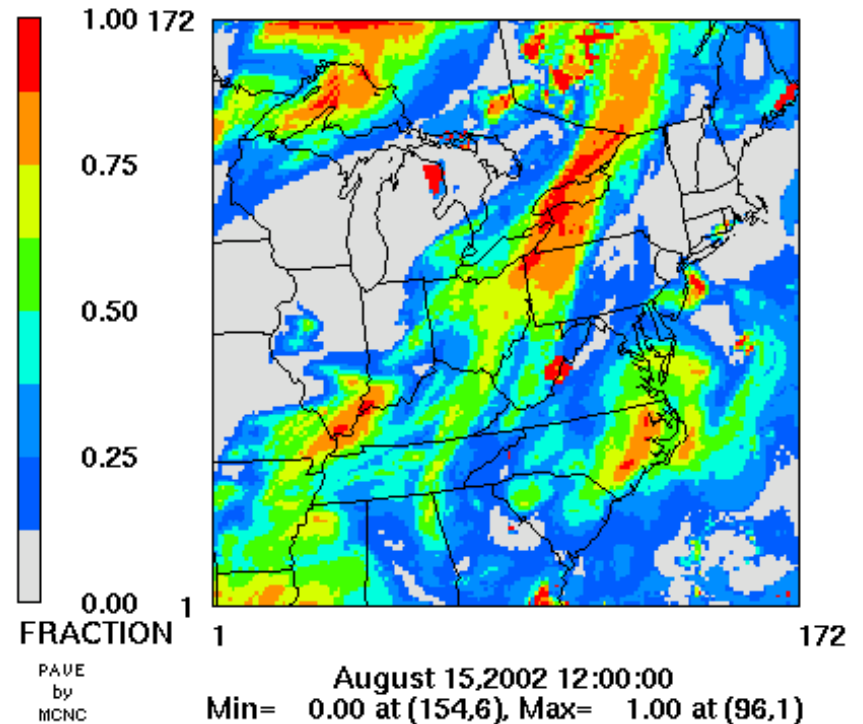
MM5 vertical wind speed profiles were compared qualitatively with wind profilers observations, using low level jets (LLJ) as an indicator

MM5 is doing a fair job capturing LLJ events

# RICHMOND VA  Lat:37.6 Lon:-77.5 Elev:61m
WindSpeedDirection| Mode:60m,105m | Res:30min |  QC:good only
VIRGINIA DEPARTMENT OF ENVIRONMENTAL QUALITY



Richmond, VA

CONCORD NH  Lat:43.21 Lon:−71.52 Elev:104m
WindSpeedDirection| Mode:60m,105m | Res:60min |  QC:good only
NOAA ENVIRONMENTAL TECHNOLOGY LABORATORY

Concord, NH

August 15, 2002
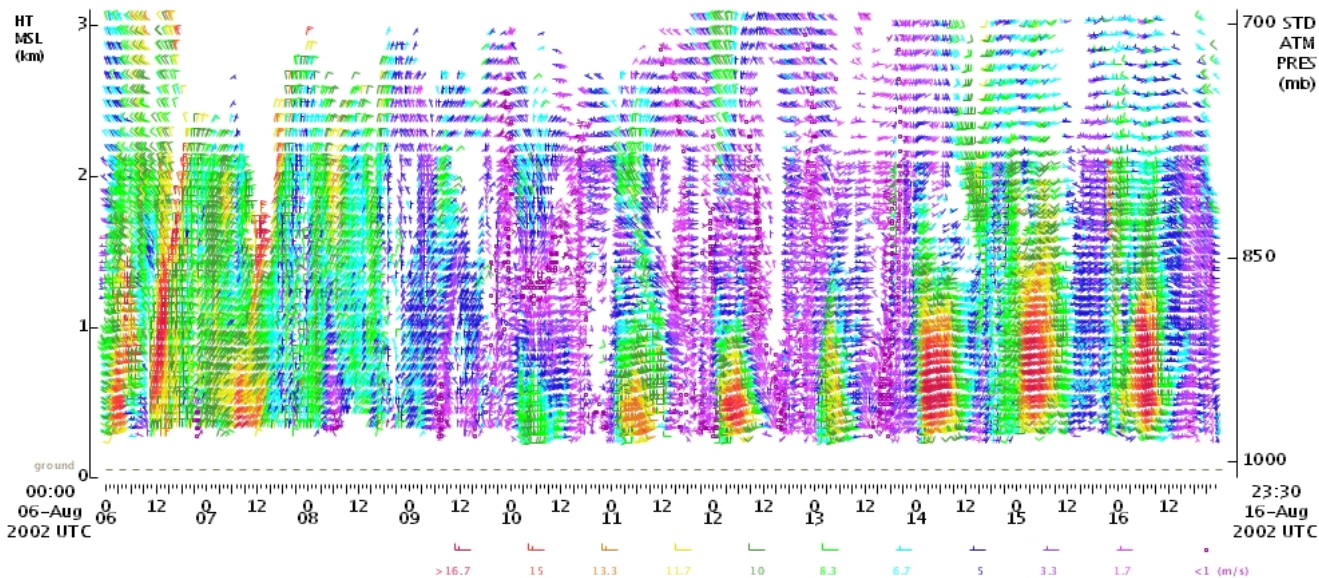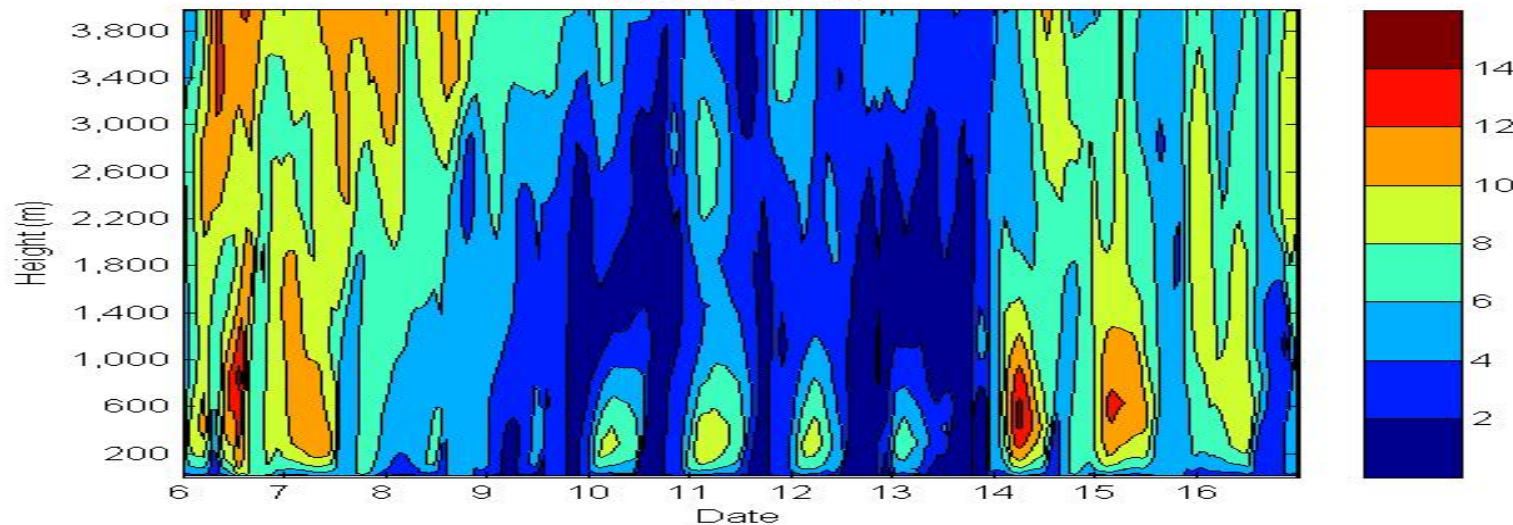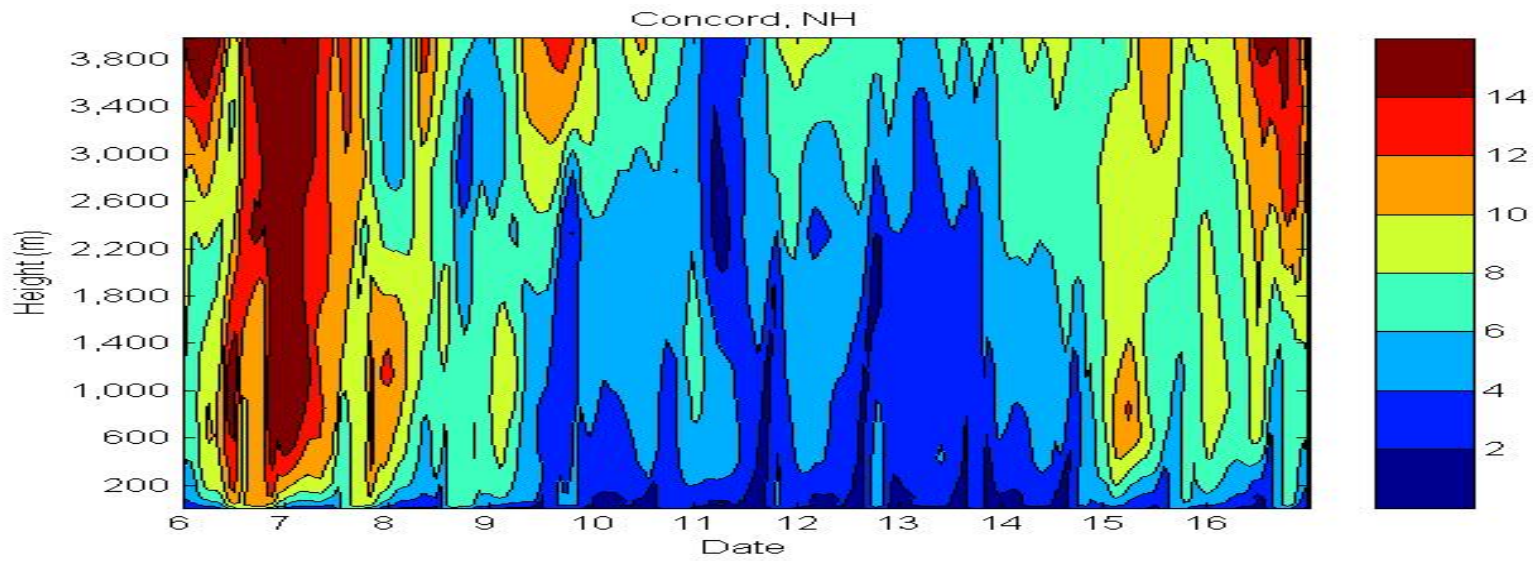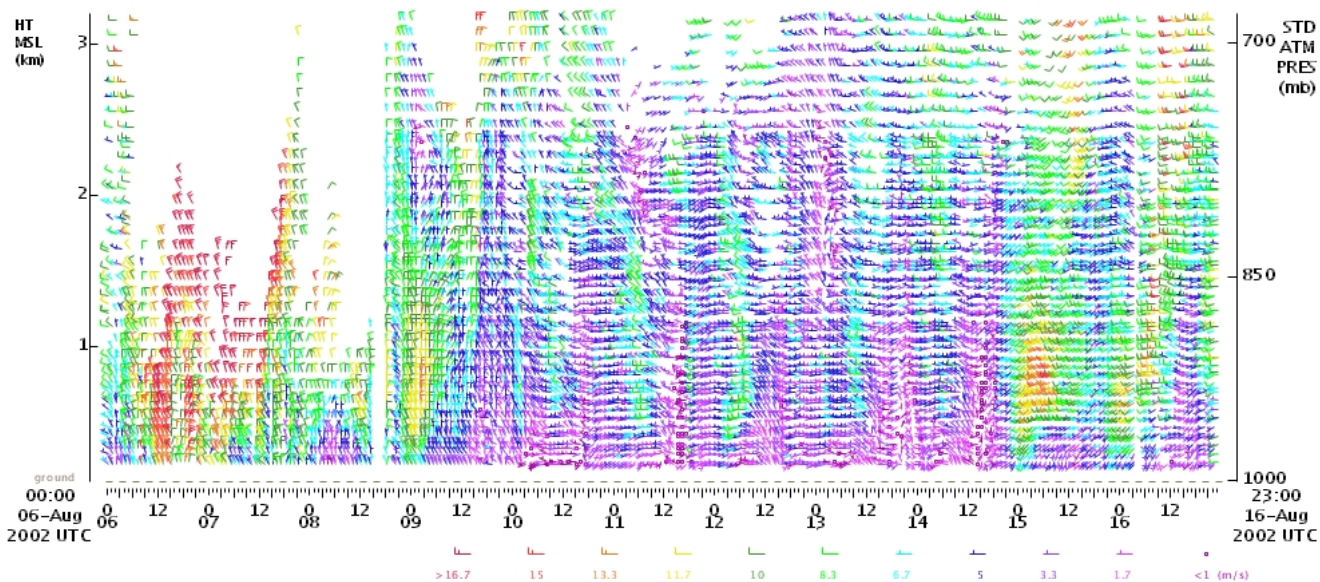
# Evaluation of 2002 Annual 12km MM5 Surface Parameters for OTC Modeling

*Shan He and Gary Kleiman*

## NESCAUM

And

*Winston Hao*

## NYDEC

Review of Application and Assessment of CMAQ in OTC

Albany, NY

November 16, 2005

NESCAUM

# Observation Network

# WIND

# WINTER   Wind Speed



Bias Wind Speed

CASTNet    TDL

m/s

Julian Day
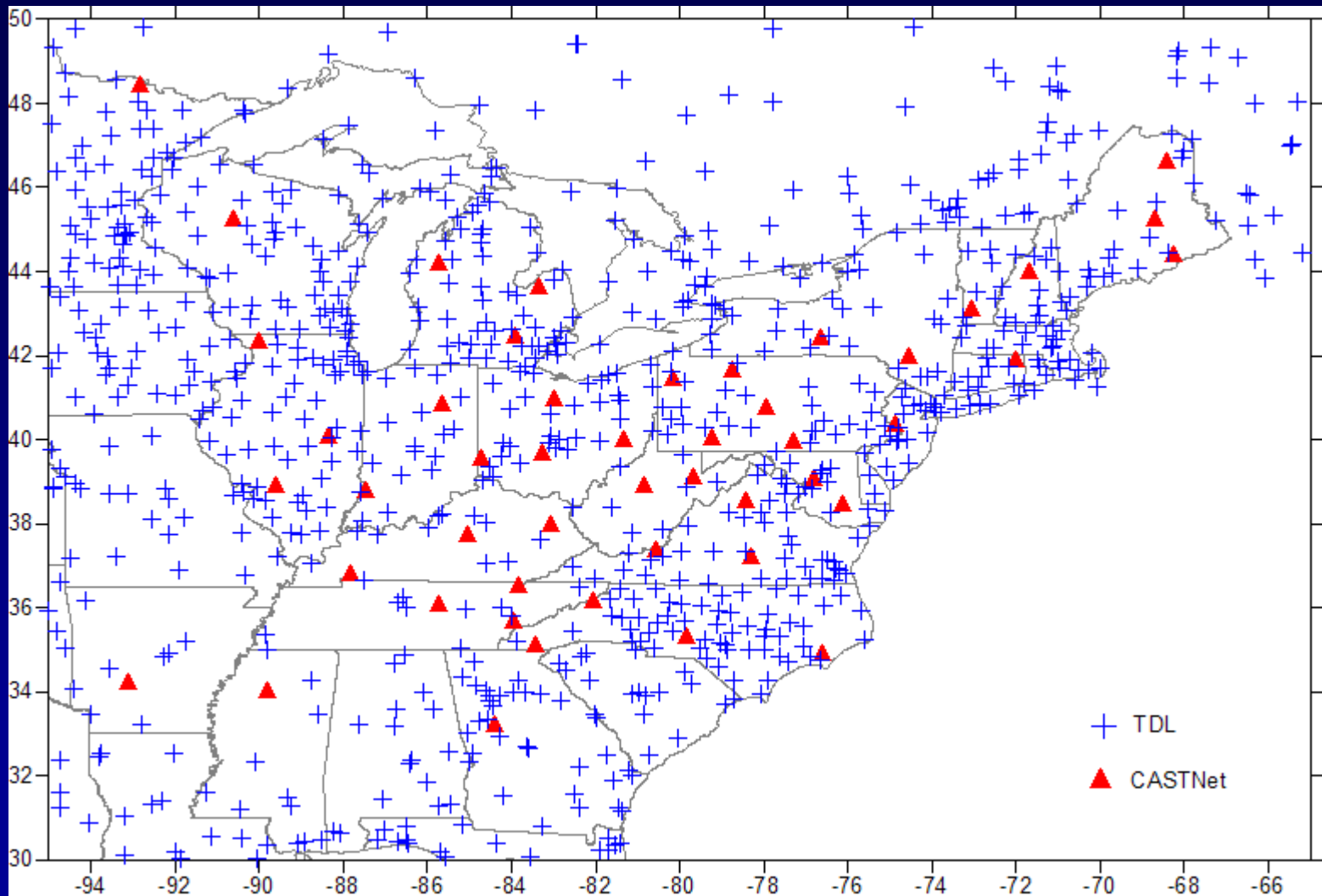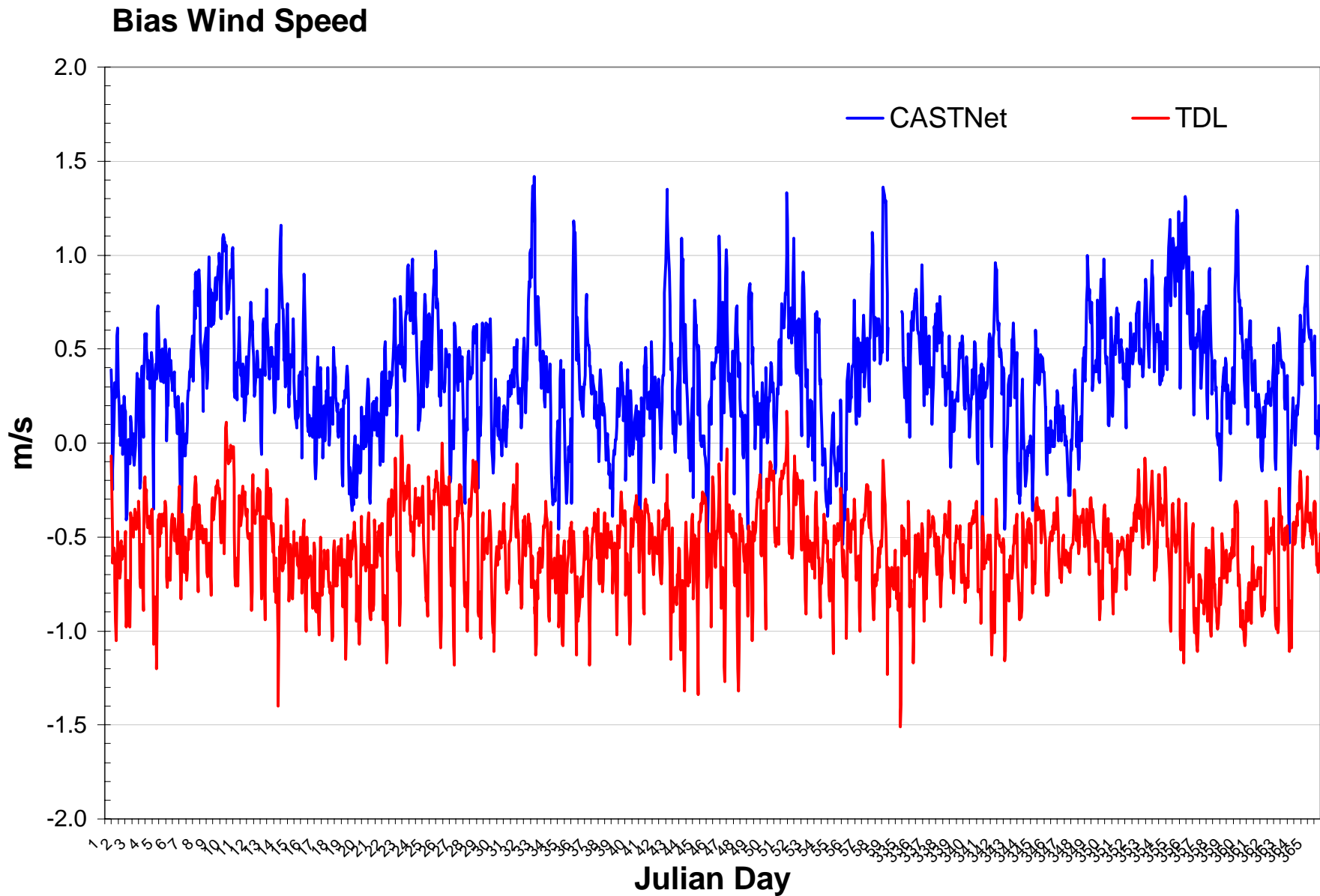
# WINTER   Wind Speed (II)
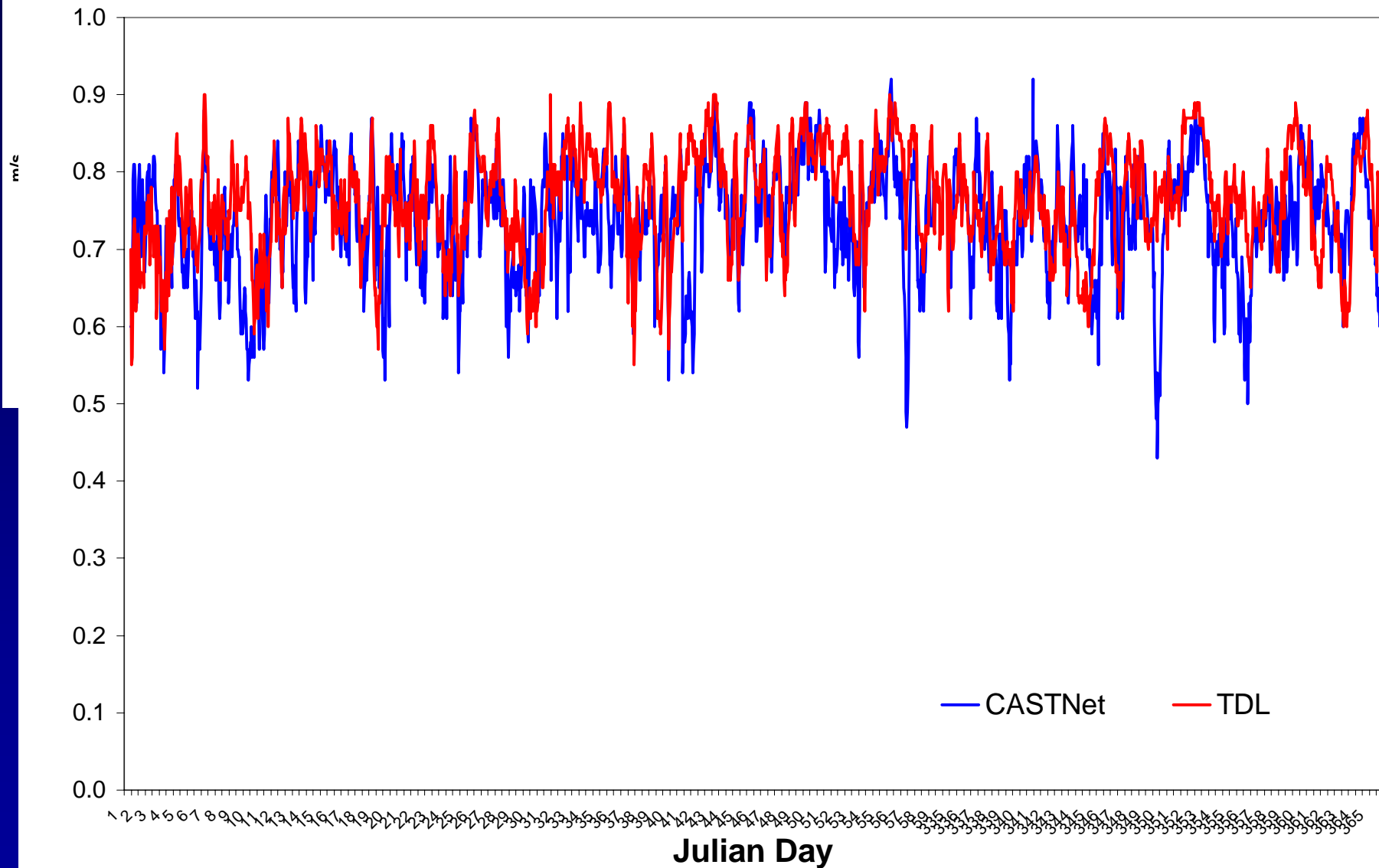


IOA Wind Speed

# WINTER   Wind Direction



Bias Wind Direction
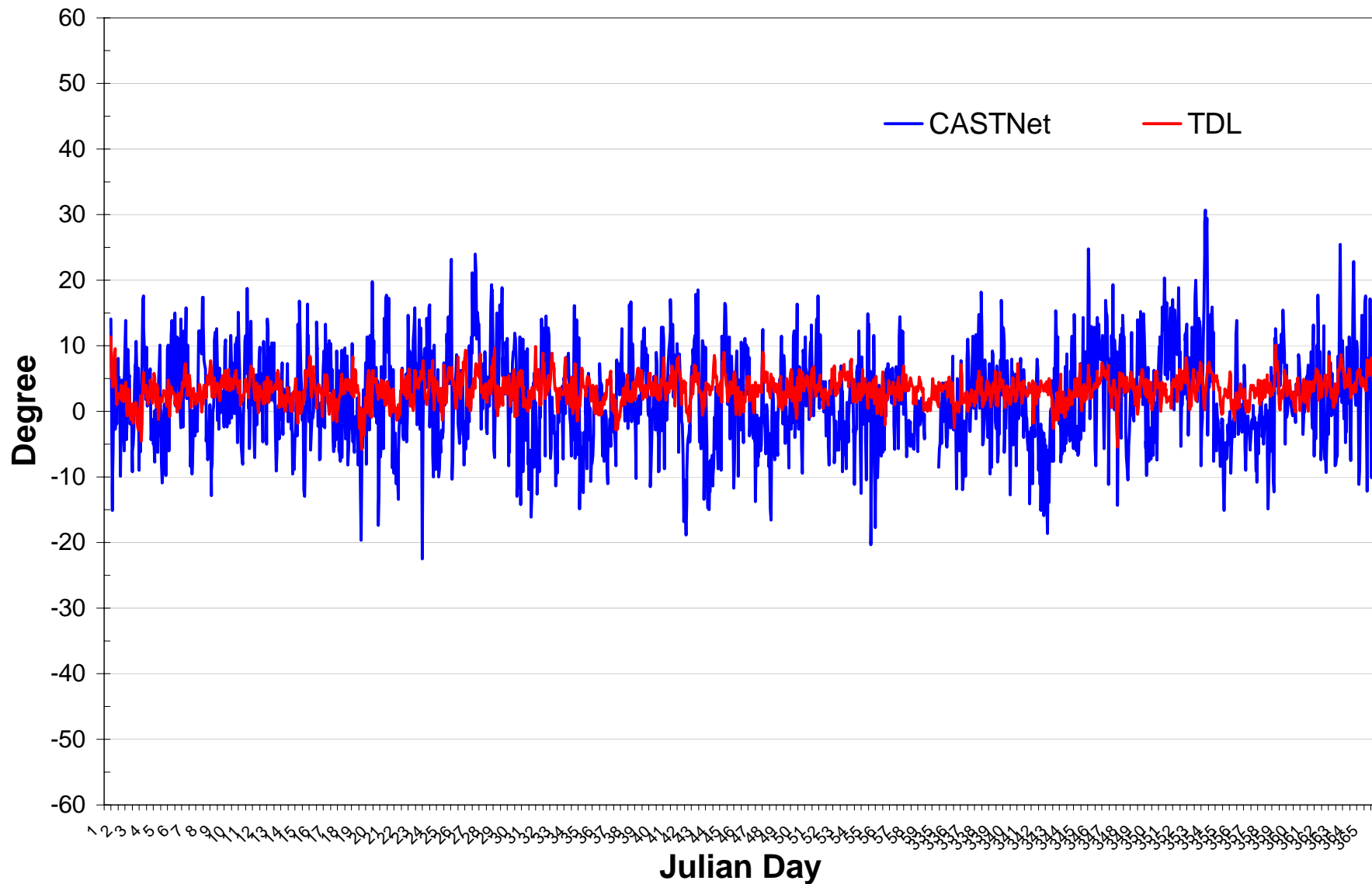
SPRING Wind Speed

# SPRING   Wind Speed (II)



**IOA Wind Speed**

m/s

CASTNet — TDL

**Julian Day**
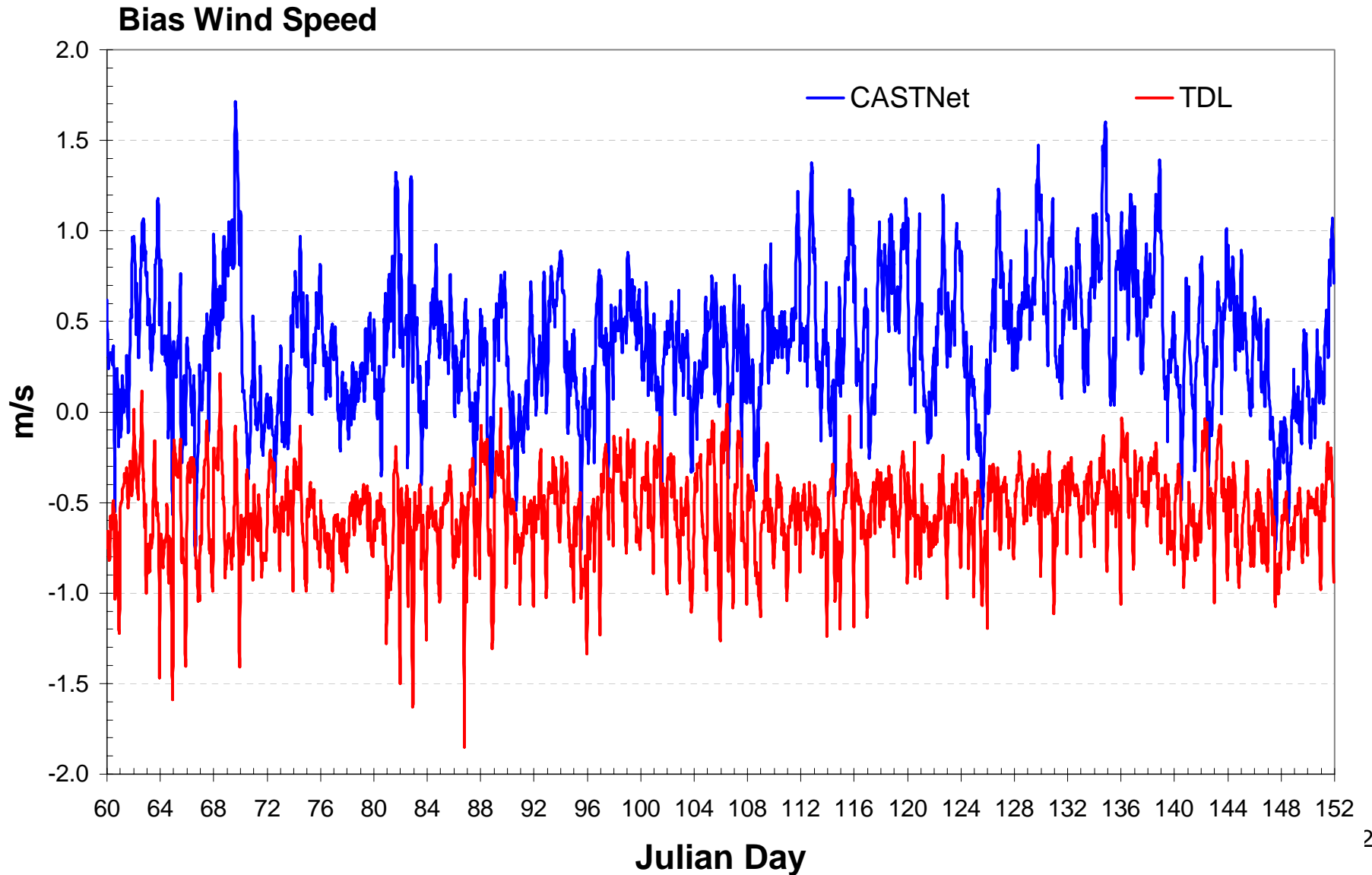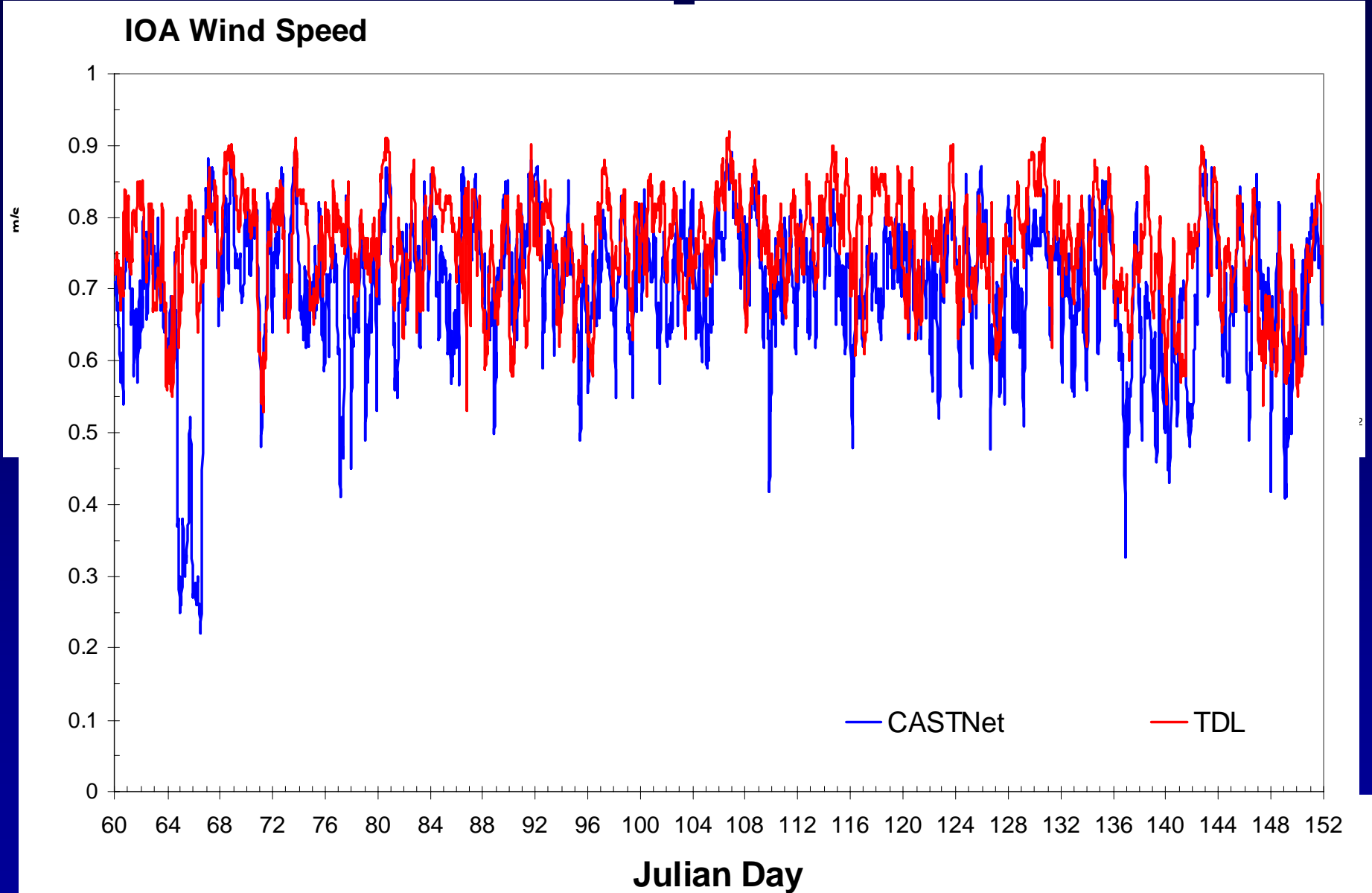
# SPRING   Wind Direction



Bias Wind Direction

Legend: CASTNet (blue), TDL (red)

Y-axis: Degree (−60 to 60)
X-axis: Julian Day (60 to 152)

# SUMMER Wind Speed



**Bias Wind Speed**

CASTNet — TDL
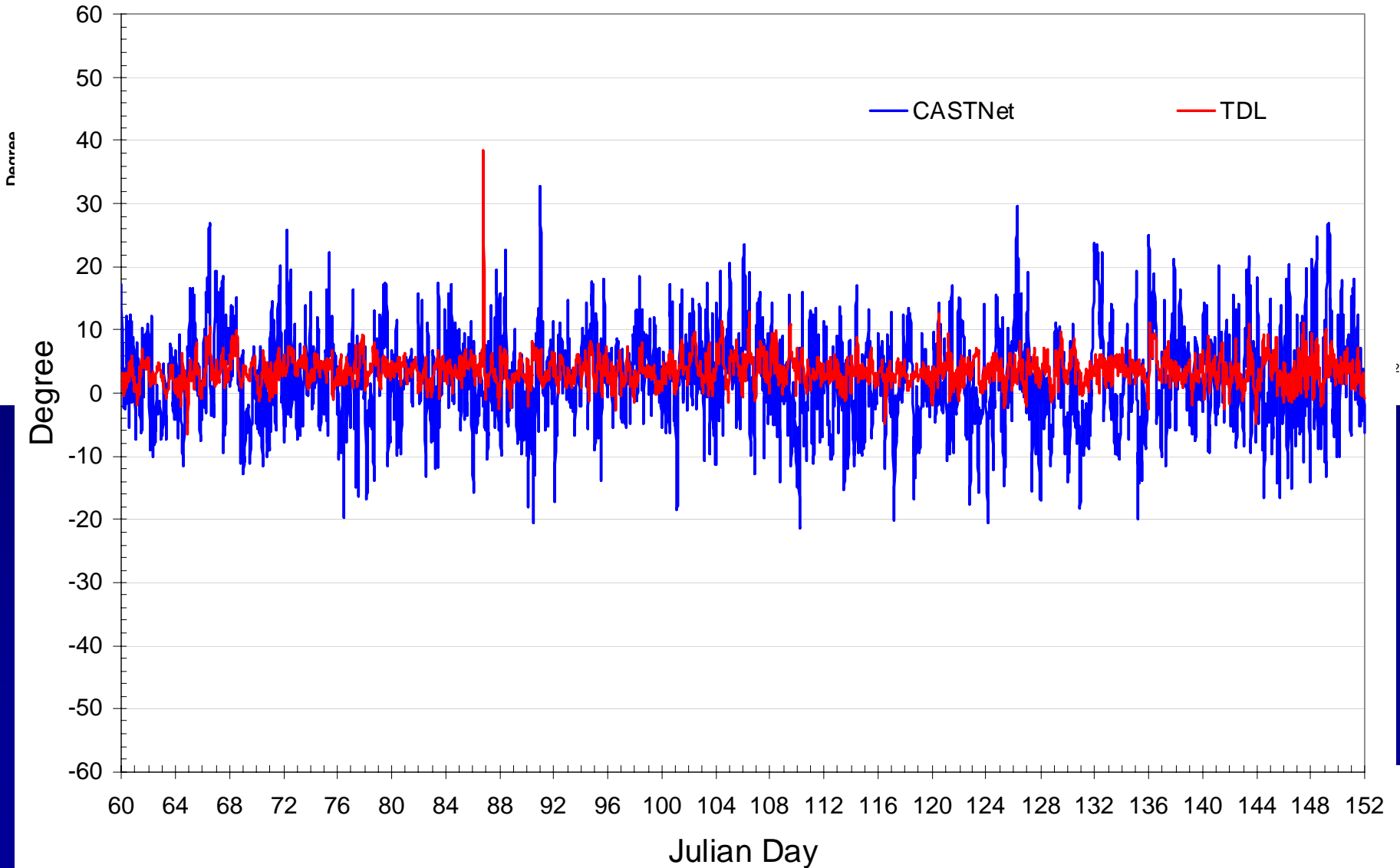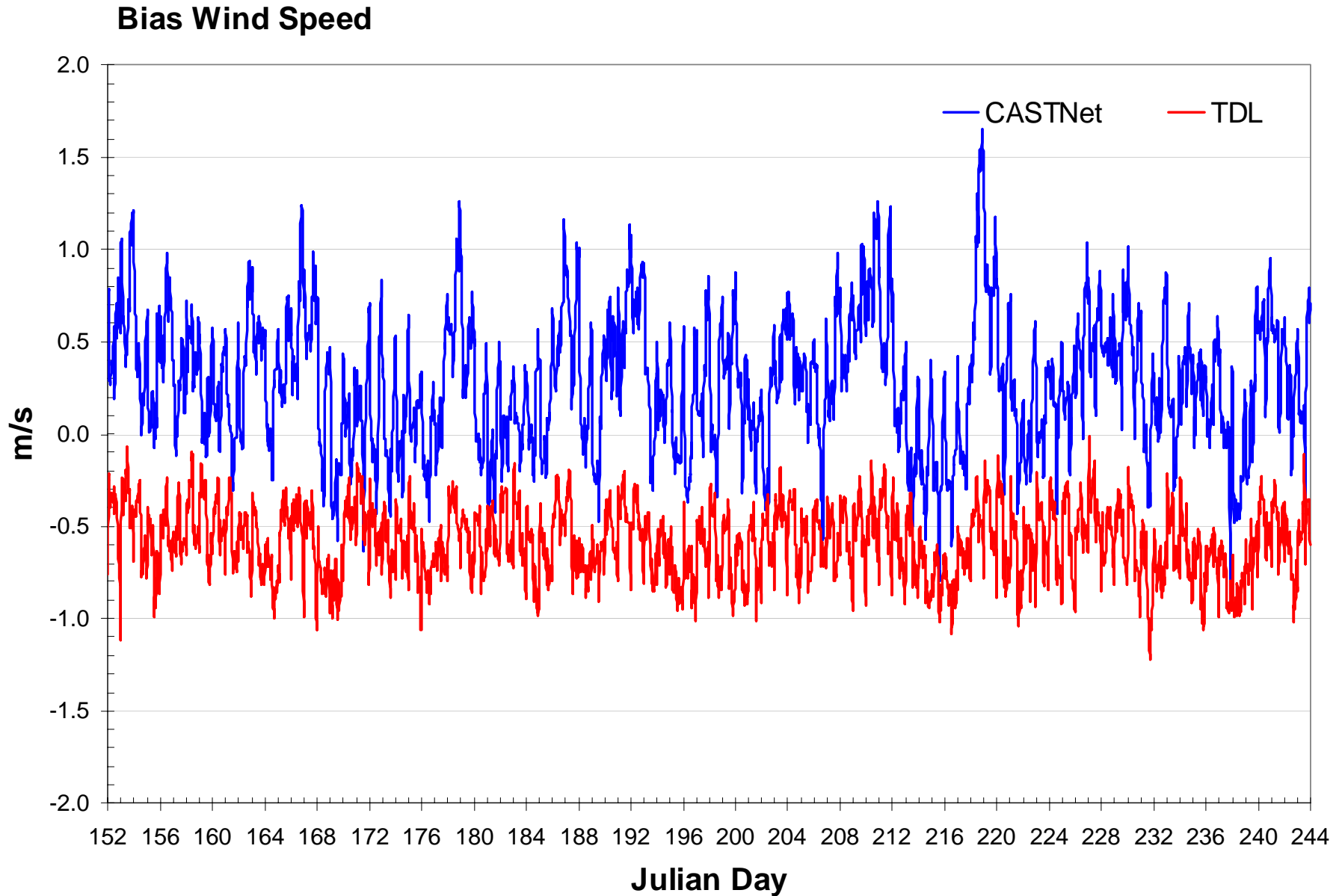
# SUMMER   Wind Speed (II)



IOA Wind Speed

CASTNet — TDL

Julian Day
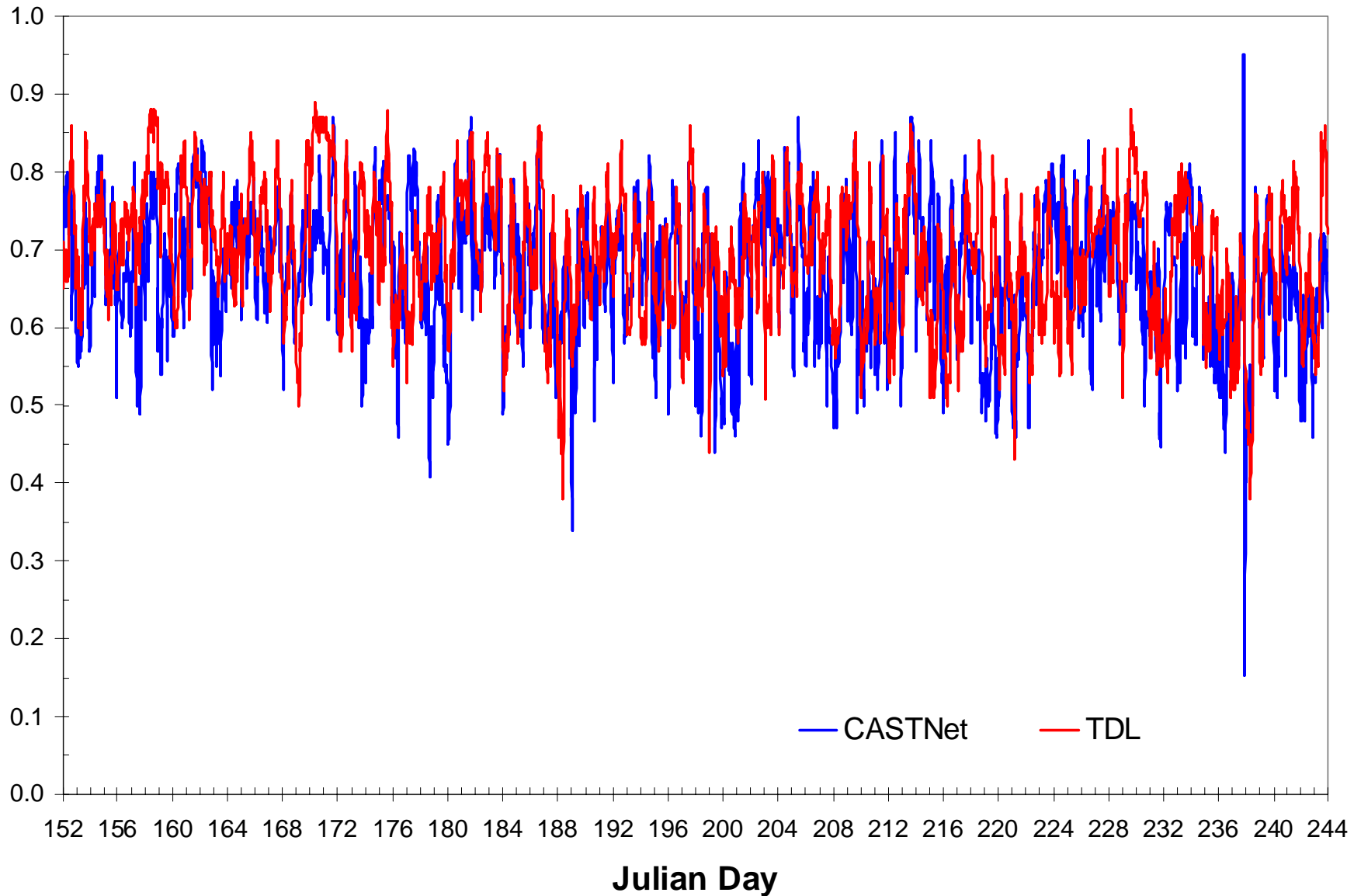
# SUMMER    Wind Direction



**Bias Wind Direction**

CASTNet — TDL
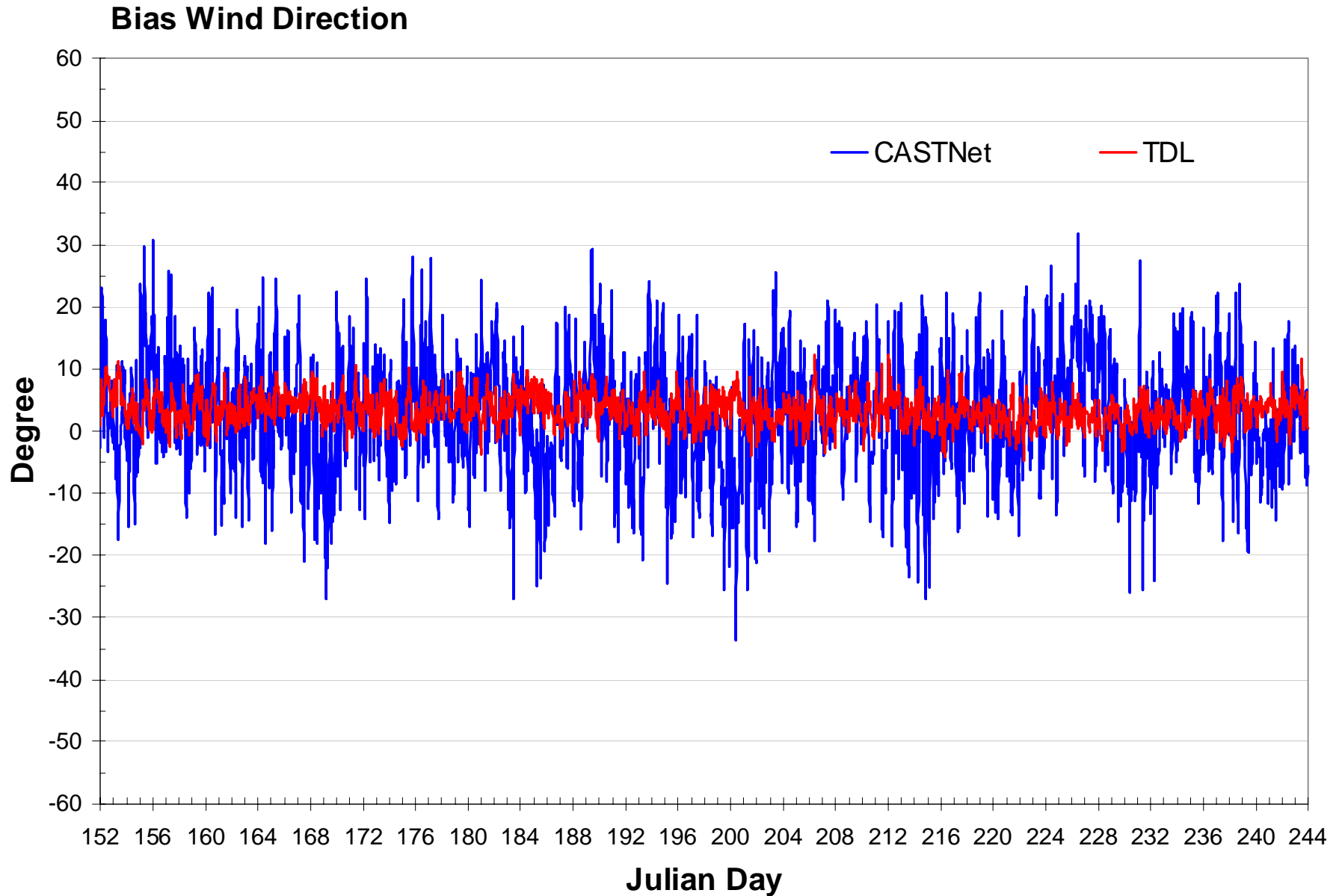
# FALL   Wind Speed



Bias Wind Speed

# FALL   Wind Speed (II)



**IOA Wind Speed**

Legend: CASTNet (blue), TDL (red)

**Julian Day**

# FALL   Wind Direction



Bias Wind Direction — CASTNet (blue), TDL (red). Y-axis: Degree (−60 to 60). X-axis: Julian Day (243 to 335).
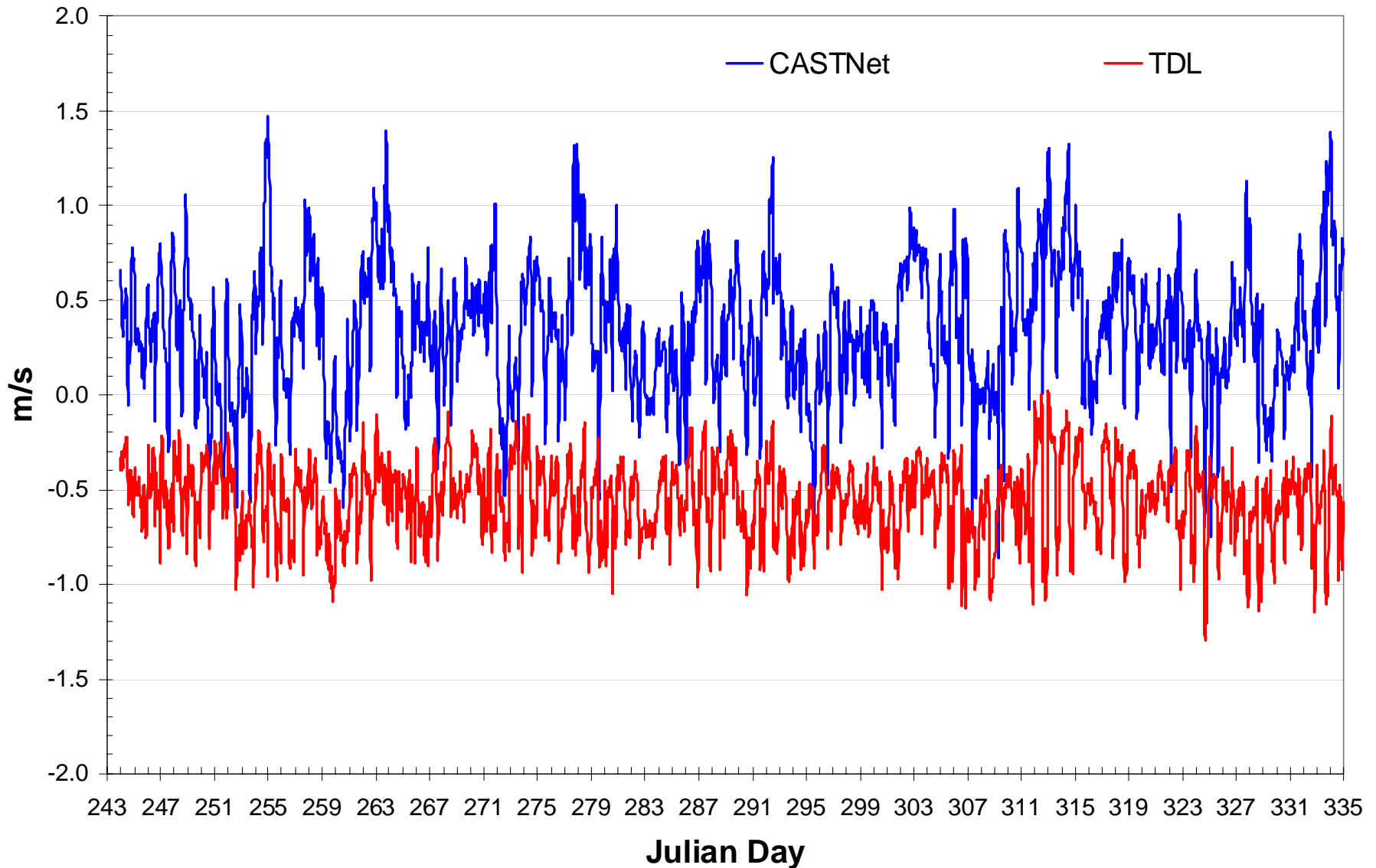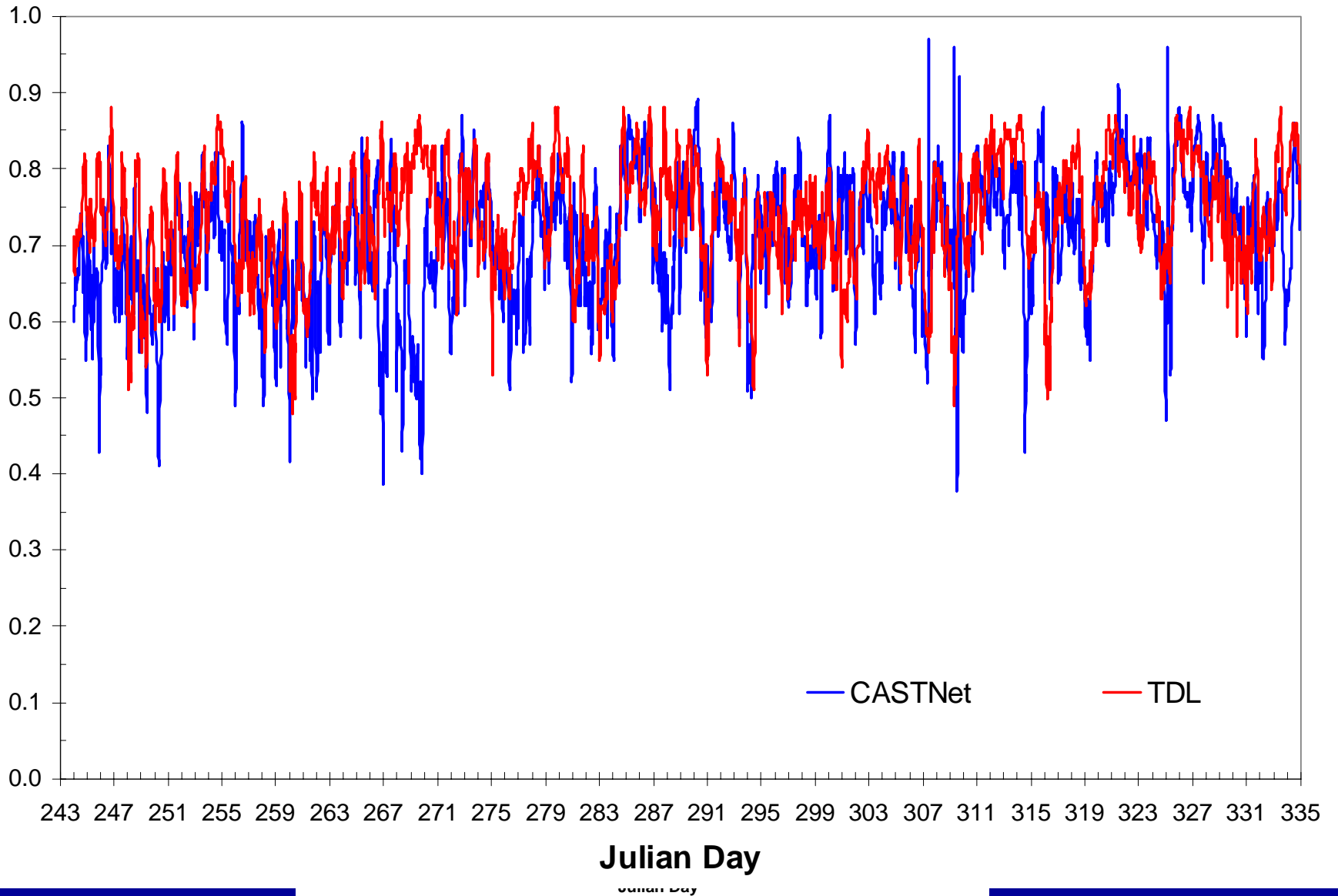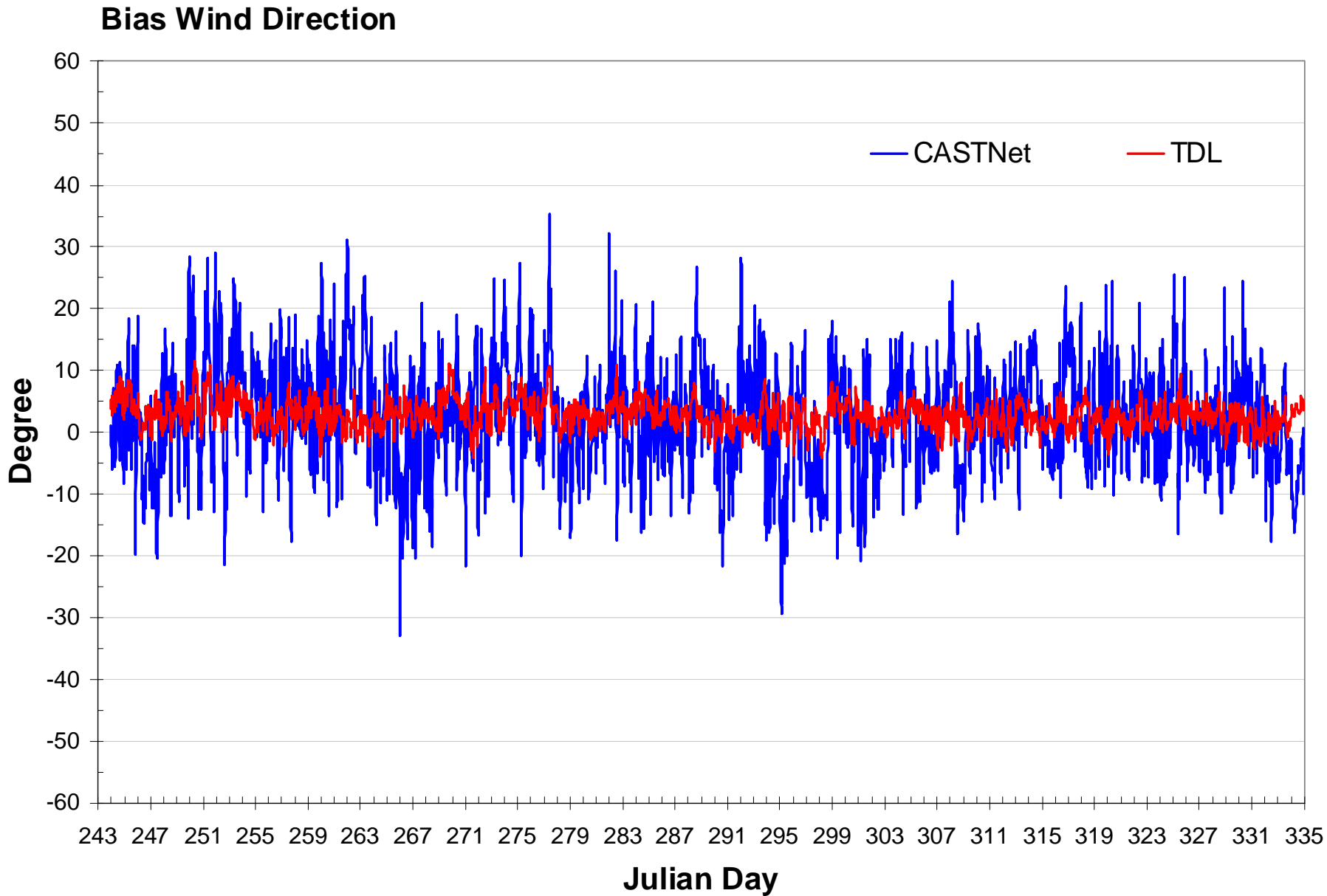
# WIND

| 2002 | Network | Wind Speed | | | | | | Wind Direction | | |
|---|---|---|---|---|---|---|---|---|---|---|
| | | Bias | | | IOA | | | Bias | | |
| | | Max | Min | Mean | Max | Min | Mean | Max | Min | Mean |
| JAN | CASTNET | 1.16 | -0.42 | 0.34 | 0.88 | 0.52 | 0.73 | 23.98 | -22.55 | 2.54 |
| | TDL | 0.11 | -1.40 | -0.53 | 0.90 | 0.55 | 0.74 | 11.42 | -5.81 | 3.12 |
| FEB | CASTNET | 1.42 | -0.61 | 0.31 | 0.92 | 0.47 | 0.75 | 18.55 | -20.29 | 0.88 |
| | TDL | 0.17 | -1.51 | -0.56 | 0.90 | 0.55 | 0.79 | 8.98 | -2.80 | 3.31 |
| MAR | CASTNET | 1.70 | -0.79 | 0.31 | 0.89 | 0.22 | 0.70 | 26.54 | -20.04 | 1.93 |
| | TDL | 0.21 | -1.85 | -0.59 | 0.91 | 0.53 | 0.76 | 38.45 | -6.45 | 3.48 |
| APR | CASTNET | 1.37 | -0.76 | 0.38 | 0.89 | 0.42 | 0.73 | 32.74 | -21.19 | 2.49 |
| | TDL | 0.04 | -1.33 | -0.55 | 0.92 | 0.58 | 0.77 | 12.80 | -4.59 | 3.61 |
| MAY | CASTNET | 1.60 | -0.76 | 0.44 | 0.88 | 0.33 | 0.69 | 29.64 | -20.58 | 2.33 |
| | TDL | -0.04 | -1.19 | -0.52 | 0.91 | 0.54 | 0.74 | 11.25 | -4.80 | 3.53 |
| JUN | CASTNET | 1.25 | -0.63 | 0.28 | 0.87 | 0.41 | 0.69 | 30.65 | -26.33 | 3.33 |
| | TDL | -0.07 | -1.11 | -0.56 | 0.89 | 0.50 | 0.73 | 11.15 | -3.65 | 3.89 |
| JUL | CASTNET | 1.26 | -0.58 | 0.31 | 0.87 | 0.34 | 0.66 | 29.26 | -33.34 | 1.44 |
| | TDL | -0.14 | -1.01 | -0.58 | 0.86 | 0.38 | 0.68 | 12.30 | -3.84 | 3.62 |
| AUG | CASTNET | 1.65 | -0.87 | 0.24 | 0.95 | 0.16 | 0.65 | 31.83 | -26.96 | 2.34 |
| | TDL | -0.02 | -1.22 | -0.61 | 0.88 | 0.38 | 0.67 | 11.76 | -4.67 | 2.74 |
| SEP | CASTNET | 1.47 | -0.75 | 0.30 | 0.87 | 0.39 | 0.67 | 30.95 | -32.73 | 3.01 |
| | TDL | -0.09 | -1.09 | -0.54 | 0.88 | 0.48 | 0.72 | 11.54 | -4.19 | 3.31 |
| OCT | CASTNET | 1.32 | -0.72 | 0.32 | 0.89 | 0.50 | 0.72 | 35.10 | -28.90 | 1.39 |
| | TDL | -0.10 | -1.05 | -0.56 | 0.88 | 0.51 | 0.74 | 10.82 | -4.09 | 2.81 |
| NOV | CASTNET | 1.39 | -0.86 | 0.37 | 0.97 | 0.38 | 0.74 | 25.62 | -17.68 | 2.35 |
| | TDL | 0.02 | -1.29 | -0.57 | 0.88 | 0.49 | 0.75 | 9.30 | -3.58 | 2.28 |
| DEC | CASTNET | 1.31 | -0.53 | 0.39 | 0.92 | 0.43 | 0.74 | 30.70 | -18.60 | 2.69 |
| | TDL | -0.08 | -1.17 | -0.59 | 0.89 | 0.60 | 0.76 | 10.08 | -5.47 | 3.41 |

- MM5 tends to overestimate wind speed at CASTNet sites, and underestimate wind speed at TDL sites
- Mean bias of MM5 wind speed to CASTNet wind speed is ~0.3 to 0.4m/s, while mean bias of MM5 wind speed to TDL wind speed is about ~-0.5 to -0.6m/s
- MM5 wind speed shows similar IOA (~0.7 to 0.8) for both CASTnet data and TDL data
- MM5 wind direction shows larger variation to CASTNet wind direction than to TDL wind direction
- However, mean bias of MM5 wind direction to CASTNet wind direction is smaller than mean bias of MM5 wind direction to TDL wind direction

NESCAUM

# TEMPERATURE

# WINTER   Temperature



Bias Surface Temperature

Legend: CASTNet (blue), TDL (red)

Y-axis: K, range from -5 to 5

X-axis: Julian Day
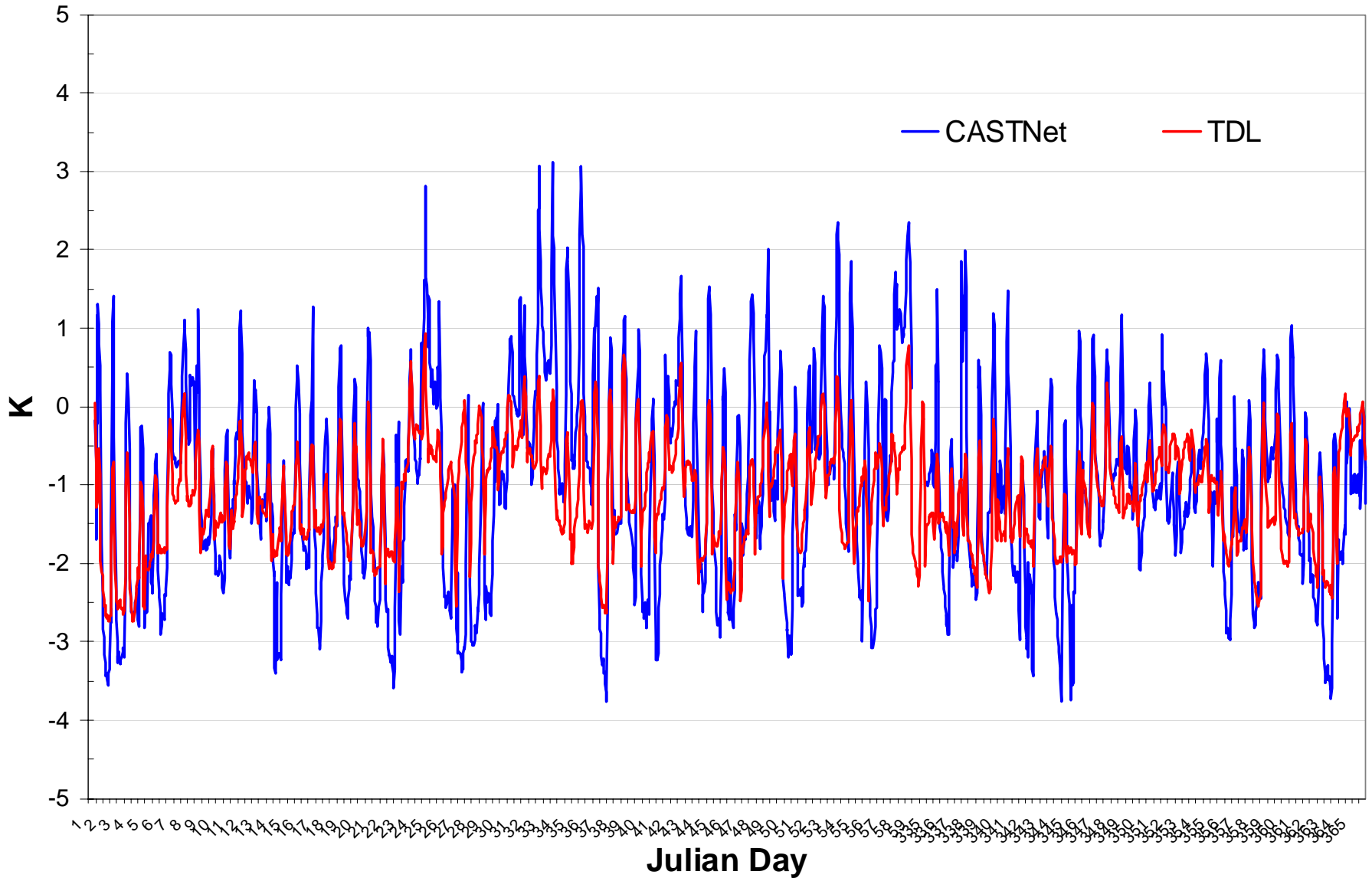
# WINTER Temperature (II)



IOA Surface Temperature

Julian Day
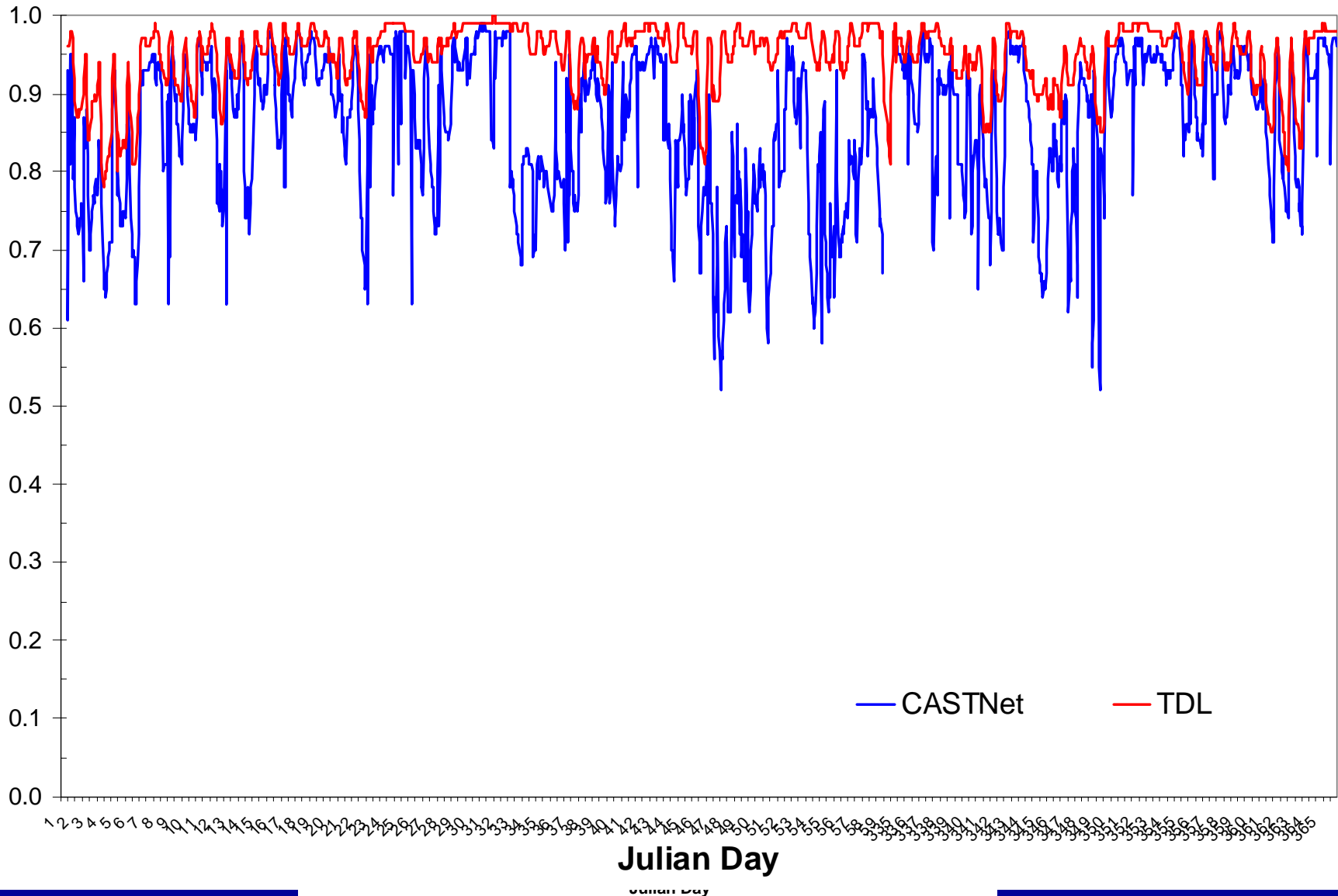
# SPRING Temperature



Bias Surface Temperature

# SPRING   Temperature (II)



**IOA Surface Temperature**

Legend: CASTNet (blue), TDL (red)

X-axis: **Julian Day** (60 to 152)
Y-axis: 0.0 to 1.0
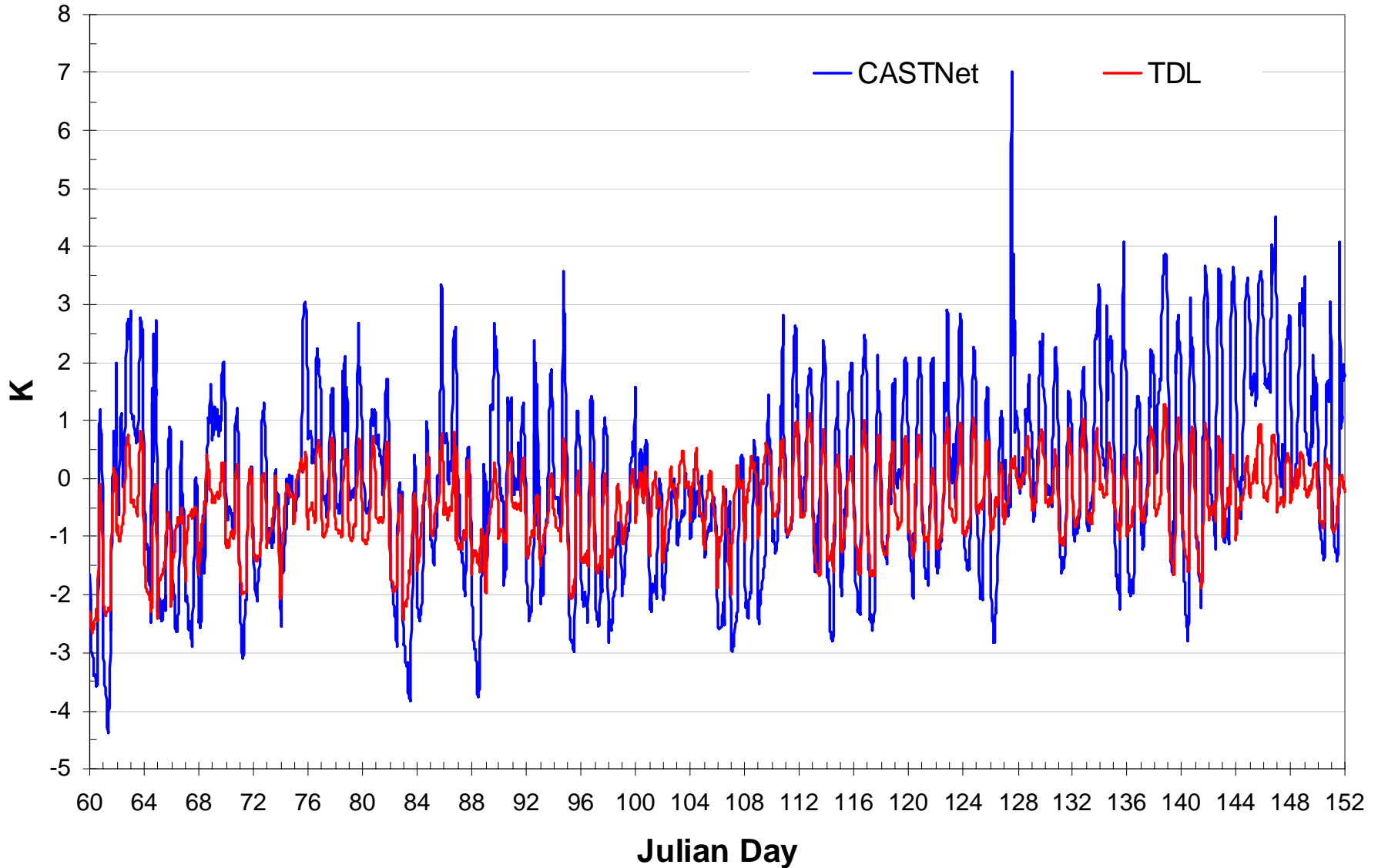
# SUMMER   Temperature
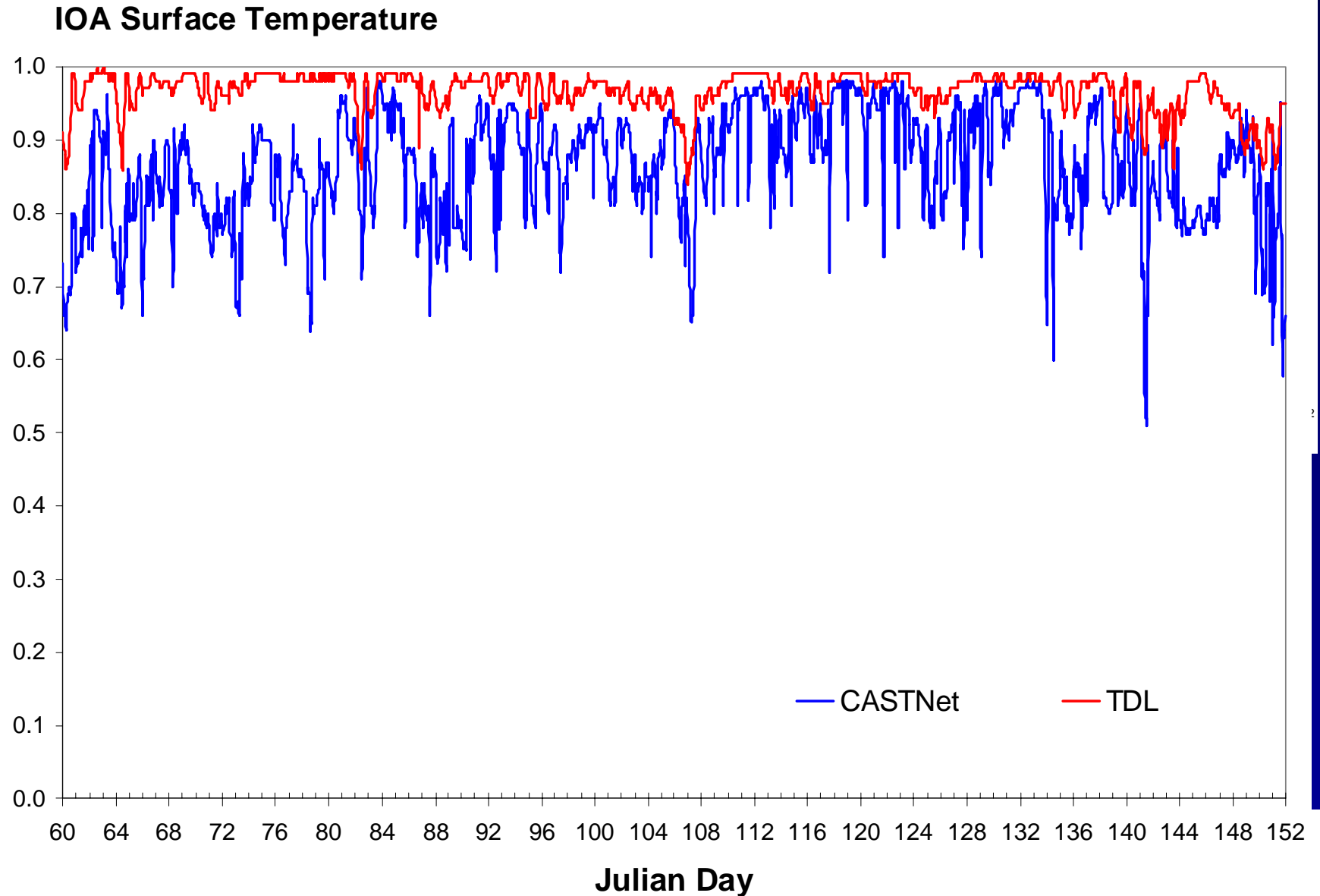


Bias Surface Temperature

# SUMMER   Temperature (II)



**IOA Surface Temperature**

Legend: — CASTNet — TDL

X-axis: Julian Day (152 to 244)
Y-axis: 0.0 to 1.0
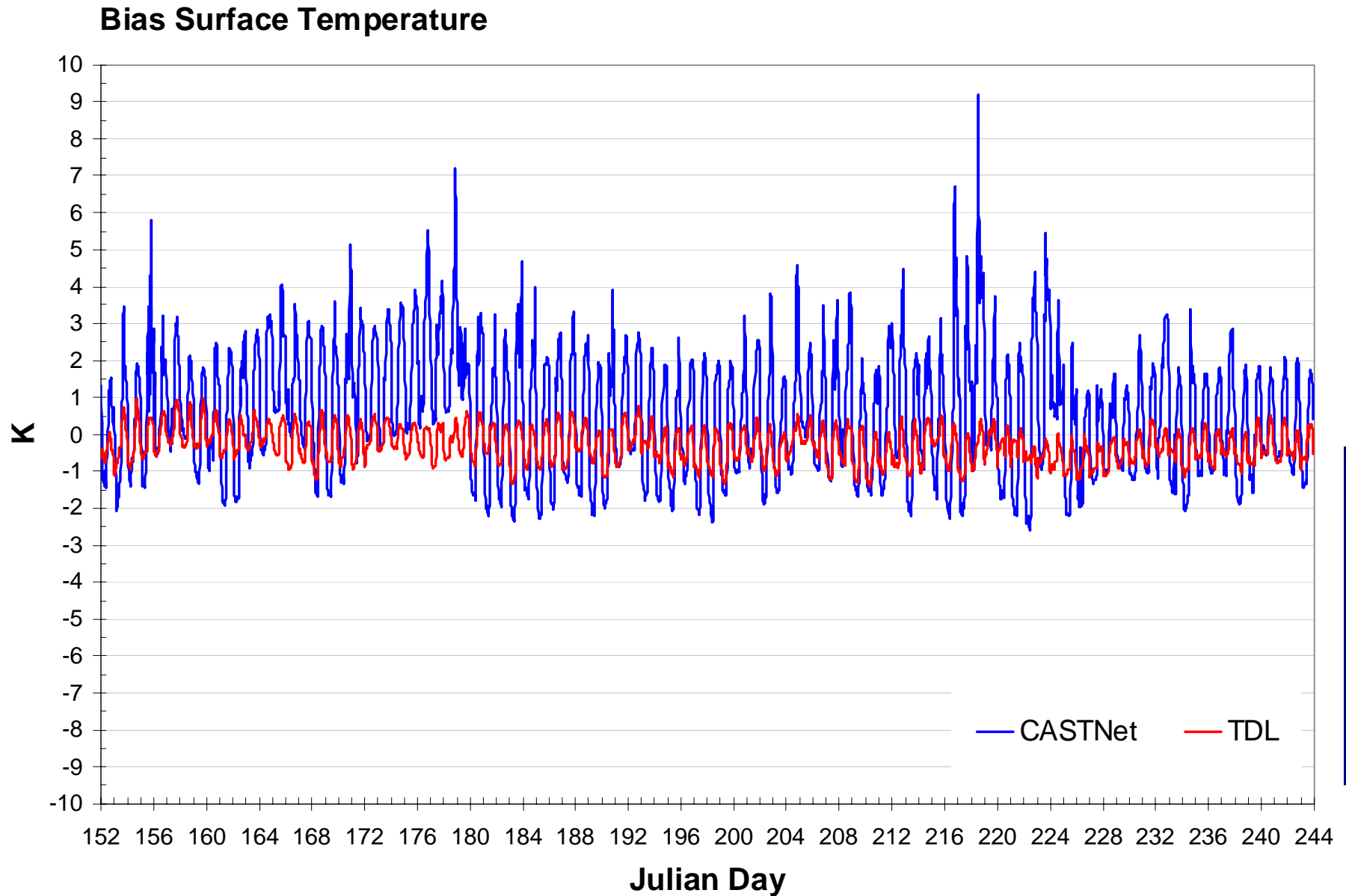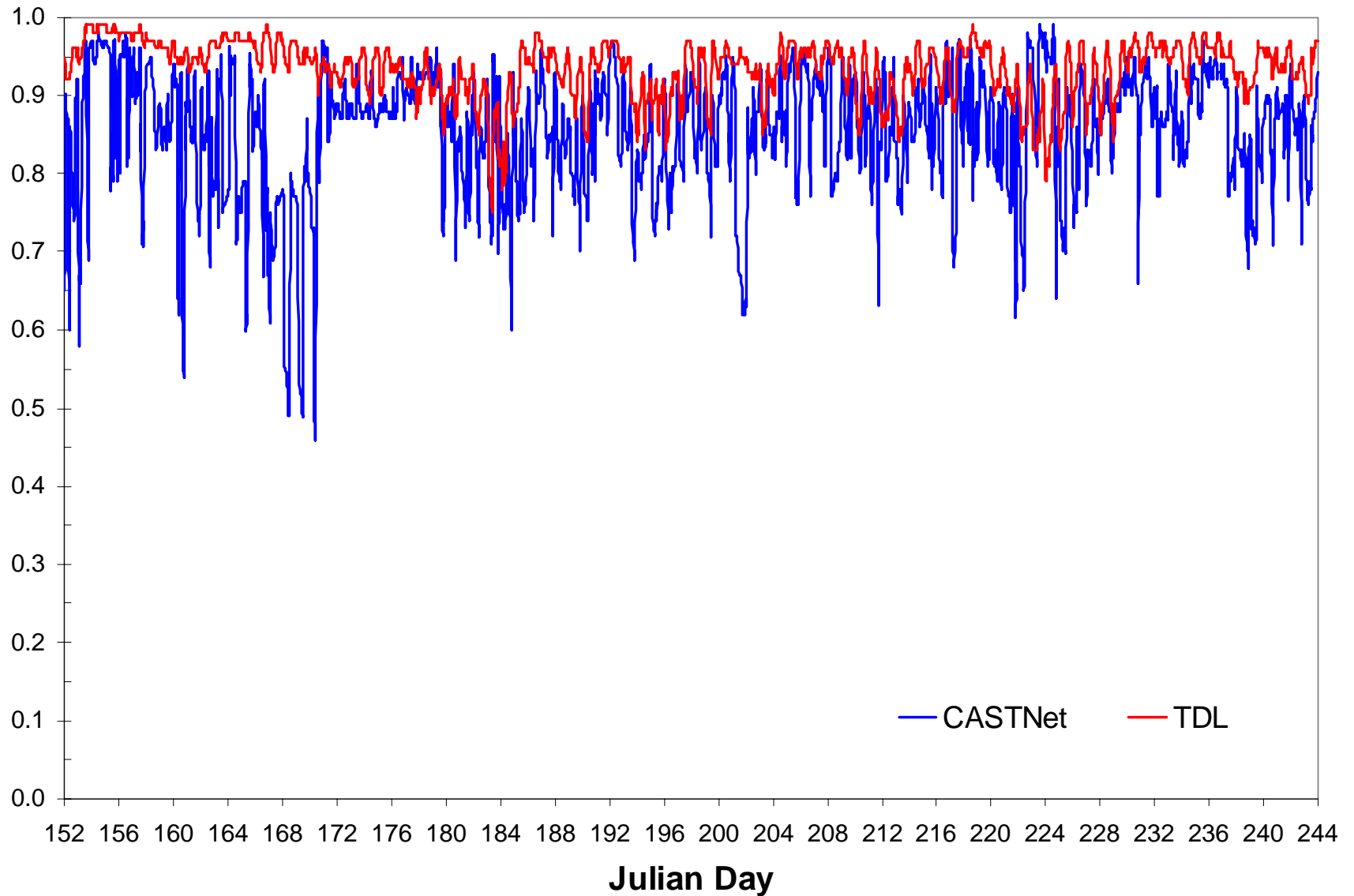
# FALL Temperature



**Bias Surface Temperature**
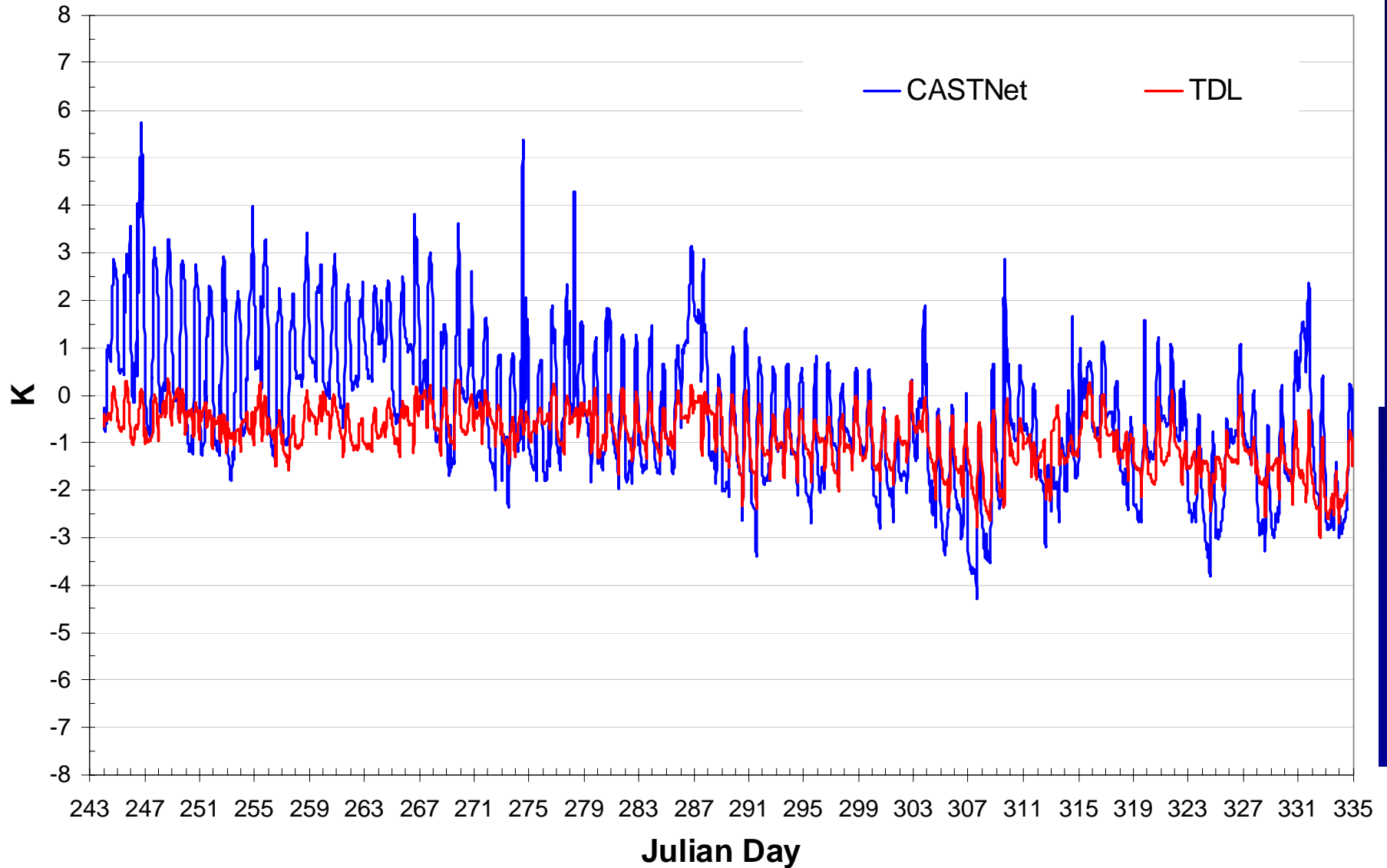
# FALL    Temperature (II)



IOA Surface Temperature

CASTNet — TDL

Julian Day
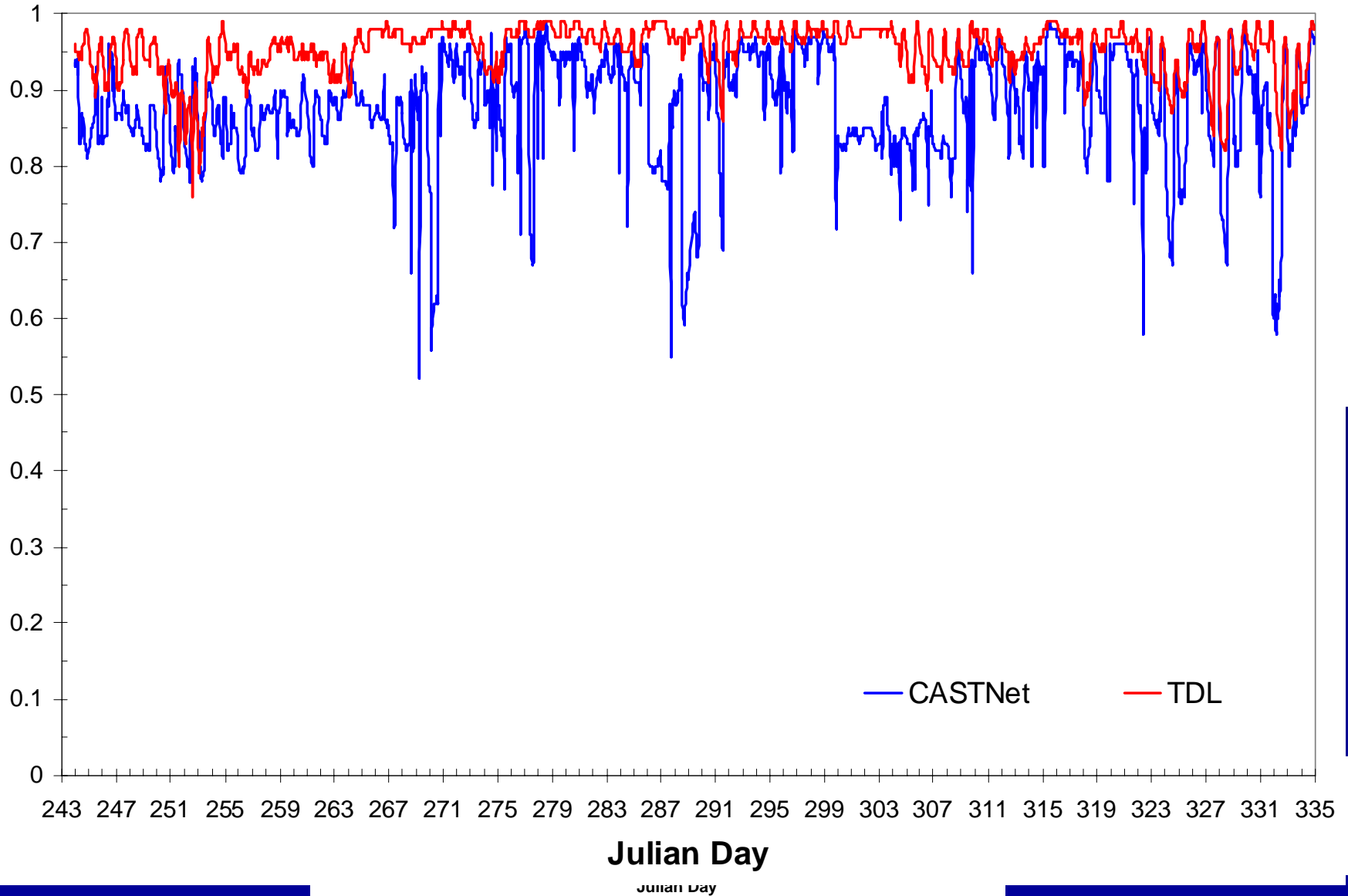
# TEMPERATURE

| 2002 | Network | Temperature | | | | | |
|------|---------|-------------|------|------|------|------|------|
| | | Bias | | | IOA | | |
| | | Max | Min | Mean | Max | Min | Mean |
| JAN | CASTNET | 2.81 | -3.59 | -1.25 | 0.99 | 0.61 | 0.88 |
| | TDL | 0.94 | -2.73 | -1.18 | 1.00 | 0.78 | 0.94 |
| FEB | CASTNET | 3.12 | -3.77 | -0.65 | 0.98 | 0.52 | 0.81 |
| | TDL | 0.79 | -2.64 | -1.00 | 0.99 | 0.81 | 0.96 |
| MAR | CASTNET | 3.31 | -4.39 | -0.35 | 0.98 | 0.64 | 0.83 |
| | TDL | 0.81 | -2.65 | -0.72 | 1.00 | 0.86 | 0.97 |
| APR | CASTNET | 3.52 | -2.97 | -0.52 | 0.98 | 0.65 | 0.90 |
| | TDL | 1.13 | -2.06 | -0.48 | 0.99 | 0.84 | 0.97 |
| MAY | CASTNET | 7.02 | -2.83 | 0.67 | 0.99 | 0.51 | 0.87 |
| | TDL | 1.27 | -1.88 | -0.18 | 0.99 | 0.86 | 0.96 |
| JUN | CASTNET | 7.13 | -2.23 | 1.03 | 0.98 | 0.46 | 0.85 |
| | TDL | 0.98 | -1.21 | -0.12 | 0.99 | 0.85 | 0.95 |
| JUL | CASTNET | 4.70 | -2.40 | 0.34 | 0.97 | 0.60 | 0.85 |
| | TDL | 0.74 | -1.38 | -0.34 | 0.98 | 0.75 | 0.92 |
| AUG | CASTNET | 9.03 | -2.59 | 0.32 | 0.99 | 0.62 | 0.86 |
| | TDL | 0.53 | -1.28 | -0.42 | 0.99 | 0.79 | 0.93 |
| SEP | CASTNET | 5.72 | -2.37 | 0.76 | 0.97 | 0.52 | 0.86 |
| | TDL | 0.34 | -1.57 | -0.54 | 0.99 | 0.76 | 0.94 |
| OCT | CASTNET | 5.17 | -3.39 | -0.56 | 0.99 | 0.55 | 0.89 |
| | TDL | 0.29 | -2.39 | -0.79 | 0.99 | 0.86 | 0.97 |
| NOV | CASTNET | 2.83 | -4.29 | -1.25 | 0.99 | 0.58 | 0.88 |
| | TDL | 0.25 | -2.99 | -1.35 | 0.99 | 0.82 | 0.95 |
| DEC | CASTNET | 1.98 | -3.76 | -1.17 | 0.98 | 0.52 | 0.88 |
| | TDL | 0.29 | -2.55 | -1.20 | 0.99 | 0.80 | 0.94 |

- MM5 tends to underestimate temperature at TDL sites all year, and at CASTNet sites for seasons other than 5month summer

- MM5 performs better on temperature for Summer than for Winter

- Unsystematic RMSE dominates RMSE at TDL sites consistently, while at CASTNet sites, RMSEU weights similar as RMSES

- MM5 shows good IOA at TDL sites (~0.9), better than at CASTNet sites (~0.8)

NESCAUM

# HUMIDITY

NESCAUM
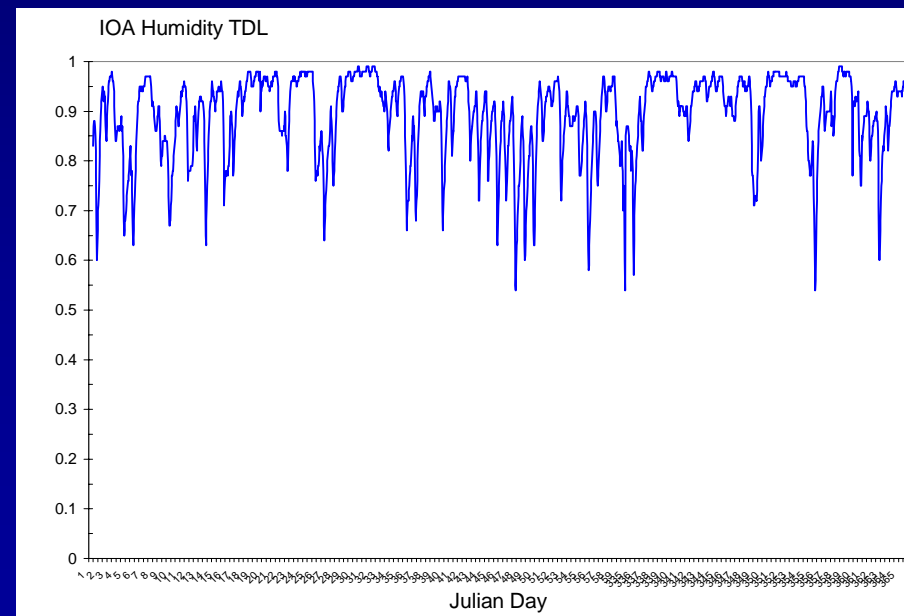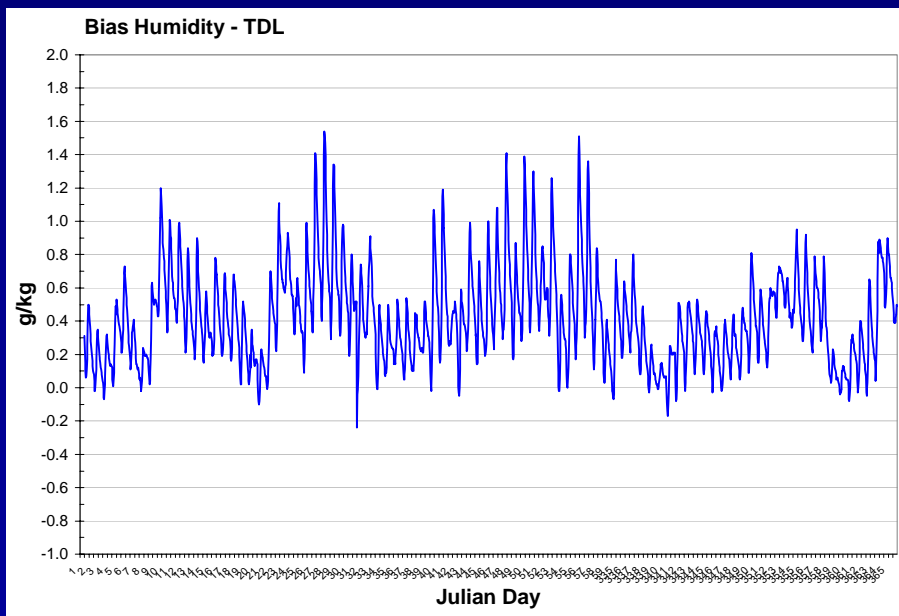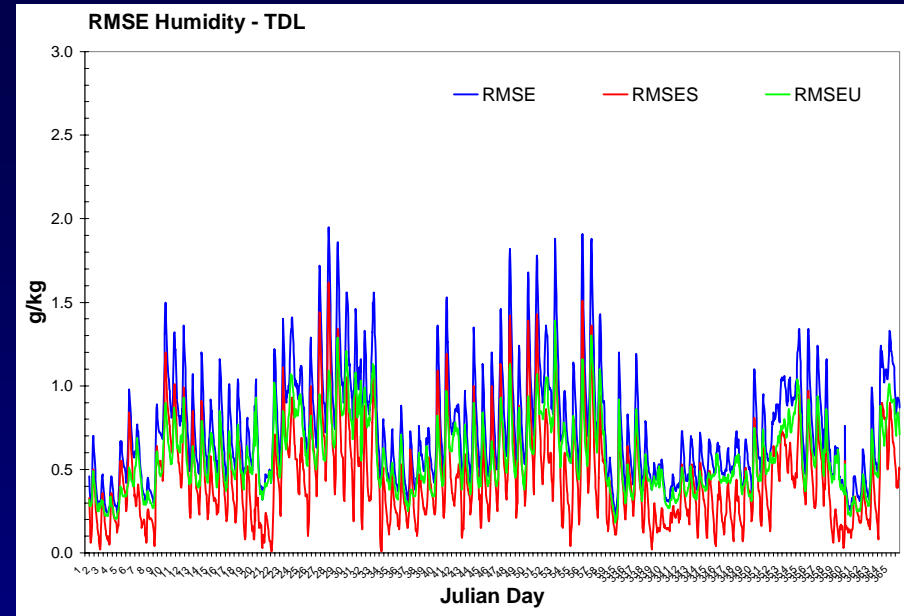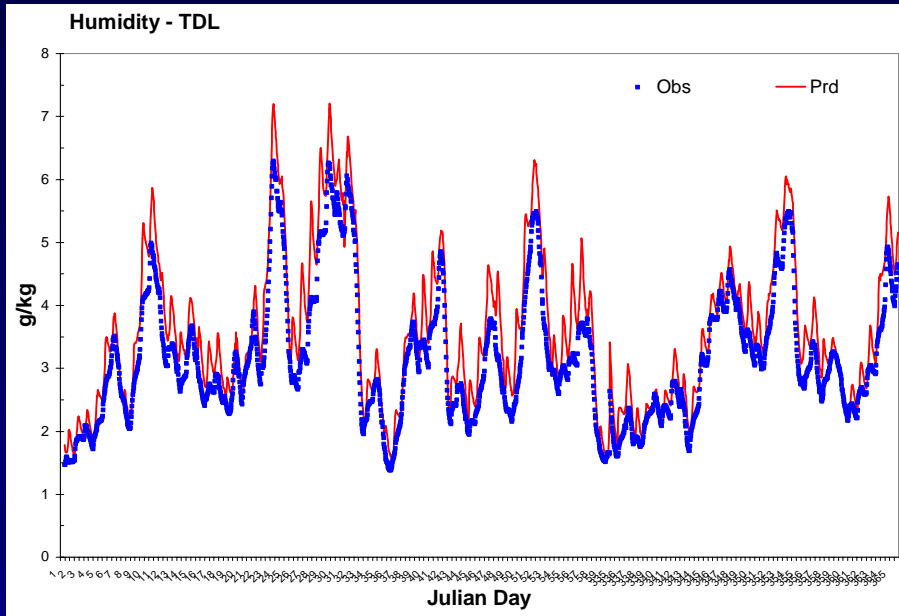
# WINTER    Humidity

# SPRING   Humidity
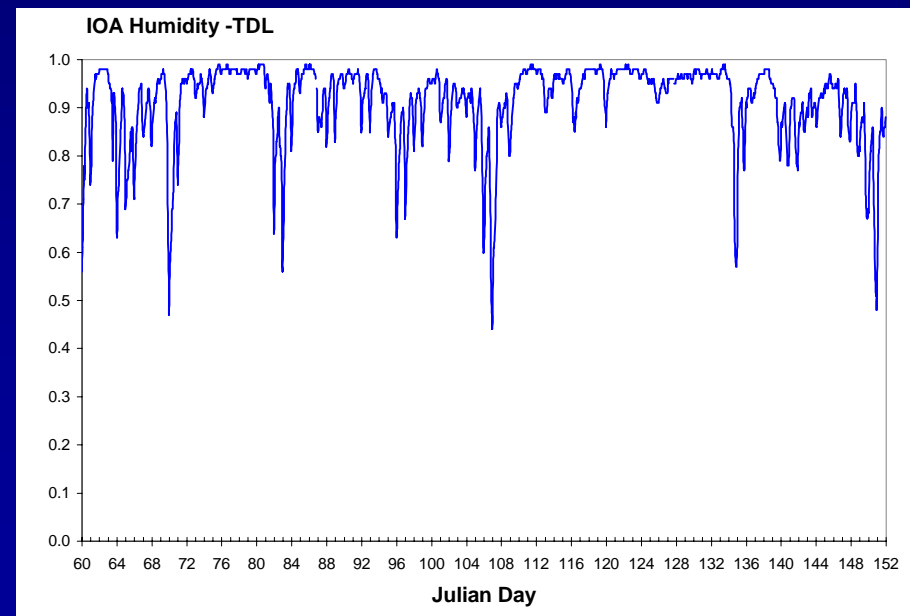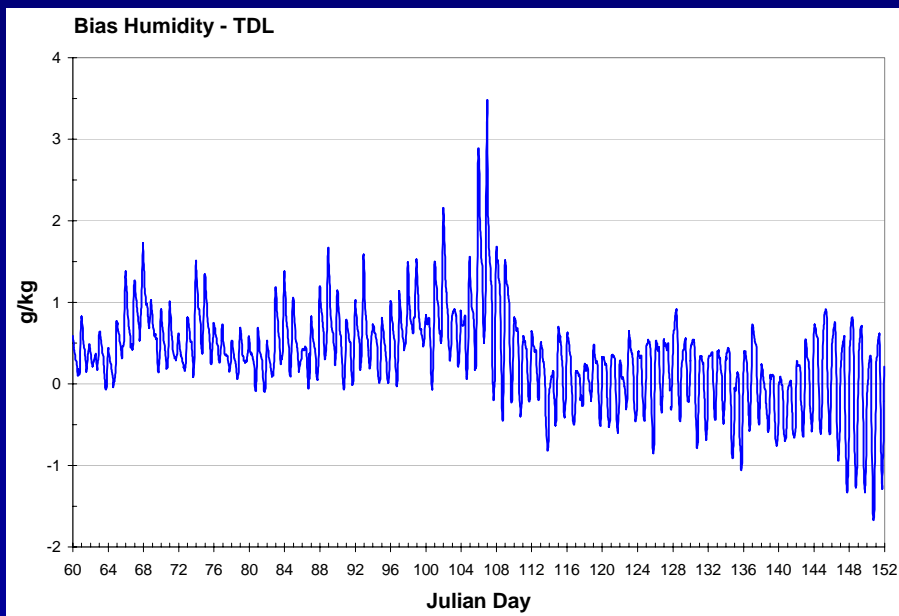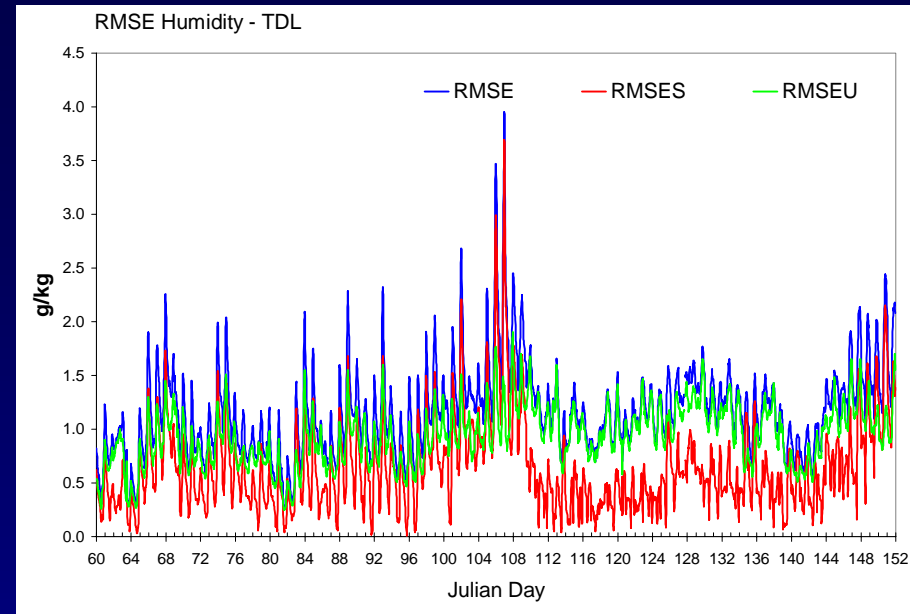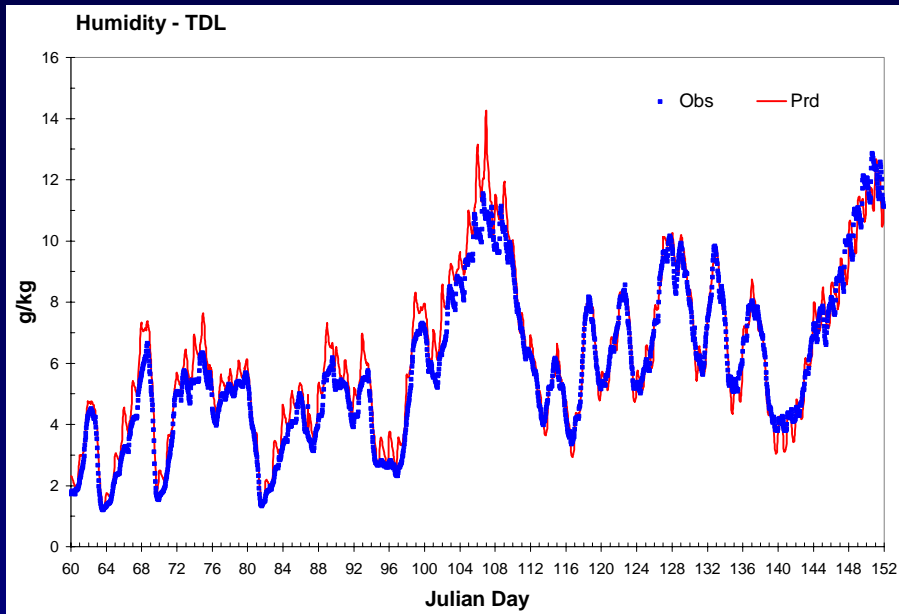
# SUMMER  Humidity
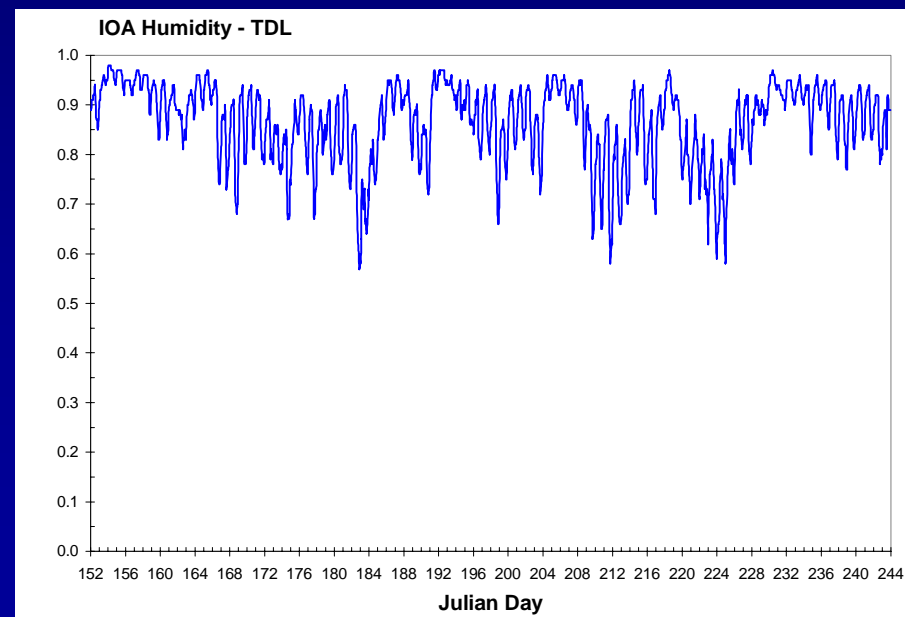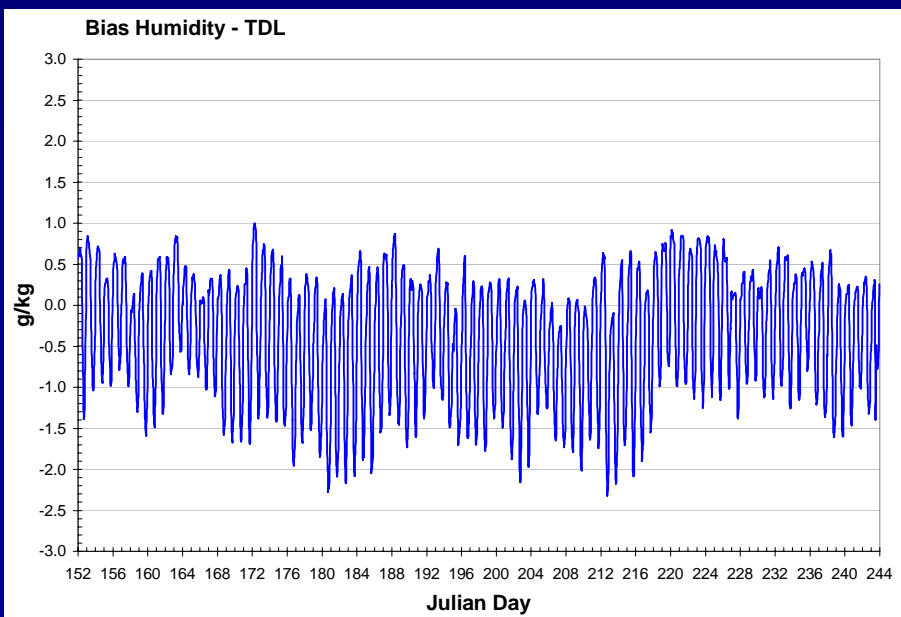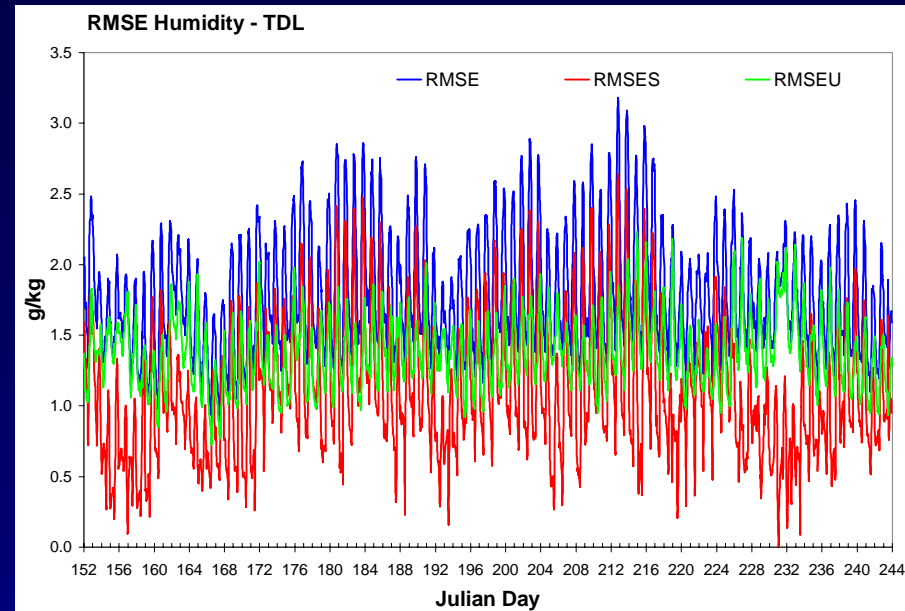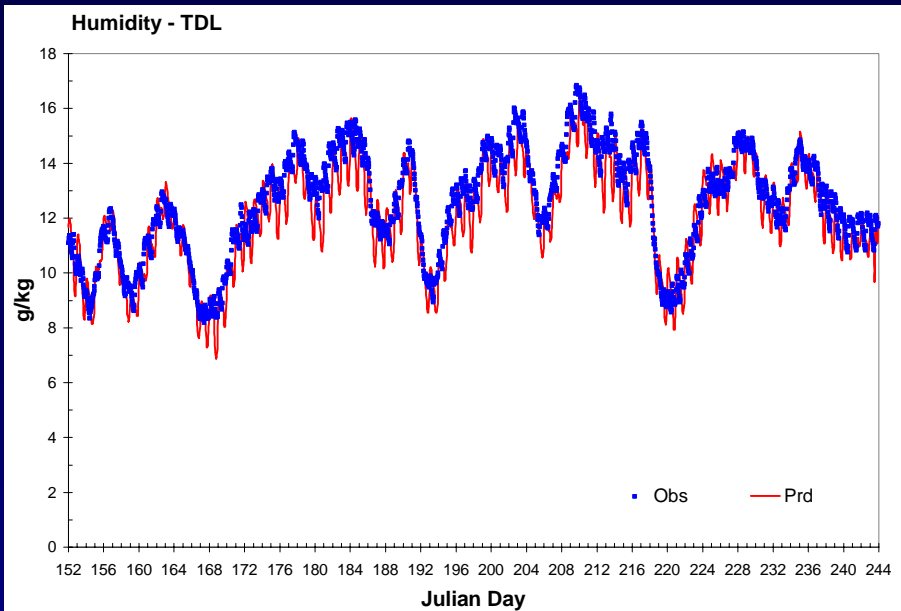
# FALL   Humidity
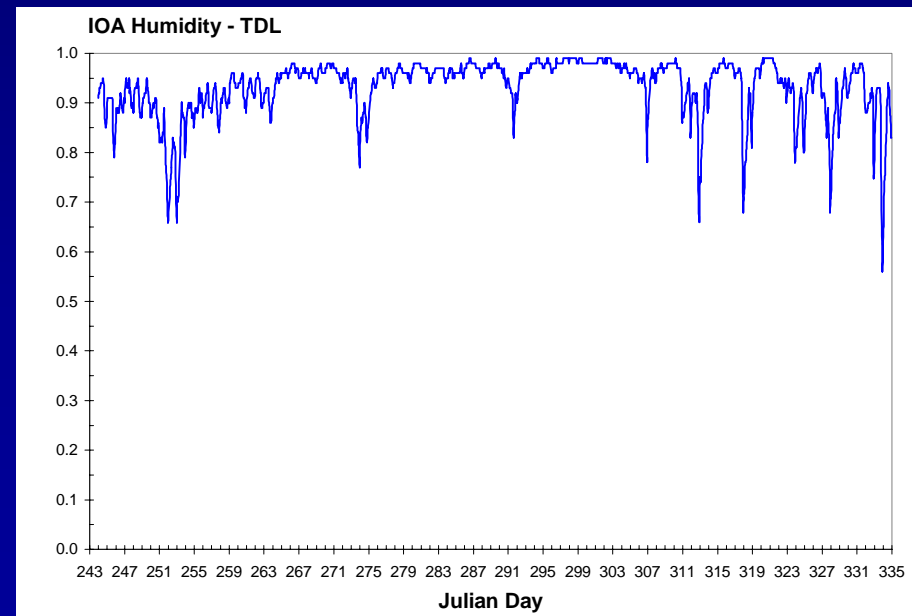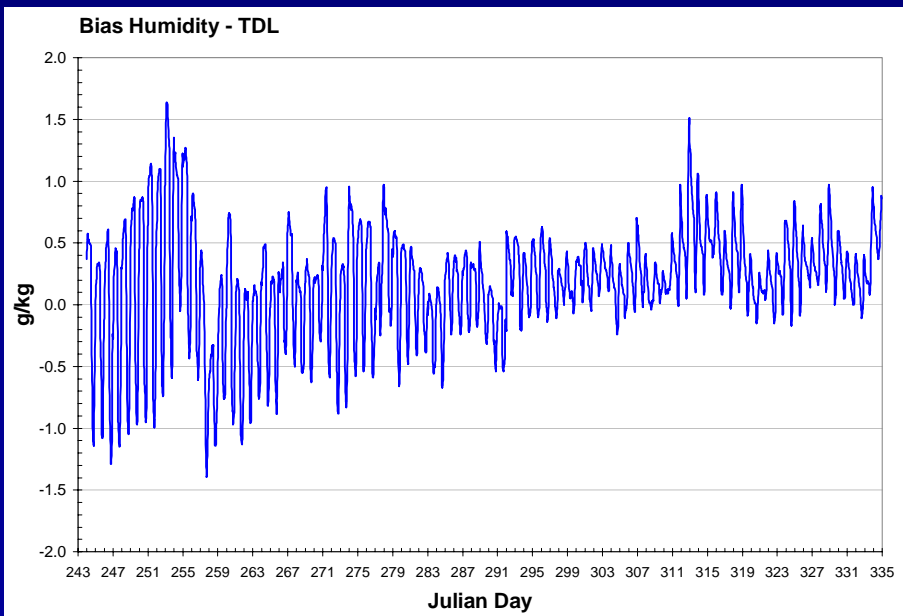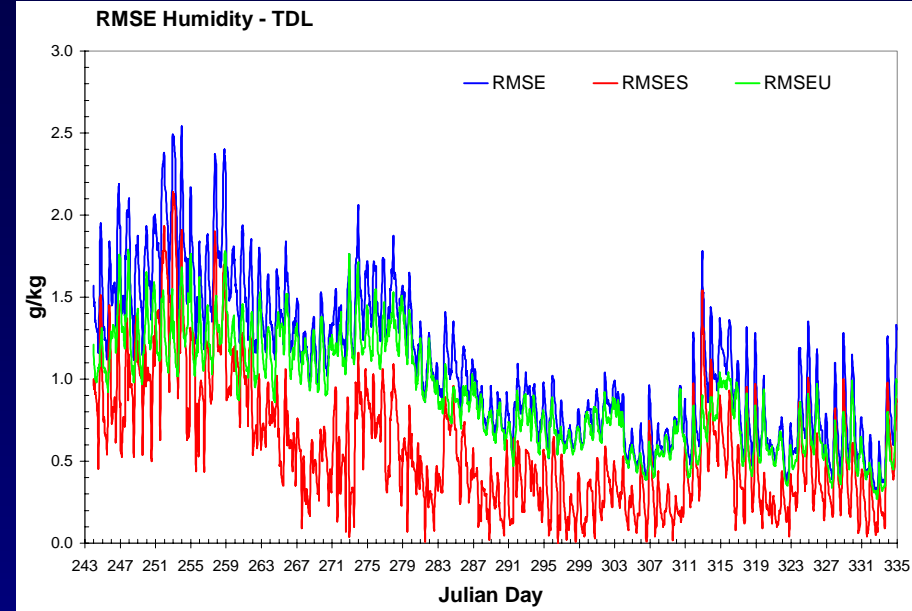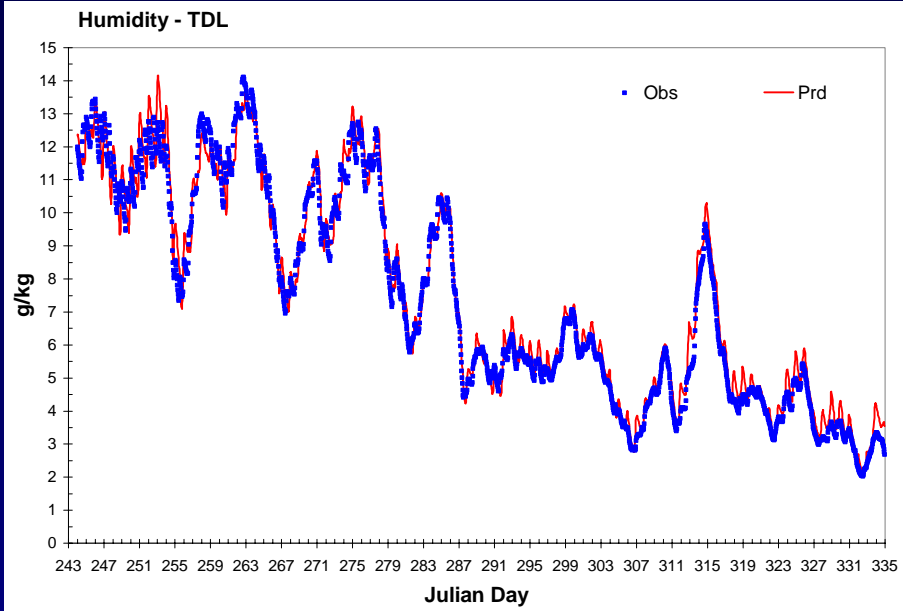
# HUMIDITY

| 2002 | Network | Humidity | | | | | |
|------|---------|----------|------|------|------|------|------|
| | | Bias | | | IOA | | |
| | | Max | Min | Mean | Max | Min | Mean |
| JAN | TDL | -0.24 | -1.54 | 0.45 | 0.99 | 0.60 | 0.89 |
| FEB | TDL | 1.51 | -0.07 | 0.48 | 0.99 | 0.54 | 0.87 |
| MAR | TDL | 1.73 | -0.10 | 0.52 | 0.99 | 0.47 | 0.91 |
| APR | TDL | 3.48 | -0.82 | 0.52 | 0.99 | 0.44 | 0.91 |
| MAY | TDL | 0.92 | -1.67 | -0.02 | 0.99 | 0.48 | 0.91 |
| JUN | TDL | 1.00 | -2.27 | -0.33 | 0.98 | 0.67 | 0.88 |
| JUL | TDL | 0.87 | -2.32 | -0.55 | 0.97 | 0.57 | 0.86 |
| AUG | TDL | 0.92 | -2.17 | -0.23 | 0.97 | 0.58 | 0.86 |
| SEP | TDL | 1.64 | -1.39 | 0.03 | 0.98 | 0.66 | 0.91 |
| OCT | TDL | 0.97 | -0.67 | 0.15 | 0.99 | 0.80 | 0.96 |
| NOV | TDL | 1.51 | -0.17 | 0.34 | 0.99 | 0.56 | 0.92 |
| DEC | TDL | 0.95 | -0.17 | 0.34 | 0.99 | 0.54 | 0.91 |

- MM5 captures general trend of humidity change
- MM5 tends to overestimate humidity in Winter, Spring, and Fall, but underestimate humidity in 5 month Summer
- MM5 often shows larger diurnal variations than observation
- Unsystematic RMSE dominates RMSE
- MM5 shows good IOA (~0.9) all year

NESCAUM

# Numerical Experimental Analysis Data for the Year of 2002

Da-Lin Zhang and Shunli Zhang
Department of Atmospheric and Oceanic Science, University of Maryland
College Park, MD 20742
Tel. (301) 405-2018; Email: dalin@atmos.umd.edu

## 1. Introduction

A total of 128 numerical experiments, in 3-day segments, for the year of 2002 (i.e., from 0000 UTC 14 December 2001 to 0000 UTC 1 January 2003) have been conducted on our newly purchased Cluster using the nested-grid (36/12 km) Version 3.6 of the PSU/NCAR mesoscale model (i.e., MM5). The NCEP's Eta analysis with 40-km resolution was used to initialize the model integrations and specify the outmost lateral boundary conditions. To minimize the influence of model errors but retain as many mesoscale circulations as possible, the dynamical nudging or four-dimensional data assimilation (FDDA) technique was adopted to include observations of the surface winds and upper-level meteorological information. More attention was paid to the accuracy of surface winds due to their important roles in ozone transport. The model integrations were re-initialized every 3.5 days, allowing a 12-h period for the model spin-up (i.e., the first 12-h data could be truncated in the application of the datasets). Hourly model outputs were archived for the period of 12.5 months. This four-dimensional high resolution (in time and space) analysis dataset so assimilated was generated for air quality modeling and for regional haze studies. These integrations yielded a total of 830 Gbytes analysis data.

## 2. Model description

The Version 3.6 of MM5 with a Lambert conformal map projection, an MPP Version developed for clusters, was used for this project. The (x, y) dimensions of the coarse (36 km) and fine (12 km) mesh domains are 149 x 129 and 175 x 175, respectively. The vertical discretion uses terrain-following $\sigma$-coordinates, but the pressure at the $\sigma$-levels are determined from a reference state that is estimated using the hydrostatic equation from a given sea-level pressure and temperature with a standard lapse rate. There are 30 uneven $\sigma$ levels, giving 29 layers, with higher resolution in the planetary boundary layer (PBL). The $\sigma$ levels are placed at the following values:

1.000, 0.9974, 0.994, 0.989, 0.9820, 0.972, 0.959, 0.943, 0.923, 0.8990, 0.871, 0.839, 0.803, 0.763, 0.718, 0.668, 0.618, 0.568, 0.518, 0.468, 0.418, 0.368, 0.318, 0.268, 0.218, 0.168, 0.123, 0.080, 0.040, 0.00

The surface layer is defined at an altitude of about 10 m, the level at which surface winds are typically observed. The model top is set at 50 hPa with a radiative upper boundary condition. The time steps for the 36 km and 12 km resolution domains are 75 and 25 seconds, respectively.

Figs. 1 and 2 show the nested-grid (36/12 km) domain and the fine-mesh domain, respectively, that were used for this project.

Domain 1 is centered at $40^0$N latitude and $97^0$W longitude with a grid size of 36 km, and it covers the U.S. continents, Mexico, Canada, the Gulf of Mexico, and part of the East Pacific and West Atlantic oceans.

| Fig. 1 The coarse-mesh (36 km) domain. | Fig. 2  The fine-mesh (12-km) domain. |

Domain 2 uses a grid size of 12 km, and it covers the northeastern, central and southeastern US as well as Southeastern Canada.

The important model physics of the MM5 used for this project include:

(i) The latest version of the Kain-Fritsch (1993) convective scheme was used for both 36- and 12-km resolution domains;

(ii) An explicit moisture scheme (without the mixed phase) containing prognostic equations for cloud water (ice) and rainwater (snow) (Dudhia 1989; Zhang 1989);

(iii) A modified version of the Blackadar planetary boundary layer (PBL) scheme (Zhang and Anthes 1982; Zhang and Zheng 2004);

(iv) A simple radiative cooling scheme (Grell et al. 1997);

(v) A multi-layer soil model to predict land surface temperatures using the surface energy budget equation (Dudhia 1996).

Note that the Blackadar PBL scheme has been modified in order to reproduce the diurnal cycles of surface winds and temperatures, after performing a comparative study of the following five different PBL schemes: the Gayno-Seaman TKE scheme (Shafran et al. 2000), Burk-Thompson (1989), Blackadar (Zhang and Anthes 1982), MRF (Hong and Pan 1996), and Miller-Yamada-Jajić (Miller and Yamada 1974; Jajić 1990, 1994). These changes are given as follows (see Zhang and Zheng 2004 for more detail):

• K-coefficient is determined by the Richardson number according to Zhang and Anthes (1982), where the critical Richardson number is set to be 0.25. In addition, the mixing length is set to be the thickness of the model layer.

• Use of potential temperature rather than virtual potential temperature to calculate the bulk Richardson number Rb.

**3. Nudging Processes**

The MM5 provides options for nudging observations for each domain during the course of model integration (Stauffer and Seaman 1990; Stauffer et al. 1991). The Eta

analyses of upper-air winds, temperature and water-vapor mixing ratio as well as their associated surface fields, were nudged every 6 hours, and the higher-resolution surface wind field was nudged every 3 hours. While only the surface winds were nudged, their influences could be extended into the PBL (see Stauffer et al. 1991).

Based on our previous experience with many numerical experiments, the following nudging coefficients have been used:

- Upper-air wind fields: 5.0E-4 for Domain 1, and 2.5E-4 for Domain 2;
- Upper-air temperature fields: 1.0E-5 for both Domains;
- Surface winds: 5.0E-4 for Domain 1, and 2.5E-4 for Domain 2; and
- Surface temperature and moisture: not nudged due to instability consideration.

## 4. Model initialization

The model is initialized with NCEP's Eta model analysis (ds609.2) as a first guess that is then enhanced by observations at upper levels and the surface.

(i) NCEP's ADP global upper-air observations (NCAR archive ds353.4) are used to further enhance the upper-level Eta analysis.

(ii) The following two sets of surface observations have been introduced into the model initial state to improve the Eta analysis of surface wind fields:

- The NCEP's ADP global surface wind observations (NCAR archive ds464.0): This dataset provides 6-hourly surface observations over land (i.e., at 0000, 0600, 1200, 1800 UTC) in one stream, and 3-hourly (i.e., at 0300, 0900, 1500, 2100 UTC) over both land and ocean surfaces in another stream.
- The TDL's U.S. and Canadian surface observations (NCAR archive ds472.0): This dataset provides hourly surface observations over the U.S. and Canadian regions.

The Eta model analysis has a domain covering the entire U.S. continents with a 40-km horizontal resolution. It includes the following types of observations:

- Rawinsonde mass and wind;
- Piball winds;
- Dropwindsondes;
- Wind profiles;
- Surface land temperature and moisture;
- Oceanic surface data (ship and buoys);
- Aircraft winds;
- Satellite cloud-drift winds;
- Oceanic TOVS thickness retrievals;
- GOES and SSM/I precipitable water retrievals.

The Cressman objective analysis option was used to enhance the Eta analysis. However, we analyzed the results and found that it still could not reproduce the right diurnal cycle of surface winds and temperatures. Thus, we repeated the Cressman procedures three more times to enhance the surface analyses. Results indicate that this procedure significantly improved the results.

Note that (i) because of the initial model spin-up, we recommend that the first 12-h model integration of each run be discarded; and (ii) because the synoptic-scale upper-air winds and temperatures were nudged, the flow fields above the PBL might contain less smaller-scale features (e.g., in low-level jets, mountain-forced perturbations and etc.).

## 5. Data Archive

As mentioned above, we have conducted a total of 128 experiments, in 3-day segments, from 0000 UTC 14 December 2001 to 0000 UTC 1 January 2003. The following table lists the experiments and their corresponding integration periods:

| Exp. # | Period | Exp. # | Period |
|---|---|---|---|
| 1 | 00/15/12-00/18/12*01 | 2 | 00/18/12-12/21/12*01 |
| 3 | 00/21/12-00/24/12*01 | 4 | 00/24/12-00/27/12*01 |
| 5 | 00/27/12-00/30/12*01 | 6 | 00/30/12-00/02/01*02 |
| 7 | 00/02/01-00/05/01*02 | 8 | 00/05/01-00/08/01*02 |
| 9 | 00/08/01-00/11/01*02 | 10 | 00/11/01-00/14/01*02 |
| 11 | 00/14/01-00/17/01*02 | 12 | 00/17/01-00/20/01*02 |
| 13 | 00/20/01-00/23/01*02 | 14 | 00/23/01-00/26/01*02 |
| 15 | 00/26/01-00/29/01*02 | 16 | 00/29/01-00/01/02*02 |
| 17 | 00/01/02-00/04/02*02 | 18 | 00/04/02-00/07/02*02 |
| Exp. # | Period | Exp. # | Period |
| 19 | 00/07/02-00/10/02*02 | 20 | 00/10/02-00/13/02*02 |
| 21 | 00/13/02-00/16/02*02 | 22 | 00/16/02-00/19/02*02 |
| 23 | 00/19/02-00/22/02*02 | 24 | 00/22/02-00/25/02*02 |
| 25 | 00/25/02-00/28/02*02 | 26 | 00/28/02-00/03/03*02 |
| 27 | 00/03/03-00/06/03*02 | 28 | 00/06/03-00/09/03*02 |
| 29 | 00/09/03-00/12/03*02 | 30 | 00/12/03-00/15/03*02 |
| 31 | 00/15/03-00/18/03*02 | 32 | 00/18/03-00/21/03*02 |
| 33 | 00/21/03-00/24/03*02 | 34 | 00/24/03-00/27/03*02 |
| 35 | 00/27/03-00/30/03*02 | 36 | 00/30/03-00/02/04*02 |
| 37 | 00/02/04-00/05/04*02 | 38 | 00/05/04-00/08/04*02 |
| 39 | 00/08/04-00/11/04*02 | 40 | 00/11/04-00/14/04*02 |
| 41 | 00/14/04-00/17/04*02 | 42 | 00/17/04-00/20/04*02 |
| 43 | 00/20/04-00/23/04*02 | 44 | 00/23/04-00/26/04*02 |
| 45 | 00/26/04-00/29/04*02 | 46 | 00/29/04-00/02/05*02 |
| 47 | 00/01/05-00/04/05*02 | 48 | 00/04/05-00/07/05*02 |
| 49 | 00/07/05-00/10/05*02 | 50 | 00/10/05-00/13/05*02 |
| 51 | 00/13/05-00/16/05*02 | 52 | 00/16/05-00/19/05*02 |
| 53 | 00/19/05-00/22/05*02 | 54 | 00/22/05-00/25/05*02 |
| 55 | 00/25/05-00/28/05*02 | 56 | 00/28/05-00/31/05*02 |
| 57 | 00/31/05-00/03/06*02 | 58 | 00/03/06-00/06/06*02 |
| 59 | 00/06/06-00/09/06*02 | 60 | 00/09/06-00/12/06*02 |
| 61 | 00/12/06-00/15/06*02 | 62 | 00/15/06-00/18/06*02 |
| 63 | 00/18/06-00/21/06*02 | 64 | 00/21/06-00/24/06*02 |
| 65 | 00/24/06-00/27/06*02 | 66 | 00/27/06-00/30/06*02 |

| | | | |
|---|---|---|---|
| 67 | 00/30/06-00/03/07*02 | 68 | 00/03/07-00/06/07*02 |
| 69 | 00/06/07-00/09/07*02 | 70 | 00/09/07-00/12/07*02 |
| 71 | 00/12/07-00/15/07*02 | 72 | 00/15/07-00/18/07*02 |
| 73 | 00/18/07-00/21/07*02 | 74 | 00/21/07-00/24/07*02 |
| 75 | 00/24/07-00/27/07*02 | 76 | 00/27/07-00/30/07*02 |
| 77 | 00/30/07-00/02/08*02 | 78 | 00/02/08-00/05/08*02 |
| 79 | 00/05/08-00/08/08*02 | 80 | 00/08/08-00/11/08*02 |
| 81 | 00/11/08-00/14/08*02 | 82 | 00/14/08-00/17/08*02 |
| 83 | 00/17/08-00/20/08*02 | 84 | 00/20/08-00/23/08*02 |
| 85 | 00/23/08-00/26/08*02 | 86 | 00/26/08-00/29/08*02 |
| 87 | 00/29/08-00/01/09*02 | 88 | 00/01/08-00/04/09*02 |
| 89 | 00/04/09-00/07/09*02 | 90 | 00/07/09-00/10/09*02 |
| 91 | 00/10/09-00/13/09*02 | 92 | 00/13/09-00/16/09*02 |
| 93 | 00/16/09-00/19/09*02 | 94 | 00/19/09-00/22/09*02 |
| 95 | 00/22/09-00/25/09*02 | 96 | 00/25/09-00/28/09*02 |
| 97 | 00/28/09-00/01/10*02 | 98 | 00/01/10-00/04/10*02 |
| 99 | 00/04/10-00/07/10*02 | 100 | 00/07/10-00/10/10*02 |
| 101 | 00/10/10-00/13/10*02 | 102 | 00/13/10-00/16/10*02 |
| 103 | 00/16/10-00/19/10*02 | 104 | 00/19/10-00/22/10*02 |

| Exp. # | Period | Exp. # | Period |
|---|---|---|---|
| 105 | 00/22/10-00/25/10*02 | 106 | 00/25/10-00/28/10*02 |
| 107 | 00/28/10-00/31/10*02 | 108 | 00/31/10-00/03/11*02 |
| 109 | 00/03/11-00/06/11*02 | 110 | 00/06/11-00/09/11*02 |
| 111 | 00/09/11-00/12/11*02 | 112 | 00/12/11-00/15/11*02 |
| 113 | 00/15/11-00/18/11*02 | 114 | 00/18/11-00/21/11*02 |
| 115 | 00/21/11-00/24/11*02 | 116 | 00/24/11-00/27/11*02 |
| 117 | 00/27/11-00/30/11*02 | 118 | 00/30/11-00/03/12*02 |
| 119 | 00/03/12-00/06/12*02 | 120 | 00/06/12-00/09/12*02 |
| 121 | 00/09/12-00/12/12*02 | 122 | 00/12/12-00/15/12*02 |
| 123 | 00/15/12-00/18/12*02 | 124 | 00/18/12-00/21/12*02 |
| 125 | 00/21/12-00/24/12*02 | 126 | 00/24/12-00/27/12*02 |
| 127 | 00/27/12-00/30/12*02 | 128 | 00/30/12-00/02/01*03 |

The datasets listed above include the MM5 outputs from Domain 1 (36 km) and Domain 2 (12 km), the analysis data used for FDDA, and initial and lateral boundary conditions. If necessary, any of the experiments listed above could be re-run. The MM5 outputs include the three-dimensional fields of temperature, horizontal winds, vertical motion, pressure perturbations, moisture, cloud water/rain water/ice water/snow water mixing ratio, and radiation tendency; and the two-dimensional fields of the map-scale factor, longitude and latitude, Coriolis parameter, land use category, terrain height, PBL depth, accumulated convective/non-convective precipitation, surface sensible/latent heat flux. A FORTRAN program to read the datasets has also been included.

## 6. Acknowledgments

## References

Burk, S. D., and W. T. Thompson, 1989: A vertically nested regional numerical weather prediction model with second-order closure physics. *Mon. Wea. Rev.,* **117,** 2305–2324.

Dudhia, J., 1989: Numerical study of convection observed during the winter monsoon experiments using a mesoscale two-dimensional model. *J. Atmos. Sci.,* **46,** 3077–3107.

Grell, G. A., J. Dudhia, and D. R. Stauffer, 1995: A description of the fifth-generation Penn State/NCAR Mesoscale Model (MM5). NCAR Tech. Note NCAR/TN-398 1 STR, 122 pp.

Hong, S.-H., and H.-L. Pan, 1996: Nonlocal boundary layer vertical diffusion in a medium-range forecast model. *Mon. Wea. Rev.,* **124,** 2322–2339.

Jajić, Z. I., 1990: The step-mountain coordinate: Physical package. *Mon. Wea. Rev.,* **118,** 1429-1443.

——, 1994: The step-mountain Eta coordinate model: Further development of the convection, viscous sublayer and turbulent closure schemes. *Mon. Wea. Rev.,* **122,** 927-945.

Kain, J.S., and J.M. Fritsch, 1993: Convective parameterization for mesoscale models: The Kain-Fritsch scheme. Cumulus Parameterization. *Meteor. Monogr.*, **46**, Amer. Meteor. Soc., 165-170.

Mellor, G. L., and T. Yamada, 1974: A hierarchy of turbulence closure models for planetary boundary layers. *J. Atmos. Sci.,* **31,** 1791–1806.

Shafran, P.C., N.L. Seaman, and G.A. Gayno, 2000: Evaluation of numerical predictions of boundary layer structure during the Lake Michigan ozone study. *J. Appl. Meteor.,* **39,** 412-426.

Stauffer, D. R., N. L. Seaman and F. S. Binkowski, 1991: Use of four-dimensional data assimilation in a limited-area mesoscale model. Part II: Effects of data assimilation within the planetary boundary layer. *Mon. Wea. Rev*., **119**, 734-754.

Stauffer, D. R. and N. L. Seaman, 1990: Use of four-dimensional data assimilation in a limited-area mesoscale model. Part I: Experiments with synoptic-scale data. *Mon. Wea. Rev*., **118**, 1250-1277.

Zhang, D.-L., 1989: The effect of parameterized ice microphysics on the simulation of vortex circulation with a mesoscale hydrostatic model. *Tellus*, **41A**, 132-147.

——, and R. A. Anthes, 1982: A high-resolution model of the planetary boundary layer—Sensitivity tests and comparisons with SESAME-79 data. *J. Appl. Meteor.,* **21,** 1594–1609.

——, and W.-Z. Zheng, 2004: Diurnal cycles of surface winds and temperatures as simulated by five boundary-layer parameterizations. *J. Appl. Meteor.,* **43**, 157-169.

# Diurnal Cycles of Surface Winds and Temperatures as Simulated by Five Boundary Layer Parameterizations

DA-LIN ZHANG AND WEI-ZHONG ZHENG

*Department of Meteorology, University of Maryland at College Park, College Park, Maryland*

## ABSTRACT

Although most of the planetary boundary layer (PBL) parameterizations have demonstrated the capability to reproduce many meteorological phenomena in the lowest few kilometers, little attention has been paid to the prediction of the diurnal cycles of surface wind speed ($V_{SFC}$) in relation to surface temperature ($T_{SFC}$). In this study, the performance of five widely used PBL parameterizations in reproducing the diurnal cycles of $V_{SFC}$ and $T_{SFC}$ is evaluated using the 3-day mesoscale simulations of summertime weak-gradient flows over the central United States where little organized convection and topographical forcing were present. The time series of area-averaged $V_{SFC}$ and $T_{SFC}$, as well as the vertical wind and thermal profiles from the five sensitivity simulations, are compared with hourly surface observations and other available data. The hourly surface observations reveal that the diurnal cycles of $V_{SFC}$ are in phase (but surface wind directions are 5–6 h out of phase) with those of $T_{SFC}$. It is shown that both $V_{SFC}$ and $T_{SFC}$ are very sensitive to the PBL parameterizations, given the identical conditions for all of the other model parameters. It is found that all five of the PBL schemes can reproduce the diurnal phases of $T_{SFC}$ (and wind directions), albeit with different amplitudes. However, all of the schemes underestimate the strength of $V_{SFC}$ during the daytime, and most of them overestimate it at night. Moreover, some PBL schemes produce pronounced phase errors in $V_{SFC}$ or substantially weak $V_{SFC}$ all of the time, despite their well-simulated diurnal cycle of $T_{SFC}$. The results indicate that a perfect simulation of the diurnal $T_{SFC}$ cycle (and the thermal structures above) does not guarantee the reproduction of the diurnal cycles of $V_{SFC}$. The final outcome would depend on how various physical processes, such as the vertical turbulent exchanges of the mass and momentum under different stability conditions, are parameterized. Because the upper portion of the PBL flow is often nearly opposite in phase to $V_{SFC}$ under weak-gradient conditions, the results have significant implications for the predictability of diurnal precipitation and the studies of air quality, wind energy, and other environmental problems.

## 1. Introduction

The planetary boundary layer (PBL) over land generally undergoes significant diurnal cycles,[1] especially on calm, clear-sky days. The daytime PBL begins when the net surface heat flux is directed upward after sunrise. As more solar energy is absorbed by the earth's surface, free convective eddies become active in transporting sensible heat (moisture) upward to warm (moisten) the air above and momentum downward to accelerate the flow below. Meanwhile, the rising eddies, with their roots in the surface layer, penetrate into the capped inversion and mix heat, moisture, and kinetic energy with their environments—a countergradient heat transport

---

[1] The diurnal cycle of the PBL used to be viewed in terms of surface radiative forcing and low-level temperature variations. In this study, it also includes the surface winds and the winds above in the PBL.

*Corresponding author address:* Dr. Da-Lin Zhang, Department of Meteorology, University of Maryland at College Park, College Park, MD 20742-2425.
E-mail: dalin@atmos.umd.edu

process referred to as entrainment. The mass and wind fields in this mixed layer adjust quickly to produce a state of slowly evolving equilibrium until the PBL reaches its maximum depth in the late afternoon. Near sunset, rapid radiative heat losses occur at the ground so that a second temperature inversion starts to grow from the bottom surface. As a result, horizontal winds above the surface layer begin to decouple from the surface friction, sometimes leading to the formation of a nocturnal low-level jet (LLJ) near the top of the nocturnal inversion layer (Blackadar 1957).

During the past 30–40 yr, considerable progress has been made in the development and improvement of the PBL parameterizations (e.g., Mellor and Yamada 1974; Blackadar 1976, 1979; Zhang and Anthes 1982; Burk and Thompson 1989; Janjić 1994; Hong and Pan 1996) and land surface parameterizations (Xue et al. 1991; Chen and Dudhia 2001) in order to obtain realistically the above-mentioned flow properties in the PBL and the collective effects of the PBL on the free atmospheric circulation with numerical weather prediction (NWP) and climate models. For example, one-dimensional (1D)

PBL schemes have advanced from the early first-order, local $K$ theory to 1.5-order and higher-order turbulent kinetic energy (TKE) closures, and 3D atmospheric models have progressed from the bulk, mixed-layer treatment to higher resolution and to the large-eddy-simulation models (Holt and Raman 1988; Moeng 1984). Because the PBL behaves differently in unstable and stable stratifications, various nonlocal closures have been developed to treat the daytime PBL development (e.g., see the appendix). However, most of the previous 3D modeling studies focused on the diurnal cycles of surface temperature ($T_{SFC}$) and the spatial structures of the mass and wind fields in the PBL in relation to clouds and precipitation (Burk and Thompson 1989; Hong and Pan 1996; Braun and Tao 2000). Little attention has been paid to the model's capability to capture the diurnal cycles of surface and PBL winds. This omission is due partly to some uncertainties in parameterizing the vertical momentum transport and pressure diffusion in the PBL and partly to the misconception that the convective development is associated more with the vertical transport of sensible and latent heat fluxes than with momentum fluxes. Sometimes the PBL winds (and divergence) are considered simply as a dynamical response to the thermal gradient generated by differential (radiative) heating or cooling (e.g., sea breezes). For the convenience of subsequent discussions, we will hereinafter distinguish the surface wind speed ($V_{SFC}$) from the wind speed above in the PBL ($V_{PBL}$).

Similarly, only a limited number of observational studies have been performed to examine the diurnal variations of $V_{SFC}$ and $V_{PBL}$ over tropical islands (Aspliden 1977), open oceans (Deser 1994), and coastal and mountainous regions (Hering and Borden 1962; Reiter and Tang 1984; Savijarvi 1997). These earlier studies related the diurnal wind changes to the atmospheric tidal variations in surface pressure and to differential solar heating associated with topography, land–water contrasts, and cloudiness. Based on 3-hourly global observations of $V_{SFC}$ during 1976–97, Dai and Deser (1999) suggested that diurnal variations of $V_{SFC}$ are caused by diurnal changes in vertical momentum fluxes and surface pressure tides. They found that (a) the diurnal harmonics of continental $V_{SFC}$ are approximately in phase with those of $T_{SFC}$ and (b) the mean daily variations of surface divergence are closely related to those of $V_{SFC}$. In another study, Dai et al. (1999) observed significant diurnal anomalies of precipitation during the summer months over the contiguous United States, which were also supported by the radar-based climatological description of warm-season precipitation episodes by Carbone et al. (2002). This observation led Dai et al. (1999) to suggest that the diurnal variations of divergence could be a major factor controlling the timing of summer convective precipitation. To test this hypothesis, they examined the sensitivity of the model-simulated precipitation in the summer of 1993 to several convective parameterizations. They found that the regional climate

simulations tend to produce too much cloudiness, thereby reducing surface solar radiation and weakening the subsequent development of the PBL, including $V_{SFC}$ and $V_{PBL}$. As a consequence, the simulations overestimate precipitation frequency and underestimate precipitation intensity as compared with the observations. Because of the pronounced convective forcing and its nonlinear interaction with other physical processes, it was not possible to identify the parameters that influence the simulated diurnal variations of $V_{SFC}$ and $V_{PBL}$.

It is obvious that obtaining realistic diurnal cycles of $V_{SFC}$ and $V_{PBL}$ is important, not only for NWP and climate research, but also for studies of air quality, wind energy, visibility (haze, fog, and low clouds), engineering (construction), and other environment-related problems. However, it still remains unclear to what extent such diurnal cycles could be reasonably reproduced by current numerical models despite the above-mentioned advances in PBL modeling. This issue could be addressed by testing the performance of various PBL parameterizations that are being used in today's numerical models.

Therefore, we are motivated to conduct a comparative numerical modeling study of limited-area boundary layer flows with five widely used PBL parameterization schemes in the fifth-generation Pennsylvania State University (PSU)–National Center for Atmospheric Research (NCAR) Mesoscale Model (MM5; Dudhia 1993; Grell et al. 1995). To minimize the impact of deep convection, land–water contrast, and topography on the diurnal cycles of $V_{SFC}$ and $V_{PBL}$, a 72-h dry period (i.e., from 1200 UTC 12 July to 1200 UTC 15 July 1997) of weak-gradient atmospheric flows over the central United States is selected for this study. Although the land surface processes may contribute to the development of the PBL through vertical fluxes of heat, moisture, and momentum in the surface layer, they generally play a role in determining the amplitude, rather than the phase, of the diurnal variations of $T_{SFC}$ and $V_{SFC}$ as compared with the other PBL processes.

The next section provides a brief description of the case study and shows the observational evidence of the diurnal cycles of $V_{SFC}$ in relation to $T_{SFC}$. Section 3 outlines the basic physical options used for the MM5 simulations, and the appendix presents the major characteristics of the five PBL parameterization schemes being tested in the study. Section 4 compares the diurnal cycles of $V_{SFC}$ simulated with the five different PBL schemes with the observed cycle. The simulated vertical PBL structures will also be studied in relation to the diurnal variations of $V_{SFC}$ and $T_{SFC}$. A summary and concluding remarks are given in the final section.

## 2. Observational evidence

Figure 1 shows the distribution of 3-day-averaged geopotential height and temperature at 850 hPa during the period of 12–15 July 1997. The large-scale flow
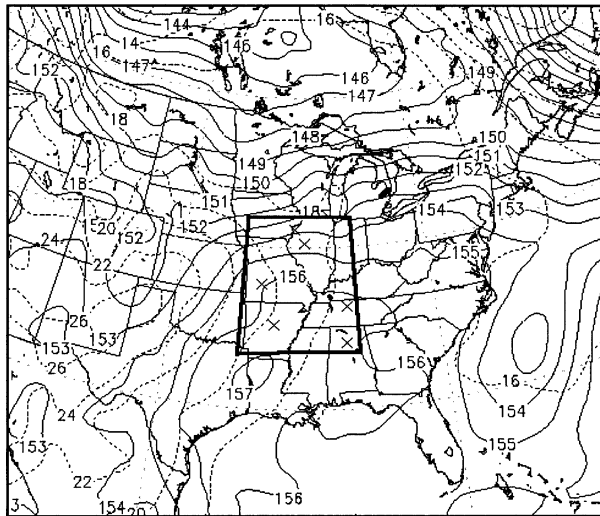
FIG. 1. Distribution of geopotential heights (solid) at intervals of 10 m and temperatures (dashed) at intervals of 2°C at 850 hPa that are obtained by averaging the 6-hourly Eta-Model analyses during the period of 1200 UTC 12 Jul–1200 UTC 15 Jul 1997. The inner domain denotes an area of 9° lat × 9° lon (i.e., 33°–42°N, 86°–95°W) that is used to obtain the averaged surface and PBL fields shown in all the subsequent figures. The × symbol shown within the inner mesh indicates the locations of available upper-air observations used for verification in Fig. 7.

over the area of interest, that is, the central United States, was dominated by a subtropical high pressure system over the southern states, with a weak-gradient westerly flow to the north. A topographically generated warm tongue with pronounced thermal gradients extended from the Rocky Mountains into the western portion of the central United States. However, these thermal gradients diminished rapidly with height and became insignificant at 700 hPa and above (not shown). Few significant disturbances passed over the region during the 3-day period (not shown), and so there was little organized convective activity except for a few isolated afternoon convective events. Thus, the weak large-scale flow, little convective influence, and little topographical forcing over the region provide a reasonable test bed to isolate the impact of surface radiative forcing on the diurnal variations of the surface and PBL properties. Nevertheless, Dai and Deser (1999) and others have shown that diurnal variations of $V_{SFC}$ could account for 50%–70% of the total daily variance over land during all seasons.

To reduce the influences of locally generated meteorological disturbances (associated with terrain, inhomogeneities in the land use, etc.) and errors in the observed $V_{SFC}$, it is meaningful and statistically significant to examine the area-averaged properties rather than individual single-station observations; similar logic holds for the model-simulated fields. Thus, all of the observed and simulated data used in this study are spatially averaged over an area of 9° lat × 9° lon in the central U.S. regions (see Fig. 1). The zonal migrating effect of
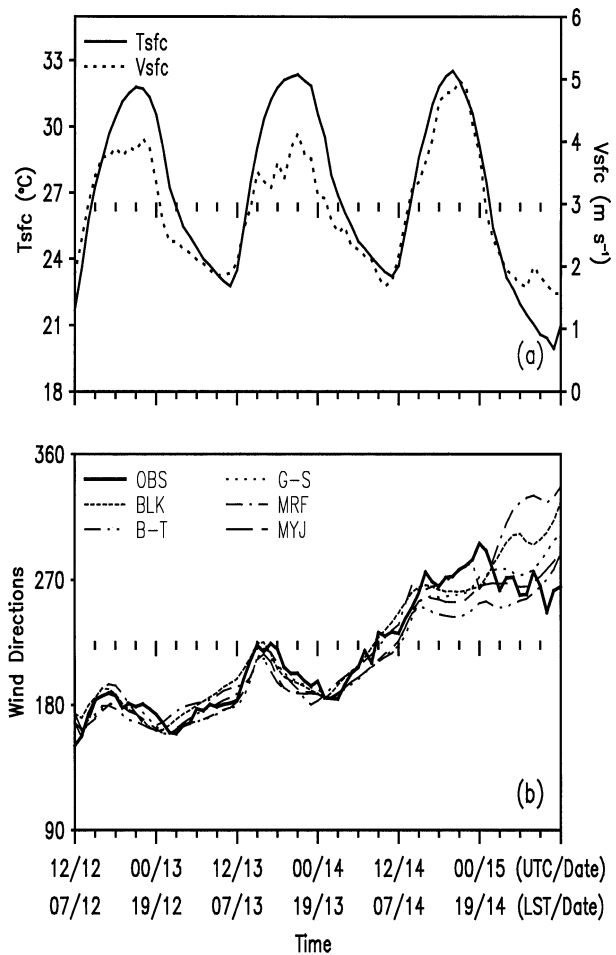


FIG. 2. (a) Diurnal variations of the area-averaged surface temperatures $T_{SFC}$ (°C, solid) and horizontal wind speeds $V_{SFC}$ (m s$^{-1}$, dashed) from the hourly observations over the analysis domain (see Fig. 1) during the 3-day period of 1200 UTC 12 Jul–1200 UTC 15 Jul 1997. (b) As in (a), but for the observed (solid) and the simulated surface wind directions using the BLK (dashed), BT (double dot–dashed), GS (dotted), MRF (dot–dashed), and MYJ (double-dashed) PBL schemes (see section 3 for the related discussion).

solar radiation, which is equivalent to ±18 min, is neglected in generating the time series of the area-averaged surface properties. On average, there were about 105 surface stations over the area that reported hourly temperature, winds, and other meteorological variables; they were extracted from the National Oceanic and Atmospheric Administration (NOAA)'s Technical Development Laboratory U.S. and Canada Surface Hourly Observations archived at NCAR (available online at http://dss.ucar.edu/datasets/ds472.0/).

Figure 2 shows the diurnal variations of the area-averaged hourly $V_{SFC}$ (speed and direction) and $T_{SFC}$ during the 3-day period. Note that, in this study, $V_{SFC}$ and $T_{SFC}$ are defined, following meteorological convention, at the altitudes of 10 and 2 m, respectively. The (nearly sinusoidal) diurnal cycles of $T_{SFC}$ were clearly evident, with the amplitudes varying from the minimums ($T_{MIN}$)

of 20°–23°C at 1100 UTC (or 0600 LST) to the peaks ($T_{MAX}$) of 31°–32°C at 2100 UTC (or 1600 LST) during the 3-day period (Fig. 2a). The continued increases in $T_{MAX}$ and the mean temperature on each day were consistent with the daily progression toward the middle summer. Note that, for each diurnal cycle, $T_{SFC}$ always increased more rapidly during the first 3–5 h of the daytime development because of the existence of shallow PBL depth with increasing energy input and decreased at slower rates as it approached $T_{MIN}$ as a result of the reduced net radiative heat losses.

Of particular relevance for this study is the fact that the diurnal cycles of $V_{SFC}$ were in phase with those of $T_{SFC}$ (Fig. 2a). That is, the strongest surface wind occurred 2–3 h before sunset when the surface air was hottest, whereas the weakest flow occurred near sunrise when the surface layer was coldest. Of significance is that even the trends of changes in wind speed at some periods were similar to those of $T_{SFC}$. This phase relationship is as expected, based on the concept described at the beginning of section 1, assuming that the horizontal winds increase monotonically with height. We may speculate that the amplitude of such diurnal cycles would be greater in the cases of stronger vertical wind shear and deeper PBL developments. Note, however, that the surface wind speeds oscillate, following the rapid acceleration during the early morning hours on the first 2 days. This oscillating feature appears to be attributable to the interaction of the PBL development with the LLJ layers developed in the previous evenings, based on the model simulations to be shown in section 4 (see Fig. 9). It took 4–6 h for the surface-based turbulent eddies to penetrate into the layers above the LLJ layer, before the PBL was fully developed with the strongest $V_{SFC}$. The daytime variations of $V_{SFC}$ on the third day appear to differ from the previous 2 days, indicating that certain changes might have occurred in the free atmosphere; this possibility will be further discussed in section 4 (in relation to Fig. 9). To our knowledge, such diurnal cycles of $V_{SFC}$ have not been previously examined in detail, particularly by numerical modeling studies.

The time series of surface wind direction is given in Fig. 2b, which exhibits a steady directional shift ($>90°$) from the southerly to westerly mean flow associated with the movement of the subtropical high. Of interest is that there also appears to be some diurnal variations (in the range of 0°–30°) in wind direction, but about 5–6 h out of phase with $V_{SFC}$. The momentary peak wind direction coincides closely with the initiation of the above-mentioned $V_{SFC}$ oscillations, suggesting the likely penetration of the surface-based turbulent eddies into the LLJ layer in which the jet flow under inertial oscillation is out of phase with the mean flow above and the frictional flow below. The surface wind direction subsequently becomes more consistent with the mean flow above, as more upper-level momentum is transferred downward. Nevertheless, because the amplitude

of diurnal variations in surface wind direction was much smaller than that of directional changes associated with larger-scale disturbances, we will hereinafter focus only on the diurnal changes of surface wind speed ($V_{SFC}$), unless otherwise mentioned. To minimize the subsequent digression from the focus of this study, Fig. 2b also compares the surface wind directions simulated by five different PBL schemes to those of the observed. It is obvious that all of the PBL schemes reproduce reasonably well the time evolution of the observed surface wind directions, with little difference among them except for the final 6-h simulations.

## 3. Model description

The fundamental features of MM5 used for this study include (i) the simultaneous use of the newest version of the Kain–Fritsch (1993) convective parameterization, which contains the parameterized shallow convective effects (Deng et al. 2003) and an explicit moisture scheme that contains prognostic equations for cloud water (ice) and rainwater (snow) (Hsie et al. 1984; Dudhia 1989; Zhang 1989), (ii) a multilayer soil model to predict land surface temperatures by using the surface energy budget equation, (iii) a simple radiative cooling scheme, and (iv) the specification of the outermost coarse-mesh lateral boundary conditions by linearly interpolating National Centers for Environment Prediction (NCEP) 6-hourly Eta Model analyses at the resolution of 40 km on the Advanced Weather Interactive Processing System 212 grid as in Perkey and Kreitzberg (1976).

The above-mentioned model features are identical for all five of the sensitivity experiments, except for the PBL parameterization schemes and their associated surface flux calculations. The five PBL schemes to be tested are the (i) Blackadar (BLK; Zhang and Anthes 1982), (ii) Gayno–Seaman (GS; Shafran et al. 2000), (iii) Medium-Range Forecasts (MRF; Hong and Pan 1996), (iv) Miller–Yamada–Janjić (MYJ; Janjić 1994), and (v) Burke and Thompson (1989; BT) parameterizations. These PBL schemes are currently being used in MM5, NCEP's operational MRF and NWP models, and the U.S. Navy's Coupled Ocean–Atmosphere Mesoscale Prediction System. As described in the appendix, all of the schemes contain nonlocal treatments of the unstable PBL developments, which include TKE closures (e.g., GS, MYJ, BT), countergradient heat fluxes (MRF), and a buoyant plume model with roots in the surface layer (i.e., BLK).

The model domain has $(x, y)$ dimensions of 123 × 109 with a uniform spacing of 36 km. A total of 26 $\sigma$ levels in the vertical direction are used, with the model top at 50 hPa. These full $\sigma$ levels are 0.0, 0.025, 0.075, 0.125, 0.175, 0.225, 0.275, 0.325, 0.375, 0.425, 0.475, 0.525, 0.575, 0.625, 0.675, 0.725, 0.770, 0.815, 0.860, 0.900, 0.935, 0.96, 0.98, 0.99, 0.9974, and 1, which give 25 half-$\sigma$ layers. The height of the lowest model
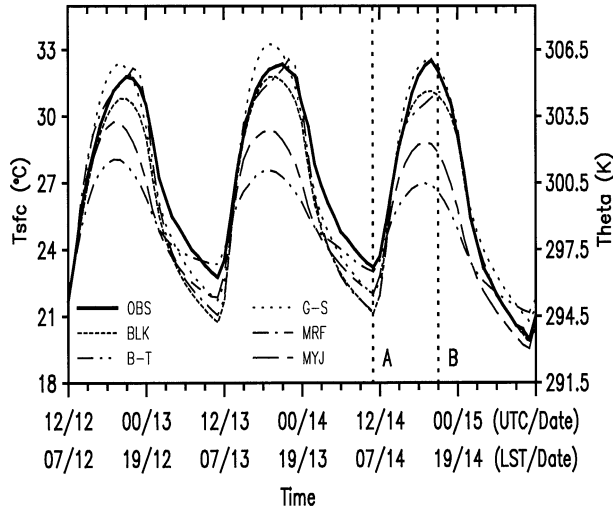
FIG. 3. Comparison of the diurnal variations of the area-averaged $T_{SFC}$ (°C) and potential temperature ($\theta_{SFC}$, K) between the observations (solid) and the model simulations using the BLK, BT, GS, MRF, and MYJ PBL schemes during the 3-day period of 1200 UTC 12 Jul–1200 UTC 15 Jul 1997. The vertical dotted lines denoted by A and B are provided to help to understand the relationship between $\theta_{SFC}$ and the vertical $\theta$ profiles shown in Figs. 4a and 4b, respectively.

layer, at which all of the surface variables except vertical velocity are defined, is about 10 m in order to be comparable with the altimeter-level observations of $V_{SFC}$. To facilitate the $T_{SFC}$ comparisons, the model-simulated $T_{SFC}$ at the altitude of 2 m is diagnosed from the ground temperature ($T_G$) and the surface temperature in the lowest model ($z = 10$ m) layer ($T_A$), namely, $T_{SFC} = 0.45T_G + 0.55T_A$. All sensitivity simulations are initialized at 1200 UTC 12 July 1997 with NCEP's Eta Model analysis as a first guess, which is then enhanced by upper-air and surface observations. They are integrated for 72 h, ending at 1200 UTC 15 July 1997. Hourly model outputs are used to show the time evolution of various surface and PBL features.

## 4. Numerical sensitivity simulations

In this section, we examine to what extent the observed diurnal cycles of $V_{SFC}$, described in section 2, could be reproduced by the above-mentioned five different PBL schemes. First, it is desirable to examine how well the five PBL schemes can reproduce the diurnal cycles of $T_{SFC}$ because of its strong correlation with those of $V_{SFC}$ (see Fig. 2a). It is evident from Fig. 3 that all five of the schemes reproduce the diurnal phases of $T_{SFC}$, including the characteristic time rates of change during the different stages of the PBL development as discussed in section 2. It is clear that this phase reproduction results from the dominant radiative cycle in the surface energy budget. However, the amplitudes of the simulated diurnal cycles of $T_{SFC}$ differ significantly from those of the observed, for example, from 2.5°C at $T_{MIN}$ to 4.5°C at $T_{MAX}$ because of the

different treatments of the surface fluxes of sensible and latent heat and of the energy exchange with the air above in the five PBL schemes.

It is obvious that almost all of the PBL schemes underestimate the magnitude of $T_{MIN}$, albeit to different degrees, and the two similar schemes (i.e., MYJ and BT, see the appendix) underestimate markedly the magnitudes of $T_{MAX}$. The MYJ and BT schemes also generate similar vertical profiles of the potential temperature $\theta$ during both the daytime and nocturnal periods (see Figs. 4a,b). Like $T_{SFC}$, their mixed layers are colder and shallower than those generated by the other three schemes (Fig. 4b), due partly to less upward transfer of the net surface heat flux and partly to underestimation of the countergradient heat flux from the capped inversion (D. Stauffer 2003, personal communication). In fact, the BT scheme tends to transfer more surface moisture upward, according to Braun and Tao (2000), thus causing more evaporative cooling and explaining the weakest amplitude in the diurnal cycles of $T_{SFC}$. In a similar way, the air in the lowest 1 km remains colder than that in the other three schemes during the nocturnal period (Fig. 4a). The two schemes also appear to be more efficient in transferring the sensible heat flux downward under the stable conditions, as indicated by the linear-shaped $\theta$ profiles in the lowest 1.5 km.

In contrast, the GS, MRF, and BLK schemes reproduce better the observed time series of $T_{SFC}$, in that order. This result could be attributed partly to the use of nearly identical surface flux ($\theta$ and water vapor $q$) representations between the MRF and BLK (and GS) schemes [see appendix B in Braun and Tao (2000)]. Of interest is that, despite the use of different closures, their daytime and nocturnal PBL structures are also similar to each other (Figs. 4a,b). Moreover, the lowest 500-m layers produced by the three schemes at $T_{MIN}$ are more statically stable than those of the BT and MYJ schemes (see Fig. 4a).

Despite the above-mentioned considerably different results among the five PBL schemes, the amplitudes in the diurnal cycles of $T_{SFC}$ and the PBL warmth are of little concern in this study of the diurnal cycles of $V_{SFC}$ because all of the surface parameters in the BT, MYJ, and MRF schemes that determine the energy input into the atmosphere above were "tuned" along with their "mother" models and PBL schemes. In other words, some parameters should have been tuned when their associated PBL schemes were incorporated into MM5. In fact, as will be seen in the next paragraph, a higher $T_{SFC}$ or a deeper PBL does not always imply the generation of a stronger $V_{SFC}$ in some PBL schemes. At issue here is to what extent the different PBL schemes can reproduce the strong correlation between $V_{SFC}$ and $T_{SFC}$ that is shown in Fig. 2, given the realistic diurnal radiative cycle at the earth's surface.

A comparison of the simulated diurnal cycles of $V_{SFC}$ with the observed cycles (Fig. 5) shows that all of the PBL schemes underestimate the observed $V_{SFC}$ during
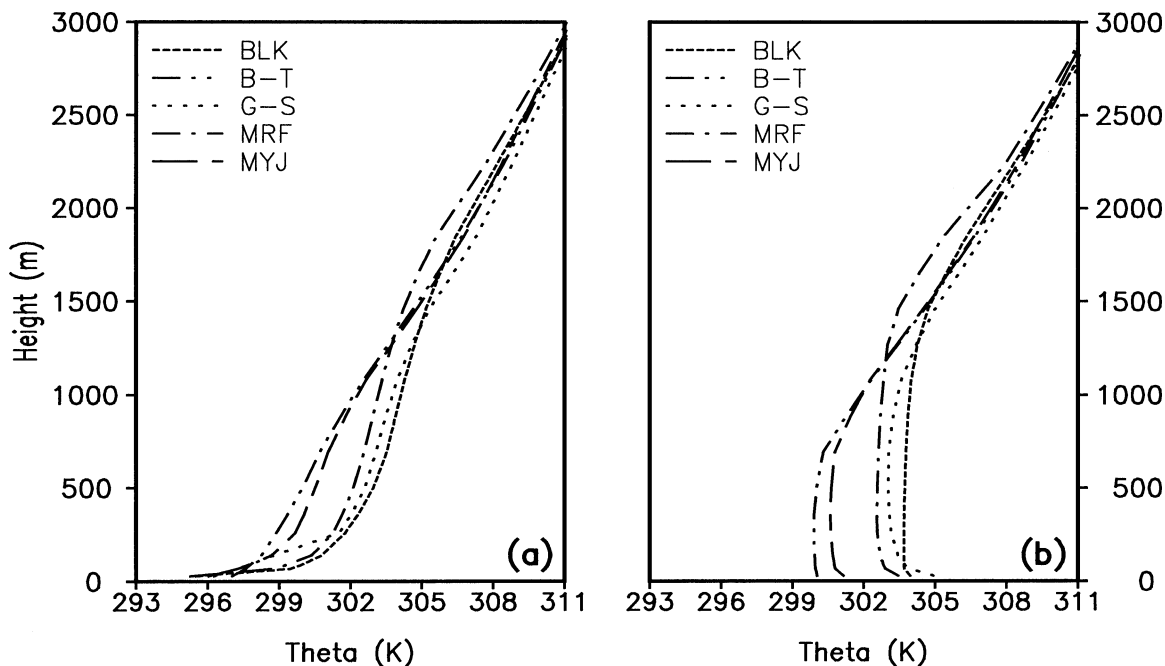
FIG. 4. Vertical profiles of the area-averaged potential temperatures (K) at (a) 0400 LST from the 45-h simulation and (b) 1300 LST from the 54-h simulation using the BLK, BT, GS, MRF, and MYJ PBL schemes.

the daytime. In relative terms, the daytime phases and amplitude of $V_{SFC}$ are better simulated by the BLK, BT, and MYJ schemes, even though the latter two schemes produce colder $T_{SFC}$ and PBL. The peak $V_{SFC}$ generated by the MRF scheme occurs 6 h ahead of the observed peak and is about 50% of the observed peak, despite the well-simulated diurnal cycles of $T_{SFC}$. This result is likely caused by the use of a prescribed $K$ profile with



FIG. 5. As in Fig. 3, but for the area-averaged surface horizontal wind speed (m s$^{-1}$). The vertical dotted lines denoted by A and B are provided to help to understand the relationship between $V_{SFC}$ and the vertical profiles of wind speeds shown in Figs. 6a and 6b, respectively.

too-small momentum diffusivity in the surface layer (see the appendix); its vertical coupling of horizontal momentum is also questionable, as compared with its nonlocal treatment of heat fluxes. Of interest is that the time series of $V_{SFC}$ generated by the GS scheme exhibits a decrease in wind speed during the early morning hours, followed by a rapid increase until it reaches its peak 3–4 h later than the observed peak. This result is to a certain extent unexpected, given the more realistic simulation of $T_{SFC}$, the more physically sound TKE closure, and the reasonable $V_{SFC}$ evolution of the other two TKE-based schemes. This result clearly must have something to do with the vertical momentum diffusivity $K_m$ [see Eq. (A2) in the appendix] and the large amplitude of the nocturnal LLJ (shown below) simulated by the GS scheme. Nonetheless, the results indicate that even a *perfect* diurnal $T_{SFC}$ (radiative) cycle does not *guarantee* a reasonable outcome of the diurnal cycles of $V_{SFC}$. The latter appears to depend highly on how the horizontal momentum above is transferred downward to the surface layer by the PBL processes. The phase correlation between $T_{SFC}$ and $V_{SFC}$ during the daytime, as shown in Fig. 2a, requires the rapid vertical exchanges (or strong coupling) of horizontal momentum between the surface layer and the layers above in the PBL. This characteristic appears to be reproduced well by the BLK, BT, and MYJ schemes, in which nonlocal closures are adopted. On the other hand, any local $K$ treatment would tend to transport the momentum fluxes slowly downward, making the daytime variations of $V_{SFC}$ out of phase with the observed.
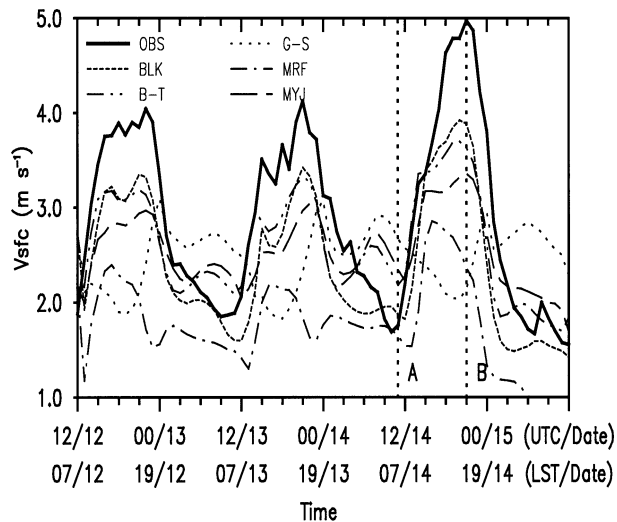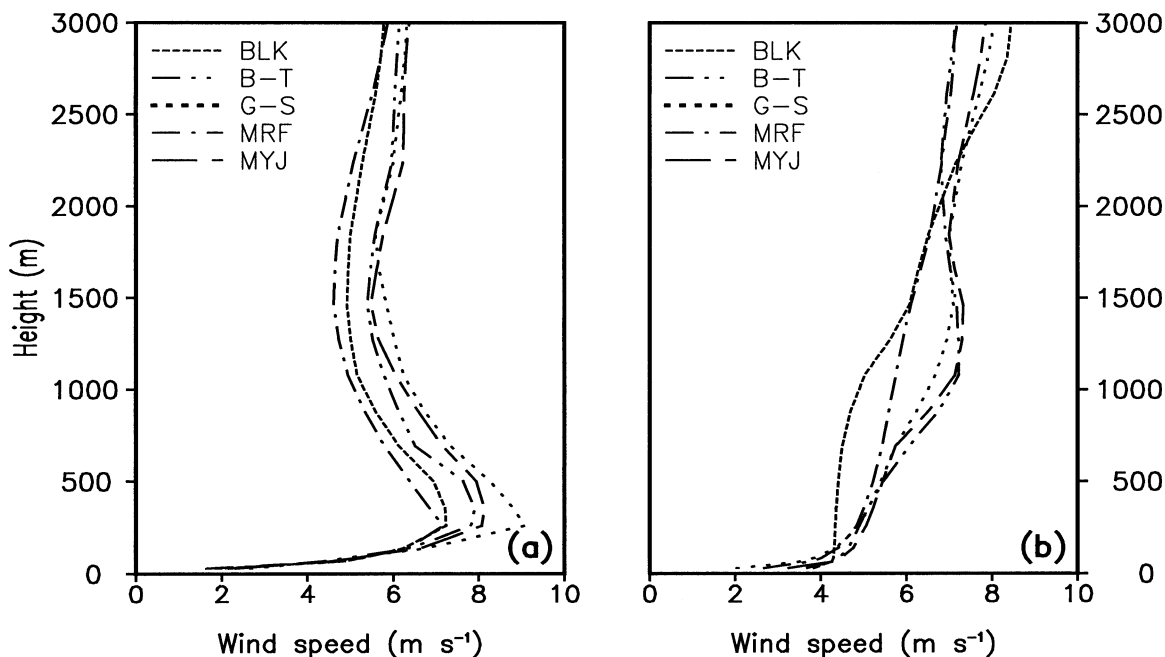
FIG. 6. As in Fig. 4, but for the area-averaged horizontal wind speed (m s$^{-1}$).

Although there are significant differences in the simulated $V_{SFC}$ (and $T_{SFC}$ and the vertical $\theta$ profiles), the vertical profiles of wind speed taken at the time of the peak $T_{SFC}$ (i.e., at 1600 LST) show similar vertical distributions, with relatively strong winds above $z = 10$–50 m, particularly for the three TKE-based schemes (Fig. 6b); the BLK and MRF schemes produce relatively weaker and well-mixed wind profiles. The simulated stronger $V_{PBL}$ but weaker $V_{SFC}$ indicate that $V_{SFC}$ in some PBL schemes is not realistically coupled with $V_{PBL}$ (cf. Figs. 5 and 6b). In this regard, the BLK scheme produces an entrainment layer (i.e., 1000–1400 m), a nearly uniform flow layer (100–1000 m), and a convective root layer below, with more momentum transferred downward to accelerate the surface flow, leading to the generation of strong $V_{SFC}$ during the daytime. This vertical wind profile in the PBL is very similar to that discussed by Santoso and Stull (1998).

It is of interest that all of the TKE-based schemes overestimate the nocturnal minimum $V_{SFC}$ (Fig. 5)—the worst overestimate of 40%–50% is generated by the GS scheme, whereas the BLK and MRF schemes tend to underestimate it slightly. The GS scheme also produces important phase errors during the nocturnal period. The pronounced errors in amplitude and phase during the nocturnal period are somewhat disturbing because the stable PBL over a near-homogeneous surface has been claimed to be understood much better and parameterized more realistically. Most PBL schemes, including those used in this study, use a local $K$ theory to treat the vertical transfers of heat, moisture, and momentum under stable conditions. The prognostic TKE equation(s) in the MYJ, GS, and BT schemes is just used to provide

more "realistic" magnitudes for the eddy exchange coefficients $K$.

Despite the different daytime developments, the nocturnal wind profiles all show the development of a local wind maximum, loosely defined herein as the LLJ, with the range of 7–9 m s$^{-1}$ near the altitude of 300 m (see Fig. 6a). This altitude is close to the top of the low-level nocturnal thermal inversion (cf. Figs. 6a and 4a), which is consistent with that discussed by Blackadar (1957). The similar wind profiles produced by the five PBL schemes are understandable because of their similar depths of the surface-based inversion (Fig. 4a) and the use of similar local $K$ treatments for turbulent transfers. On the other hand, the generation of too-strong nocturnal $V_{SFC}$ by all of the TKE-based schemes is likely caused by too much downward transport of horizontal momentum associated with the too-strong LLJ generated (cf. Figs. 5 and 6a). In nature, the flows above are decoupled with $V_{SFC}$ and a substantial reduction in eddy viscosity should occur below the inversion, as parameterized in the BLK scheme.

Overall, the BLK scheme produces the best diurnal cycles of $V_{SFC}$, whereas the GS scheme generates the worst results, with its diurnal cycles being about 12 h out of phase with the observed cycles (see Fig. 5). The daytime $V_{SFC}$ produced by the MYJ and BT schemes are comparable to those of the BLK scheme, but their nocturnal $V_{SFC}$ are too strong and have opposite time rates of change. By comparison, the MRF scheme yields systematically the weakest $V_{SFC}$ at all of the times, with some unsmoothed transitions and phase errors.

Note that the nocturnal time series of $V_{SFC}$ simulated with the BLK scheme in the previous version of MM5
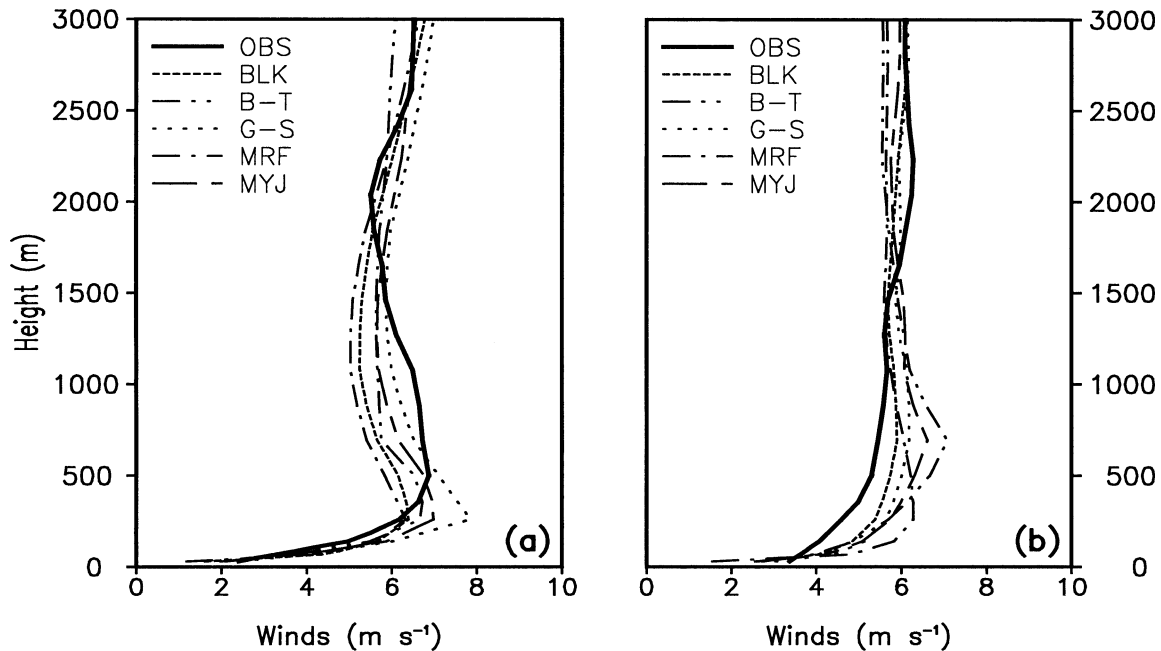
FIG. 7. Vertical profiles of the spatially (9° lat × 9° lon) and temporally (three time levels) averaged horizontal wind speeds (m s$^{-1}$) from the sensitivity simulations using the BLK, BT, GS, MRF, and MYJ, PBL schemes as compared with the observed data (solid) at (a) 1200 and (b) 0000 UTC over the period of 0000 UTC 13 Jul–1200 UTC 15 Jul 1997.

is similar to that from the MYJ and BT schemes, mainly because of the use of virtual potential temperature $\theta_v$ to estimate the bulk Richardson number ($R_b$) and the Richardson number ($R_i$) and secondarily because of the use of a relatively large background $K_0$ (i.e., 1 m$^2$ s$^{-1}$) coefficient in the (thin) surface layer. The inclusion of moisture in calculating $R_i$ and $R_b$ tends to make the atmosphere less stable, producing larger $K$ coefficients and stronger downward transfers of horizontal momentum, especially from the LLJs (see Fig. 6). In particular, Fig. 4a shows that the lowest 300 m is very stable (i.e., $R_b \geq 0.2$) so that little turbulence should be expected (Zhang and Anthes 1982). Thus, in this study we used the potential temperature $\theta$ to estimate $R_i$ and $R_b$ as in the original BLK scheme (Zhang and Anthes 1982) and set $K_0 = C_k \Delta Z$, where $C_k = 10^{-3}$ m s$^{-1}$ and $\Delta Z$ is the depth of the model layer (m), as described in the appendix.

Although the vertical profiles of the potential temperature and horizontal winds shown in Figs. 4 and 6 are useful for understanding the correlation between the surface properties and those above, it is not possible to validate whether the two extreme PBL developments are realistically simulated. However, there were six conventional upper-air stations located within the area of interest (see their locations in Fig. 1) that could be utilized to verify indirectly the above-mentioned features, because the two synoptic times of 1200 and 0000 UTC were only about 1 and 3 h later than those of $T_{MIN}$ and $T_{MAX}$, respectively. Nevertheless, the six soundings were too few to sample the mean atmospheric states over the

region. Thus, the observed wind profiles at the two synoptic times are averaged both spatially and temporally and likewise for the simulated profiles for verification purposes (see Fig. 7). In general, the simulated wind profiles by all of the PBL schemes compare favorably to those of the observed at both times. They all exhibit nearly constant wind speeds above 300 m at 0000 UTC (Fig. 7b), and local wind maxima between 300 and 500 m at 1200 UTC (Fig. 7a). Of course, some differences could also be noted. For example, the simulated wind speeds in the lowest 1.5 km at 0000 UTC are 1–2 m s$^{-1}$ stronger than those of the observed (Fig. 7b), whereas the opposite is true at 1200 UTC (Fig. 7a). A close examination of Figs. 7a and 7b reveals that the BLK and GS schemes produce the least differences in the vertical wind profiles from the observed profiles at 0000 and 1200 UTC, respectively, except that the GS nocturnal wind maximum appears to be too strong. The result indicates that all of the PBL schemes produce similar vertical distributions and magnitudes of $V_{PBL}$, which are comparable to those of the observed, in contrast to their marked variations and differences in $V_{SFC}$. The simulated vertical profiles of the potential temperature $\theta$ at the two synoptic times are also similar to those in Fig. 4, except for some evolutions in the lowest 100–200-m layer (not shown). Again, like the wind profiles, the vertical $\theta$ profiles of the GS and BLK schemes resemble better those of the observed (not shown).

To gain further insight into the relationship between $V_{SFC}$ and $V_{PBL}$, Fig. 8 shows the time series of the simulated horizontal wind speeds in the second and fourth
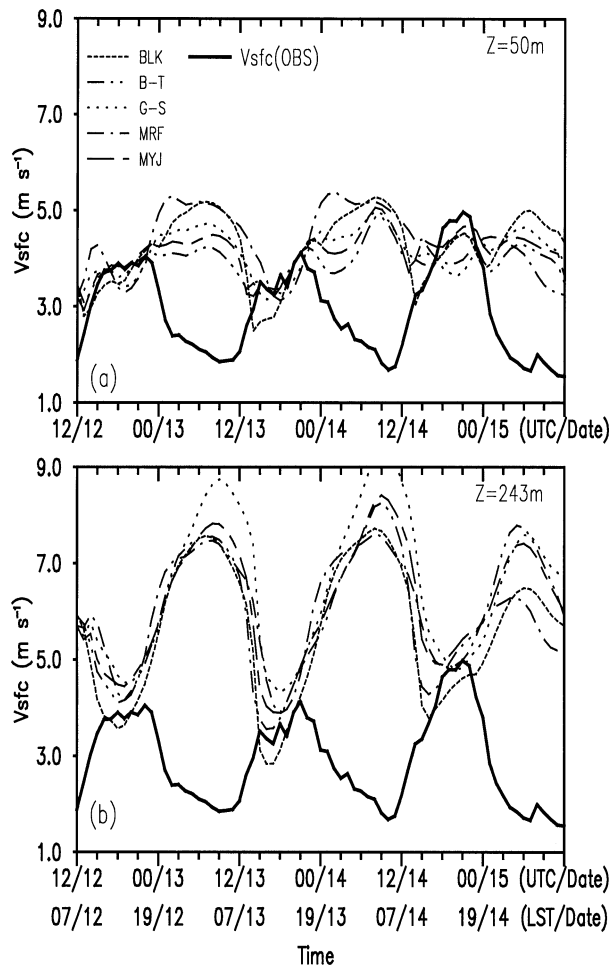
FIG. 8. Time series of the area-averaged horizontal wind speeds (m s$^{-1}$) as simulated with the BLK, BT, GS, MRF, and MYJ, PBL schemes during the 3-day period of 1200 UTC 12 Jul–1200 UTC 15 Jul 1997. They are taken at $z$ = (a) 50 and (b) 243 m. The observed $V_{SFC}$ (solid) is superposed to help to understand the relationship between the surface and boundary layer winds.
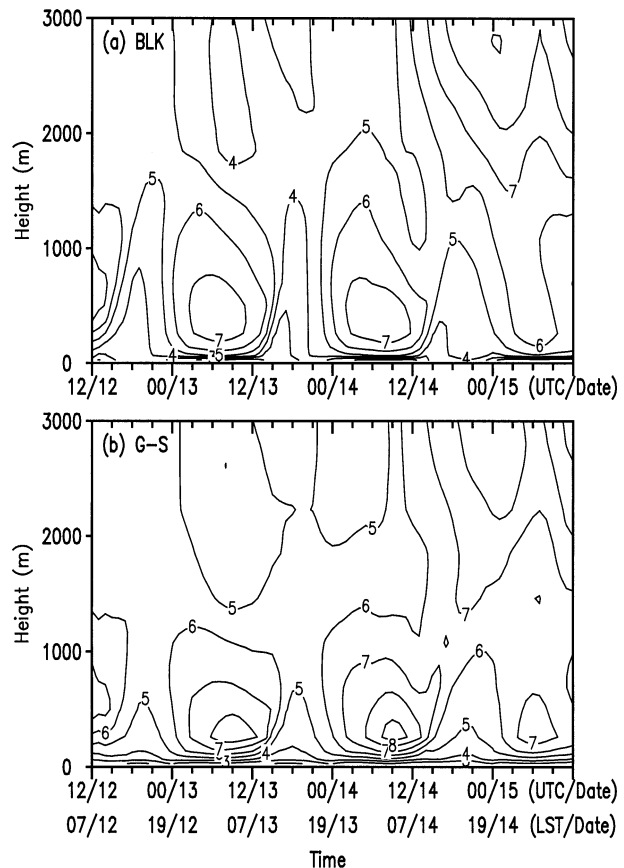


FIG. 9. The height–time cross sections of hourly, area-averaged horizontal wind speeds, at intervals of 1 m s$^{-1}$, simulated with the (a) BLK and (b) GS PBL schemes during the 3-day period of 1200 UTC 12 Jul–1200 UTC 15 Jul 1997.

model layers from the bottom surface (i.e., at $z$ = 50, 243 m) in relation to the observed $V_{SFC}$. Of interest is that $V_{PBL}$ in each layer also exhibits the diurnal cycle, more significantly near the level of the LLJs, but it is nearly opposite in phase with (i.e., 2–3 h lagging behind) the observed $V_{SFC}$. That is, $V_{PBL}$ ($V_{SFC}$) begins to weaken (intensify) 1–2 h before (after) sunrise, whereas $V_{PBL}$ ($V_{SFC}$) commences its acceleration (deceleration) in early (late) afternoon. In general, the differences in the simulated $V_{PBL}$ among the five PBL schemes become smaller with height, except for the GS scheme, the magnitude of which increases more rapidly as it approaches the level of the LLJs. Note the more pronounced asymmetries in the time series of $V_{PBL}$ as compared with those of $V_{SFC}$. This result is apparently because the variations of $V_{PBL}$ are affected not only by the surface forcing but also by the inertial oscillations and the large-scale forcing.

Figure 9 compares the time–height cross sections of horizontal wind speeds produced by the BLK and GS schemes to see their different relationships between $V_{PBL}$ and $V_{SFC}$. Some common features include the diurnal cycles of $V_{PBL}$, which negatively correlated with those of $V_{SFC}$, the development of the nocturnal LLJs with strong vertical shear below, and the weak $V_{PBL}$ with relatively weak shear during the daytime. Because of the strong vertical coupling during the daytime, the time series of $V_{SFC}$ reflects, to a certain degree, the flow structures above in the PBL, as discussed in section 2. On the third day when a weak baroclinic disturbance passes by, the daytime $V_{SFC}$ becomes stronger than before (Fig. 5) and the nocturnal LLJ turns out to be much less evident. In this case, the deeper the PBL is, the stronger is the daytime $V_{SFC}$. Based on the simulated colder $T_{SFC}$ (Fig. 3) and stronger $V_{PBL}$ aloft (Fig. 9), we may speculate that the MYJ, BT, and BLK schemes could make the daytime $V_{SFC}$ closer to that of the observed (see Fig. 5) if a deeper PBL with warmer $T_{SFC}$ were simulated. Some errors (e.g., 1 m s$^{-1}$; see Fig. 7) in the large-scale flows may also explain the underestimation of the peak $V_{SFC}$ by these PBL schemes.

A comparison of Figs. 9a and 9b reveals that the BLK-generated vertical shear in the lowest 100–200 m during the nighttime (daytime) is greater (weaker) than that by the GS scheme, even though the opposite is true for the intensity of the LLJs. This result indicates that $V_{PBL}$ in the former case is more decoupled with $V_{SFC}$ because of the reduced downward momentum transport from the LLJs. In general, the BLK-produced $V_{PBL}$, particularly for the lowest 100–200 m, shows more pronounced diurnal variations and a more rapid transition between the stable and unstable regimes than that of the GS scheme (and the other three schemes). It is evident from Fig. 9 that use of the high vertical resolution in the PBL is essential not only for resolving the LLJs and its associated large vertical shear, but also for ensuring smooth transitions in the vertical turbulent mixing between the unstable and stable turbulence regimes.

## 5. Summary and conclusions

In this study, the performance of five widely used PBL parameterization schemes in reproducing the diurnal cycles of surface wind speed in relation to surface temperature is evaluated using 3-day regional simulations of summertime weak-gradient flows over the central United States with the PSU–NCAR MM5. This case was also characterized by little organized deep convection and little topographical forcing. The area-averaged hourly time series of $V_{SFC}$ and $T_{SFC}$, as well as their vertical structures in the PBL from the five sensitivity simulations, are compared with hourly surface observations and some upper-air measurements at the two synoptic times.

The hourly surface observations show that the diurnal variations of $V_{SFC}$ are in phase with the diurnal cycles of $T_{SFC}$. Although surface wind directions also exhibit diurnal variations but 5–6 h out of phase with $V_{SFC}$ and $T_{SFC}$, their amplitudes, reasonably simulated by the five PBL schemes, are much weaker than the directional changes associated with larger-scale disturbances. So, the diurnal cycles of surface wind directions are not examined in detail in this study. The numerical simulations show that both $T_{SFC}$ and $V_{SFC}$ are sensitive to the PBL parameterizations, given the identical conditions for all of the other model parameters. It is found that the five PBL schemes all reproduce the diurnal phase of $T_{SFC}$ because of the dominant radiative forcing; three of them reproduce very well the diurnal cycles of $T_{SFC}$ in both magnitude and phase. However, all of the PBL schemes tend to underestimate the magnitudes of $V_{SFC}$ during the daytime, and three schemes overestimate them substantially at night. Moreover, some PBL schemes produce pronounced phase errors in the diurnal cycles of $V_{SFC}$ or substantially weak $V_{SFC}$ all of the time despite their well-simulated diurnal cycles of $T_{SFC}$. The results suggest that even a perfect simulation of diurnal $T_{SFC}$ cycles does not always guarantee the reproduction of the diurnal cycles of $V_{SFC}$. Furthermore, even with

the realistically simulated vertical thermal structures in the PBL, the diurnal cycles of $V_{SFC}$ may not be reasonably obtained if certain physical processes, such as the strong vertical coupling in daytime and the vertically decoupled flows at night, are not properly parameterized.

The numerical simulations also show the significant diurnal cycles of $V_{PBL}$, but in opposite phase with $V_{SFC}$, that is, with the development of weak $V_{PBL}$ during the day and LLJs at night. Such a phase relationship indicates the necessity to use a thin surface layer to reduce possible errors in simulating the lower-level flows and to use high vertical resolution to resolve the surface-based inversion, its associated LLJs, and stability transitions. It is shown that the vertical distributions and magnitudes of $V_{PBL}$ simulated by the five PBL schemes are, on average, similar to each other, and they are all comparable to those observed at the two synoptic times. Based on these results, we conclude that the diurnal cycles of $V_{SFC}$ simulated with some PBL schemes do not depend on how well the horizontal winds and mass in the PBL and $T_{SFC}$ are reproduced, although these variables are all interrelated in nature. To reproduce the observed diurnal cycles of $V_{SFC}$, it appears to be essential to incorporate realistically certain physical processes in the PBL schemes, such as the nonlocal closures, including the countergradient transport, which could provide a strong coupling between $V_{SFC}$ and $V_{PBL}$ under unstable conditions, and the Richardson number–based closures, which could distinguish various stable regimes for the generation of different vertical fluxes of the mass and momentum in the surface layer.

In this regard, the BLK scheme is shown to perform the best among the five tested PBL schemes in reproducing the diurnal cycles of $V_{SFC}$ for this particular case study. This is because (a) the BLK scheme allows direct mass and momentum exchanges between the surface layer and the layer above in the unstable PBL, with the entrainment effects included, and (b) it treats the nocturnal module with three different stability regimes based on the bulk Richardson number, which yield more reasonable magnitudes of the vertical heat and momentum fluxes in the surface layer. The use of more stability regimes also permits reasonable simulations of the transitions between a wide range of turbulent mixing regimes. It is evident that some of the above features, such as the treatment of the nocturnal module, could easily be implemented into the other PBL schemes.

It should be mentioned, however, that the results presented herein do not imply the capability of the BLK scheme to reproduce many other important PBL features. It is clear that more case studies of this kind over different geographical regions and under different surface (e.g., topographical, water) and large-scale forcing conditions should be done to generalize our findings. Furthermore, it is highly desirable to obtain 3D high-resolution observations in order to examine more realistically the model's capability to reproduce the cor-

relations among $V_{SFC}$, $V_{PBL}$, $T_{SFC}$, and the vertical thermal structures in the PBL, especially around the time of $T_{MIN}$ and $T_{MAX}$.

## APPENDIX

### The Planetary Boundary Layer Parameterization Schemes

To help to understand the characteristics of the simulated surface winds shown in section 4, some pertinent features of the five PBL schemes tested in this study are summarized below. They include calculations of the surface fluxes and the treatment of vertical turbulent mixing for the mass and wind fields under stable and unstable conditions. Most variables given below, if not defined, would assume their usual meteorological meaning.

#### a. The Blackadar PBL scheme

The Blackadar PBL scheme (Blackadar 1976, 1979; Zhang and Anthes 1982) consists of a nocturnal (stable) and a free convection (unstable) module of turbulent mixings. In the nocturnal module, local $K$ theory is used and the eddy viscosity $K$ is calculated as a function of the Richardson number $R_i$,

$$K = K_0 + \left| \frac{\partial \mathbf{V}}{\partial z} \right| \ell^2 f(R_i), \tag{A1}$$

where $K_0 = C_k \Delta Z$ is a background value that depends on the vertical resolution $\Delta Z$ and $C_k = 10^{-3}$ m s$^{-1}$, $k$ is the von Kármán constant, $\ell = kz(1 + kz/\lambda)^{-1}$ is the mixing length (Blackadar 1962), and $f(R_i)$ denotes a functional dependence of $K$ on the Richardson number $R_i$ (Holtslag and Boville 1993). For unstable conditions ($R_i < 0$), we use

$$f(R_i) = (1 - 18R_i)^{1/2}, \tag{A2}$$

and, for stable conditions ($R_i > 0$),

$$f(R_i) = \frac{1}{1 + 10R_i(1 + 8R_i)}. \tag{A3}$$

To help to reproduce the smooth transition of a wide range of turbulent mixing, the nocturnal module is subdivided into three stability regimes, depending on the bulk Richardson number $R_b$. When $R_b \geq 0.2$, the surface layer is assumed to be so stable that little turbulence exists and all fluxes at its top are set to their minimum values by assuming $K = K_0$. When $0 < R_b < 0.2$, the surface layer is assumed to be driven by damped mechanical turbulence. When $R_b \leq 0$ and $|H/L| \leq 1.5$, where $L$ is the Monin–Obukhov length and $H$ is the height of the PBL, a marginally unstable state of forced convection is assumed.

In the free convection module, $R_b \leq 0$ and $|H/L| > 1.5$, the vertical transfers of heat, moisture, and momentum are explicitly calculated using a nonlocal mixing model in which buoyant plumes from the surface layer mix directly with all other layers within the PBL. The intensity of the mixing is determined by the ratio of the heat flux at the top of the surface layer to the vertically integrated potential temperature $\theta$ difference between the surface layer and the layers in the PBL. Above the PBL (i.e., $z > H$), vertical mixing is calculated with $K$ theory as in the stable module.

#### b. The Gayno–Seaman PBL scheme

The Gayno–Seaman scheme (Shafran et al. 2000) is a Mellor–Yamada (1974) 1.5-order closure model in which a prognostic equation for turbulent kinetic energy (TKE) is included. It uses the liquid water potential temperature, $\theta_L = \theta(1 - Lq_L/c_pT)$, as the two fundamental mass variables (Betts 1973), where $q_L$ is the liquid water mixing ratio, and the total water mixing ratio $q_T = q + q_L$. Vertical turbulent transfers of the mass and wind fields are calculated using nonlocal $K$ theory, but the eddy diffusivities for the mass ($K_h$) and momentum ($K_m$) fields are determined by TKE or $E$, according to

$$K_h = \ell_h\left(\ell, E, N, \frac{\partial \mathbf{V}}{\partial z}\right)E^{1/2} \quad \text{and} \tag{A4}$$

$$K_m = \ell_m\left(\ell, E, N, \frac{\partial \mathbf{V}}{\partial z}\right)E^{1/2}, \tag{A5}$$

where the mixing-length scales $\ell_h$ and $\ell_m$ are defined by Ballard et al. (1991), and $N$ is the moist buoyancy frequency. Under unstable conditions, a nonlocal $K$ approach is adopted by adding a countergradient $\theta_L$ flux term $\gamma_c$ to the local gradient transport, that is,

$$\overline{w'\theta'_L} = -K_h\left(\frac{\partial \theta_L}{\partial z} - \gamma_c\right), \tag{A6}$$

for the layers of $z < 1.2H$. In this scheme, the PBL depth is diagnosed from the TKE profile as the level at

which the surface-based mixed-layer TKE decreases to $0.1$ m² s⁻² in strongly convective situations (i.e., when the maximum PBL TKE $> 0.2$ m² s⁻²) or to 50% of the maximum TKE in weakly convective situations (i.e., when the maximum PBL TKE $< 0.2$ m² s⁻²). The surface fluxes are calculated in the same way as those in the BLK scheme (Zhang and Anthes 1982).

### c. The PBL scheme in the Medium-Range Forecast model

The MRF scheme (Hong and Pan 1996) is a nonlocal $K$ scheme in which the countergradient transports of temperature and moisture under unstable conditions are added to the local gradient transports in a form similar to that given in Eq. (A6). In this situation, the PBL height $H$ is estimated by

$$H = \mathrm{Rb}_c \frac{\theta_v(z = z_a)|V(z = H)|^2}{g[\theta_v(z = H) - \theta(z = z_a)]}, \quad \text{(A7)}$$

where $\mathrm{Rb}_c$ is the critical bulk Richardson number, $\theta_v$ is the virtual potential temperature, and $z = z_a$ and $z = H$ represent, respectively, the surface layer and the top of the PBL at which $\theta_v$, $\theta$, and $V$ are involved in the calculation. The eddy diffusivity for the wind field $K_m$ is obtained from a prescribed profile shape, similar to that of O'Brien (1970), as a function of $H$, the height from the surface $z$, and some surface scaling parameters, whereas the eddy diffusivities for the mass field are computed from $K_m$ by using a Prandtl-number relationship.

Under stable conditions, including the layers above the PBL, the local $K$ approach is utilized for all prognostic variables, in which the eddy diffusivity $K_z$ is calculated as a function of the mixing length, $R_i$, and $\partial|\mathbf{V}|/\partial z$. The value of $K_z$ is limited between 1 and 1000 m² s⁻¹ for all possible atmospheric conditions.

The vertical diffusivities so obtained also apply to the surface layer under both stable and unstable conditions.

### d. The Miller–Yamada–Janjić PBL scheme

The Miller–Yamada–Janjić (Janjić 1990, 1994) scheme is a Mellor–Yamada (1982) level-2.5 scheme, or a variant of 1.5-order closure model that includes a prognostic equation of the TKE. Like all of the TKE closures, the nonlocal $K$ approach is used, which has a form similar to that given in Eqs. (A4) and (A5) but as complex algebraic functions of the mixing length, TKE, vertical wind shear, and static stability. The mixing length is diagnosed as a function of the height from the surface, which is large under unstable conditions. In these situations, certain constraints are imposed to avoid the development of too-large $K$.

The surface layer is treated using a Mellor–Yamada (1982) level-2 closure with the logarithmic extension. The magnitudes of surface eddy exchange coefficients depend on the mixing length, vertical shear, and static stability.

### e. The Burk–Thompson PBL scheme

The Burk–Thompson (1989) PBL scheme is a Mellor–Yamada (1982) level-2.5 scheme, or a variant of 1.5-order closure model with many features similar to those in the MYJ scheme. Unlike the formulations described in Burk and Thompson (1989), the scheme in MM5 does not include the countergradient $\theta_v$ and moisture flux terms.

#### REFERENCES

Aspliden, C. I., 1977: Dirunal and semidiurnal low-level wind cycles over a tropical island. *Bound.-Layer Meteor.,* **12,** 187–199.

Ballard, S. P., B. W. Golding, and R. N. B. Smith, 1991: Mesoscale model experimental forecasts of the Haar of northeast Scotland. *Mon. Wea. Rev.,* **119,** 2107–2123.

Betts, A. K., 1973: Non-precipitating cumulus convection and its parameterization. *Quart. J. Roy. Meteor. Soc.,* **99,** 178–196.

Blackadar, A. K., 1957: Boundary layer wind maxima and their significance for the growth of nocturnal inversions. *Bull. Amer. Meteor. Soc.,* **83,** 283–290.

——, 1962: The vertical distribution of wind and turbulent exchange in a neutral atmosphere. *J. Geophys. Res.,* **67,** 3095–4102.

——, 1976: Modeling the nocturnal boundary layer. Preprints, *Third Symp. on Atmospheric Turbulence, Diffusion and Air Quality,* Raleigh, NC, Amer. Meteor. Soc., 46–49.

——, 1979: High resolution models of the planetary boundary layer. *Advances in Environmental Science and Engineering.* J. Pfafflin and E. Ziegler, Eds., Vol. 1, Gordon and Breach, 50–85.

Braun, S. A., and W.-K. Tao, 2000: Sensitivity of high-resolution simulations of Hurricane Bob (1991) to planetary boundary layer parameterizations. *Mon. Wea. Rev.,* **128,** 3941–3961.

Burk, S. D., and W. T. Thompson, 1989: A vertically nested regional numerical weather prediction model with second-order closure physics. *Mon. Wea. Rev.,* **117,** 2305–2324.

Carbone, R. E., J. D. Tuttle, D. A. Ahijevych, and S. B. Trier, 2002: Inferences of predictability associated with warm season precipitation episodes. *J. Atmos. Sci.,* **59,** 2033–2056.

Chen, F., and J. Dudhia, 2001: Coupling an advanced land surface–hydrology model with the Penn State–NCAR MM5 modeling system. Part I: Model implementation and sensitivity. *Mon. Wea. Rev.,* **129,** 569–585.

Dai, A., and C. Deser, 1999: Diurnal and semidiurnal variations in global surface wind and divergence field. *J. Geophys. Res.,* **104,** 31 109–31 125.

——, F. Giorgi, and K. E. Trenberth, 1999: Observed and model-simulated diurnal cycles of precipitation over the contiguous United States. *J. Geophys. Res.,* **104,** 6377–6402.

Deng, A., N. L. Seaman, and J. S. Kain, 2003: A shallow-convective parameterization for mesoscale models. Part I: Submodel description and preliminary application. *J. Atmos. Sci.,* **60,** 34–56.

Deser, C., 1994: Daily surface wind variations over the equatorial Pacific Ocean. *J. Geophys. Res.,* **99,** 23 071–23 078.

Dudhia, J., 1989: Numerical study of convection observed during the winter monsoon experiments using a mesoscale two-dimensional model. *J. Atmos. Sci.,* **46,** 3077–3107.

——, 1993: A nonhydrostatic version of the Penn State–NCAR mesoscale model: Validation tests and simulation of an Atlantic cyclone and cold front. *Mon. Wea. Rev.,* **121,** 1493–1513.

Grell, G. A., J. Dudhia, and D. R. Stauffer, 1995: A description of the fifth-generation Penn State/NCAR Mesoscale Model (MM5). NCAR Tech. Note NCAR/TN-398 1 STR, 122 pp.

Hering, W. S., and T. R. Borden Jr., 1962: Diurnal variations in the

summer wind field over the central United States. *J. Atmos. Sci.,* **19,** 81–86.

Holt, T., and S. Raman, 1988: A review and comparative evaluation of multilevel boundary layer parameterizations for first-order and turbulent kinetic energy closure schemes. *Rev. Geophys.,* **26,** 761–780.

Holtslag, A. A. M., and B. A. Boville, 1993: Local versus nonlocal boundary-layer diffusion in a global climate model. *J. Climate,* **6,** 1825–1842.

Hong, S.-H., and H.-L. Pan, 1996: Nonlocal boundary layer vertical diffusion in a medium-range forecast model. *Mon. Wea. Rev.,* **124,** 2322–2339.

Hsie, E.-Y., R. A. Anthes, and D. Keyser, 1984: Numerical simulation of frontogenesis in a moist atmosphere. *J. Atmos. Sci.,* **41,** 2581–2594.

Janjić, Z. I., 1990: The step-mountain coordinate: Physical package. *Mon. Wea. Rev.,* **118,** 1429–1443.

——, 1994: The step-mountain Eta coordinate model: Further development of the convection, viscous sublayer and turbulent closure schemes. *Mon. Wea. Rev.,* **122,** 927–945.

Kain, J. S., and J. M. Fritsch, 1993: Convective parameterization for mesoscale models: The Kain–Fritsch scheme. *Cumulus Parameterization, Meteor. Monogr.,* No. 46, Amer. Meteor. Soc., 165–170.

Mellor, G. L., and T. Yamada, 1974: A hierarchy of turbulence closure models for planetary boundary layers. *J. Atmos. Sci.,* **31,** 1791–1806.

——, and ——, 1982: Development of a turbulence closure model for geophysical fluid problems. *Rev. Geophys. Space Phys.,* **20,** 851–875.

Moeng, C.-H., 1984: A large-eddy-simulation model for the study of planetary boundary-layer turbulence. *J. Atmos. Sci.,* **41,** 2052–2062.

O'Brien, J. J., 1970: A note on the vertical structure of the eddy exchange coefficient in the planetary boundary layer. *J. Atmos. Sci.,* **27,** 1213–1215.

Perkey, D. J., and W. Kreitzberg, 1976: A time-dependent lateral boundary scheme for limited area primitive equation models. *Mon. Wea. Rev.,* **104,** 744–755.

Reiter, E. R., and M. Tang, 1984: Plateau effects on diurnal circulation patterns. *Mon. Wea. Rev.,* **112,** 638–651.

Santoso, E., and R. Stull, 1998: Wind and temperature profiles in the radix layer: The bottom fifth of the convective boundary layer. *J. Appl. Meteor.,* **37,** 545–558.

Savijarvi, H., 1997: Diurnal winds around Lake Tanganyika. *Quart. J. Roy. Meteor. Soc.,* **123,** 901–918.

Shafran, P. C., N. L. Seaman, and G. A. Gayno, 2000: Evaluation of numerical predictions of boundary layer structure during the Lake Michigan ozone study. *J. Appl. Meteor.,* **39,** 412–426.

Xue, Y., P. J. Sellers, J. L. Kinter, and J. Shukla, 1991: A simplified biosphere model for global climate studies. *J. Climate,* **4,** 345–364.

Zhang, D.-L., 1989: The effect of parameterized ice microphysics on the simulation of vortex circulation with a mesoscale hydrostatic model. *Tellus,* **41A,** 132–147.

——, and R. A. Anthes, 1982: A high-resolution model of the planetary boundary layer—Sensitivity tests and comparisons with SESAME-79 data. *J. Appl. Meteor.,* **21,** 1594–1609.